

**Measuring Decoherence and the Matter-wave  
Index of Refraction with an Improved Atom  
Interferometer**

by

David Anthony Kokorowski

Submitted to the Department of Physics  
in partial fulfillment of the requirements for the degree of

Doctor of Philosophy

at the

MASSACHUSETTS INSTITUTE OF TECHNOLOGY

June 2001

© David Anthony Kokorowski, MMI. All rights reserved.

The author hereby grants to MIT permission to reproduce and  
distribute publicly paper and electronic copies of this thesis document  
in whole or in part.

Author .....  
Department of Physics  
May 3, 2001

Certified by .....  
David E. Pritchard  
Professor of Physics  
Thesis Supervisor

Accepted by .....  
Thomas J. Greytak  
Professor, Associate Department Head for Education

# Measuring Decoherence and the Matter-wave Index of Refraction with an Improved Atom Interferometer

by

David Anthony Kokorowski

Submitted to the Department of Physics  
on May 3, 2001, in partial fulfillment of the  
requirements for the degree of  
Doctor of Philosophy

## Abstract

This thesis describes experiments performed using the MIT atom interferometer, which has recently been upgraded to provide increased experimental precision and flexibility.

The three-gratings comprising our Mach-Zehnder interferometer have been installed on a vibration isolated platform which has reduced rms motion of the gratings by a factor of two. The arrangement of gratings on the platform can be reconfigured at will, and the entire platform removed from the vacuum chamber for purposes of alignment.

We have performed a series of experiments related to decoherence in an atom interferometer. We have explored decoherence due to photon scattering, in particular the transition from single- to multiple-photon decoherence, and have quantitatively verified the decoherence rate constant in the many-photon regime. We have also examined decoherence due to background gas scattering. Finally, we have investigated the distinction between decoherence and classical dephasing by comparing experiments which illustrate each of these phenomena.

We have made new measurements of the index of refraction of argon for sodium matter-waves. Our results are twice as precise previous measurements but suffer from significant systematic error. A detailed study of systematics is presented along with concrete proposals for minimizing their effect in future matter-wave index of refraction measurements.

Thesis Supervisor: David E. Pritchard  
Title: Professor of Physics

# Acknowledgments

I gratefully acknowledge my advisor, Dave Pritchard, for his many roles in my education as a physicist. Not only was he a first-class mentor and scientific resource, but he also provided me opportunities to develop leadership, time management, and self-awareness.

I have also learned from Prof. Winthrop Smith and Prof. Herb Bernstein with whom I collaborated on previous projects in our lab, and from Prof. Wolfgang Ketterle and Prof. Dan Kleppner with whom I have had the pleasure of interacting at MIT. I would like to thank Prof. Ketterle in particular for allowing us to borrow from his group the laser light we needed to perform the decoherence experiment.

From the previous graduate students on the atom interferometer project, Troy Hammond, Ed Smith, and Rich Rubenstein, I learned almost all of what I know about day-to-day labwork and much of what I know about atomic physics. I directly benefited not only from their wisdom, but also from all the hard work that they put into building and improving the apparatus I inherited. I feel grateful for the long, frustrating nights we spent running the experiment together; occasions which gave me a chance to interact with Troy, Ed, and Rich not just as colleagues but as friends.

More recently, it has been a pleasure to work with Alex Cronin and Tony Roberts on the two experiments in this thesis. I am quite literally amazed at the dedication and energy with which they devoted themselves to making these experiments happen. Both are impressive scientists, and without their contributions, the work presented in this thesis would not have been possible. Their presence, along with that of postdoc Jana Lehner and a series of talented undergraduates: Celeste Yang, Jay Mitchell, Martin Tiberg, and Peter Finin, was not only instrumental to the science we did together, but also transformed the lab from a mere workplace into a real community.

I am also grateful to the larger community of students and postdocs in atomic physics at MIT for their willingness to share equipment and ideas (especially about how to get a dye laser working), for the engaging conversations which kept me excited about physics, and for their pleasant society. In particular, I have enjoyed working

closely with Deep Gupta both in the lab and on several papers.

Finally, for their role in keeping everything in perspective, I thank Allen, Amanda, Dan, John, Kieran, Sean, and Winthrop. Special thanks to my parents, brothers, and sister, who were there for me at any time and in any capacity I needed them, and to Jen for her support, patience, and insight as I was writing this thesis.

Because [quantum] behavior is so unlike ordinary experience, it is very difficult to get used to and it appears peculiar and mysterious to everyone, both to the novice and to the experienced physicist. Even the experts do not understand it the way they would like to, and it is perfectly reasonable that they should not, because all of direct, human experience and of human intuition applies to large objects.

— Richard P. Feynman

# Contents

<b>1</b>	<b>Introduction</b>	<b>14</b>
1.1	Historical Introduction to Atom Interferometry . . . . .	14
1.2	Previous Atom Interferometry Experiments . . . . .	16
1.2.1	Inertial Sensing . . . . .	16
1.2.2	Fundamental Physics . . . . .	17
1.2.3	Precision Measurements . . . . .	17
1.3	Overview of the Thesis . . . . .	18
<b>2</b>	<b>Apparatus</b>	<b>19</b>
2.1	Introduction . . . . .	19
2.2	Beam Machine . . . . .	20
2.2.1	Source Region . . . . .	20
2.2.2	Main Region . . . . .	22
2.2.3	Detector Region . . . . .	22
2.3	MIT Atom Interferometer . . . . .	24
2.3.1	Overview . . . . .	24
2.3.2	Forming and Detecting an Atom Interference Pattern . . . . .	24
2.3.3	Interferometer Platform . . . . .	27
2.4	Diffraction Gratings . . . . .	39
2.4.1	Overview . . . . .	39
2.4.2	Important Grating Parameters . . . . .	42
2.4.3	Characterization of 100 nm Period Gratings . . . . .	44
2.4.4	Conclusion . . . . .	49

<b>3</b>	<b>Measuring Decoherence with an Atom Interferometer</b>	<b>52</b>
3.1	Introduction . . . . .	52
3.1.1	Motivation . . . . .	52
3.1.2	Chapter Outline . . . . .	53
3.2	Theory and Previous Experiments . . . . .	54
3.2.1	General Decoherence Theory . . . . .	54
3.2.2	Previous Experiments . . . . .	58
3.3	Decoherence due to Photon Scattering in an Atom Interferometer . . . . .	59
3.3.1	Photon Decoherence Theory . . . . .	59
3.3.2	Apparatus and Procedures . . . . .	61
3.3.3	Results . . . . .	63
3.3.4	Experimental Details . . . . .	65
3.4	Decoherence from Two Successive Environments . . . . .	72
3.5	Decoherence due to Background Gas Scattering . . . . .	73
3.6	Decoherence versus Dephasing . . . . .	78
3.6.1	Introduction . . . . .	78
3.6.2	Fourth-Grating (Dephasing) Experiment . . . . .	80
3.6.3	The “Decohering Environment” . . . . .	80
3.6.4	Comparison with Photon Decoherence . . . . .	82
3.6.5	Distinguishing between Decoherence and Dephasing . . . . .	83
<b>4</b>	<b>Measuring the Matter-Wave Index of Refraction with an Atom Interferometer</b>	<b>87</b>
4.1	Introduction . . . . .	87
4.1.1	Motivation . . . . .	87
4.1.2	Chapter Outline . . . . .	88
4.2	Theory and Previous Measurements . . . . .	88
4.2.1	Ground State Sodium-Argon Interaction Potential . . . . .	88
4.2.2	Matter-Wave Index of Refraction: Theory . . . . .	90
4.2.3	Interferometric Measurement of the Index of Refraction . . . . .	94

4.2.4	Velocity Averaging and Glory Oscillations . . . . .	96
4.2.5	Previous Index of Refraction Measurements . . . . .	99
4.3	Experiment . . . . .	99
4.3.1	Apparatus and Procedures . . . . .	101
4.3.2	Improvements over Previous Experiments . . . . .	107
4.3.3	New Measurements . . . . .	110
4.4	Analysis of Systematic Errors . . . . .	112
4.4.1	Other Interfering Orders . . . . .	112
4.4.2	Molecule Interferometers . . . . .	115
4.4.3	Attenuation of the Path Traveling Outside the Gas Cell . . . . .	119
4.4.4	Impure Target Gas . . . . .	121
4.4.5	Gas Cell Filling/Emptying . . . . .	125
4.4.6	Summary of Systematics . . . . .	127
4.5	Future Prospects . . . . .	129
<b>A Diffraction of Sodium Atoms through a Nanofabricated Grating</b>		<b>131</b>
A.1	Introduction . . . . .	131
A.2	Physical Model . . . . .	131
A.2.1	Multiple Slit Diffraction . . . . .	131
A.2.2	Variable Open Fraction . . . . .	132
A.2.3	Velocity Distribution and Collimation . . . . .	133
A.2.4	Detection Geometry . . . . .	134
A.2.5	Molecules . . . . .	135
A.2.6	Background . . . . .	135
A.3	Synthesis . . . . .	135
A.4	Effect of Atom-Wall Interactions . . . . .	136
<b>B Paper: From Single to Multiple-Photon Decoherence in an Atom Interferometer</b>		<b>137</b>

<b>C Paper: Longitudinal Quantum Beam Tomography</b>	<b>143</b>
C.1 INTRODUCTION . . . . .	143
C.1.1 Longitudinal Tomography . . . . .	146
C.1.2 ‘Initial’ Time . . . . .	148
C.1.3 Experimental Parameters . . . . .	149

# List of Figures

2-1	Atom Beam Machine Schematic . . . . .	21
2-2	Formation and Detection of Atom Interference Fringes . . . . .	25
2-3	Atom Interference Fringe Data . . . . .	27
2-4	Interferometer Platform Schematic . . . . .	28
2-5	Interferometer Platform Suspension . . . . .	30
2-6	Interferometer Platform Oscillation Modes . . . . .	32
2-7	Contrast versus Grating Spacing Error . . . . .	34
2-8	Additional Diffraction Orders . . . . .	35
2-9	Variable Period Fringes . . . . .	38
2-10	200 nm Period Diffraction Grating . . . . .	40
2-11	Contrast versus Open Fraction Variation . . . . .	44
2-12	Sodium Diffraction through a 100 nm Period Grating . . . . .	45
2-13	Contrast versus Atom Beam Height . . . . .	46
2-14	Sodium Diffraction through a Flawed 100 nm Period Grating . . . . .	48
2-15	Flawed 100 nm Period Diffraction Grating . . . . .	50
3-1	Photon Decoherence Experiment Schematic . . . . .	62
3-2	Contrast versus Number of Scattered Photons . . . . .	63
3-3	Decoherence in the Many-Photon Regime . . . . .	64
3-4	Decoherence versus Path Separation . . . . .	64
3-5	Decoherence Region Optics . . . . .	67
3-6	Momentum Spread versus Number of Scattered Photons . . . . .	69
3-7	Zero Phase Drift . . . . .	70

3-8	Successive Decohering Environments: Level Scheme . . . . .	72
3-9	Successive Decohering Environments: Schematic and Results . . . . .	74
3-10	Contrast versus Background Gas Pressure . . . . .	76
3-11	Dephasing Experiment Schematic . . . . .	79
3-12	Comparison of Contrast Loss due to Dephasing versus Decoherence . . . . .	80
3-13	Decoherence versus Dephasing Thought Experiment . . . . .	85
4-1	Sodium-Argon Interaction Potentials . . . . .	89
4-2	Matter-Wave Attenuation and Phase Shift in a Gas . . . . .	91
4-3	Index of Refraction Experiment Schematic . . . . .	94
4-4	Effect of Velocity Averaging on $\rho_{\text{NaAr}}$ . . . . .	97
4-5	Impact Parameters Leading to Glory Oscillations . . . . .	98
4-6	Previous Measurements of $\rho_{\text{NaAr}}$ . . . . .	100
4-7	Index of Refraction Experiment Schematic . . . . .	102
4-8	Target-Gas Cell . . . . .	103
4-9	Raw Count Rate, Contrast, and Phase Data . . . . .	106
4-10	Comparison of Current and Previous Index of Refraction Data . . . . .	109
4-11	New $\rho_{\text{NaAr}}$ Measurements . . . . .	111
4-12	Other Interfering Orders Schematic . . . . .	113
4-13	Systematic Error due to Other Interfering Orders . . . . .	115
4-14	Molecule Interferometers Schematic . . . . .	116
4-15	Systematic Error due to Molecule Interferometers . . . . .	118
4-16	Attenuation of the Path Traveling Outside the Gas Cell . . . . .	120
4-17	Systematic Error due to Attenuation of the Path Traveling Outside the Gas Cell . . . . .	121
4-18	Systematic Error due to Impure Target Gas . . . . .	122
4-19	Systematic Error due to Nitrogen Leak . . . . .	124
4-20	Target Cell Filling/Emptying Time Constants . . . . .	125
4-21	Systematic Error due to Gas Cell Filling/Emptying . . . . .	127
4-22	Measurements of $\rho_{\text{NaAr}}$ Corrected for Systematic Errors . . . . .	128

4-23	Theoretical Predictions for $\rho_{\text{NaAr}}$ , $\rho_{\text{NaKr}}$ , and $\rho_{\text{NaXe}}$ . . . . .	130
C-1	Longitudinal beam tomography setup . . . . .	152
C-2	Range of experimentally accessible rotation angles . . . . .	152

# List of Tables

2.1	Contrast and Signal-to-Noise versus Grating Open Fraction . . . . .	43
2.2	100 nm Period Grating Summary . . . . .	51
3.1	Decoherence Master Equations . . . . .	56
3.2	Localization Rates . . . . .	57
4.1	Comparison of Sodium-Argon Potential Parameters . . . . .	91
4.2	Magnitude of Systematic Errors . . . . .	129

# Chapter 1

## Introduction

This thesis describes experiments performed using an atom interferometer: a device which coherently splits and recombines matter waves to form a spatial interference pattern. In this chapter I present a brief historical introduction to matter-wave interferometry<sup>1</sup>, review previous atom interferometer experiments, and give an overview of the work to be described in the thesis.

### 1.1 Historical Introduction to Atom Interferometry

Optical interferometers which coherently split and recombine light waves have been a standard tool of the experimental physicist for over a century, and have produced many beautiful experiments and precise measurements. With the development of quantum mechanics came the realization that massive particles also possess wavelike properties, as epitomized by the famous deBroglie relation:  $\lambda_{dB} = h/mv$ . Matter-wave interferometry is therefore a natural extension of the earlier work with light interferometers, and is proving to be a valuable tool in its own right.

A fundamental requirement for building a matter-wave interferometer is some method for coherently splitting a matter wave into two distinct components. Devel-

---

<sup>1</sup>For a more complete overview of matter-wave interferometry see Refs. [16, 10, 12]

oping such a “beamsplitter” proved easier for neutron matter waves, which can be transmitted through solid material, and electron matter waves which can be reflected or refracted by static electromagnetic fields than for atoms. As a result the first matter-wave interferometers were built for electrons [76, 77, 81] in the 1950’s and neutrons [75, 91] in the 1960’s and 1970’s, while the first atom interferometers did not appear until the early 1990’s [60, 21, 59, 94]. Compared to electron or neutron interferometry, atom interferometry offers greater richness due to the atom’s internal structure, the wide range of properties possessed by different atoms (e.g. mass, magnetic moment, absorption frequencies, and polarizability), and the variety of interactions between atoms and their environment (e.g. static E-M fields, radiation, and other atoms). However atoms, with rare exception, stick to solid surfaces rather than bouncing from or passing through them, and as neutral particles are only weakly affected by static electromagnetic fields. Thus, the same beamsplitters used to build electron or neutron interferometers could not easily be applied to atoms.

Beamsplitters for atoms have since been developed, using two different general techniques. The first employs laser beams, tuned near an atomic transition, to implement stimulated scattering, in which an atom absorbs a photon from one traveling laser beam and is stimulated to emit the photon into a second beam. Stimulated scattering imparts momentum equal to the difference of the two photon momenta, and thus can be used to change the direction of a matter wave. If the two light beams are coherent, the coherence of the atom’s wave function is maintained. A complete beamsplitter is realized by arranging that there is some amplitude for coherent scattering to leave the atom in two (or more) final momentum states.

Nanofabricated structures offer an alternative way to coherently manipulate matter waves. In particular, nanofabricated diffraction gratings have been produced which, in exactly the same fashion as optical diffraction gratings, coherently split an incoming matter wave into multiple diffracted orders. Because diffraction is a coherent process, the grating represents a coherent beamsplitter. Nanofabricated beamsplitters differ from those based on light forces in a number of ways: they are amplitude gratings (with corresponding loss of transmission intensity), they are species-independent,

their scale size can be several times smaller than attainable with light, and they can be arbitrarily patterned.

A variety of atom and molecule interferometers have been built using these two beamsplitting technologies. A majority have used a three-grating configuration in which the first grating splits the incident beam, the second reverses the differential momenta given by the first, and the third recombines the two beams at the location where they overlap. Both material and light gratings have been developed and used in the Raman-Nath, Bragg, and adiabatic regimes to obtain interference fringes in either position or internal state space. Thermal or supersonic beam interferometers have been made for Ar\*, Ca, Cs, He\*, K, Mg, Ne\*, Rb, and Na<sub>2</sub> and I<sub>2</sub> molecules, interferometers starting with trapped atoms have been made for Cs, Ca, He\*, Mg, and Rb, and interferometers using Bose-Einstein condensates have been demonstrated with Na and Rb.

## 1.2 Previous Atom Interferometry Experiments

In the decade since their creation, atom interferometers have been used to perform a broad variety of experiments. These experiments can be classified into three categories: inertial sensing, fundamental physics, and measurements of atomic and molecular properties.

### 1.2.1 Inertial Sensing

When a separated beam atom (or light) interferometer is subject to an acceleration or rotation, the interference fringes are shifted in phase by an amount proportional to the rotation/acceleration [104]. Partly because of the extremely short wavelength of matter waves with respect to light, atom interferometers are potentially much more sensitive to these inertial effects than light interferometers. Indeed, an early study of rotation sensing with an atom interferometer [71] demonstrated a sensitivity to rotations equal to that of the best commercially available laser gyroscopes, and subsequent experiments have improved upon this result by more than four orders

of magnitude [50]. The sensitivity of atom interferometers to acceleration has been exploited to measure and map out gradients in the Earth’s gravitational field [88, 110].

### 1.2.2 Fundamental Physics

Atom interferometers have been used to demonstrate and study a host of interesting phenomena predicted by quantum mechanics. Several interferometer experiments, including one described in this thesis, have explored the phenomena of decoherence and wave-particle duality (see Chapter 3). Others have investigated the Aharonov-Bohm [82] and Aharonov-Casher [80, 132] effects — the simplest of the so-called “topological” phases discovered by M.V. Berry [14]. A more complicated topological phase arising when a neutral, polarizable particle (i.e. atom) which moves in crossed electric and magnetic fields has been predicted and is being pursued experimentally [128, 84]. A number of theorists have proposed interferometric techniques for measuring the quantum state of both the transverse [57, 40, 64, 124, 73], and longitudinal [29, 66, 92] degrees of freedom of atoms in an atomic beam. A two-slit atom interferometer has been used to tomographically reconstruct the Wigner function for the transverse degree of freedom of an atomic beam [69], and an experiment in our own group has measured an atomic beam’s longitudinal quantum state [100]. As inertial sensors, atom interferometers hold promise for making sensitive tests of general relativity [49]. Recently, atom interferometry with Bose-Einstein condensates has been demonstrated, and has already been used to study long range phase coherence [6, 53, 52, 15, 85], solitons [28], mean field effects [106], and vortices [1].

### 1.2.3 Precision Measurements

Finally, atom interferometers have proven to be valuable tools for making precision measurements of fundamental atomic and molecular parameters. Our own group has measured interferometrically the polarizability of sodium to 10 times the precision of any other technique [35]. Part-per-billion measurements of  $\hbar/m_{Cs}$  [125] are underway which will eventually lead to a new measurement of  $\alpha$ , the fine-structure constant.

Atom-atom scattering within an interferometer has been used to study interatomic potentials, though it is not yet as sensitive as other techniques for determining these potentials [39] (see also Chapter 4 of this thesis.)

## 1.3 Overview of the Thesis

The remainder of this thesis is divided into three chapters:

Chapter 2 describes the atom interferometer apparatus, focusing on improvements implemented over the past two years. It also describes the nanofabricated diffraction gratings that are the enabling feature of our interferometer, and includes a study of next-generation gratings of smaller period than the gratings currently used. Appendix A describes an analytical model which we use to extract various atom beam and diffraction grating parameters from measured diffraction patterns.

Chapter 3 describes four experiments relating to decoherence within an atom interferometer. Included in Appendix B is a recently published [65] article describing the most important of these: a study of decoherence due to photon scattering which explores the transition from single- to multiple-photon decoherence.

Chapter 4 describes recent advances in our group's ongoing study of the matter-wave index of refraction. New measurements of the refractive index of argon for sodium matter waves are presented, as well as an analysis of several systematic errors that must be taken into account as the experiment progresses.

# Chapter 2

## Apparatus

### 2.1 Introduction

The MIT atom interferometer uses nanofabricated diffraction gratings to split and recombine sodium matter waves, creating a spatial interference pattern which is then detected. The interferometer has been in operation since 1991, and is described in detail in several theses written between 1991 and 1997 [24, 34, 54, 61]. In 1997, major modifications were made to the vacuum system housing the interferometer to create additional space, leaving the atom beam source and detector unchanged. The additional space had two intended purposes: to accommodate longitudinal atom optical elements for new series of longitudinal interferometry experiments [98, 108], and to allow the entire atom interferometer to be assembled on a rigid, vibration isolated platform for increased experimental flexibility and stability. This platform was put into operation in 1999, and the improved atom interferometer was used to perform the experiments described in this thesis.

In this chapter, I will briefly describe the atomic beam machine, then the re-designed atom interferometer. The latter description will focus on the newly implemented interferometer platform. Finally, I will discuss the 200 nm period diffraction gratings used for the experiments in this thesis, and present an analysis of smaller period (100 nm) gratings that our group hopes to use in future work.

## 2.2 Beam Machine

Our atomic beam machine (Figure 2-1) consists of three regions: a source region in which the atomic beam is generated, a main region in which the diffraction gratings are arranged, and a detector region in which atom flux is measured.

### 2.2.1 Source Region

The source region is subdivided into three differentially pumped chambers. In the first, the oven chamber, we employ a standard supersonic source [51] to generate an intense beam of sodium atoms. Sodium metal (melting point =  $98^{\circ}\text{C}$ , boiling point =  $883^{\circ}\text{C}$ ) is heated to  $580^{\circ}\text{C}$  in stainless steel oven, generating  $\approx 5$  Torr of sodium vapor. Within the oven, the sodium vapor mixes with  $\approx 1800$  Torr of a carrier gas before expanding adiabatically through a  $70\ \mu\text{m}$  nozzle. The oven chamber is maintained at moderate vacuum ( $< 1$  mTorr) using a Varian VHS-6 diffusion pump. The sodium/carrier gas mixture expands isenthalpically into this vacuum, generating a beam with a peaked velocity distribution ( $\sigma_v/v = 3 - 7\%$ ). The mean velocity of the beam can be varied between 500 and 3000 m/s depending on the choice of carrier gas.

The beam passes via a 0.5 mm diameter skimmer into the second source chamber, maintained at  $1 - 2 \times 10^{-7}$  Torr using a Varian VHS-10 diffusion pump. In this chamber are a series of transverse collimation slits, 5 mm tall and ranging in width between 10 and 50  $\mu\text{m}$  (see “1st slit” in Figure 2-1). Any one of the slits can be translated into the beam path using a manual vacuum feedthrough. An anti-reflection coated glass window allows optical access to the beam just prior to the 1st collimation slit for optical pumping (see Section 3.3.4).

A 2 cm diameter hole opens into the third source chamber, which is held at a pressure  $< 10^{-7}$  Torr by a Varian VHS-4 diffusion pump. A solenoid actuated, mechanical beam block within this chamber acts as a convenient on/off switch for the atomic beam.

The entire source region can be disconnected and rolled away from the rest of the

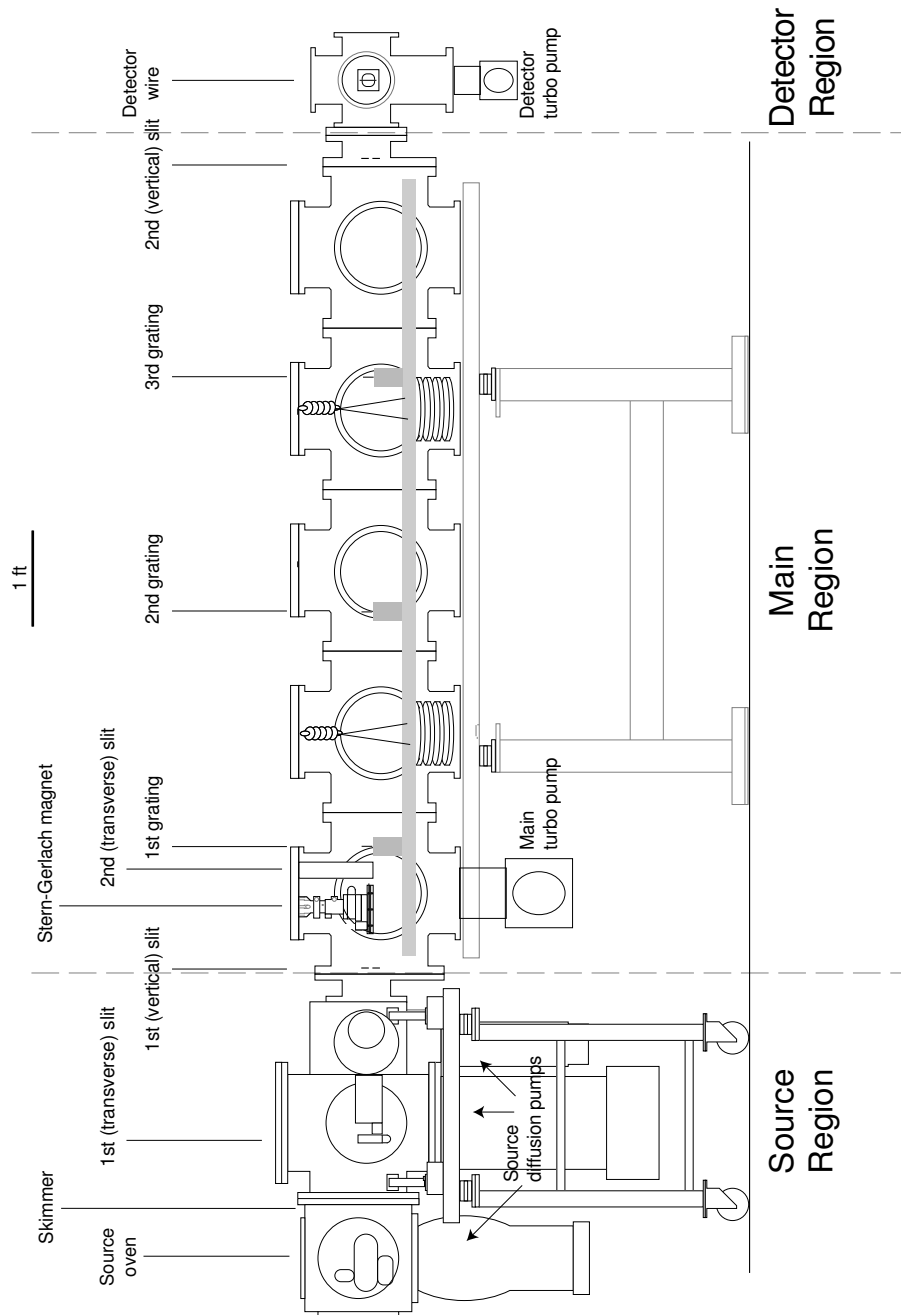


Figure 2-1: Scale drawing of the atomic beam machine housing the MIT atom interferometer. The beam machine is divided into source, main, and detector regions as described in the text. Also shown are the various beam collimation elements, and the interferometer platform (gray).

beam machine on an independent, wheeled frame. Disconnecting the source region is sometimes necessary when inserting/removing the experimental platform into the main region.

### 2.2.2 Main Region

A 1 cm diameter gate valve leads from the source to the main experimental region of our beam machine. The main region of our beam machine consists of five identical six-way crosses, each 20 inches long and with an inner diameter of 12 inches. A  $2 - 3 * 10^{-7}$  Torr vacuum is maintained using a Balzers-Pfeiffer TPU510 turbo pump. When higher vacuum is desired, a cold-finger extending into the chamber is filled with liquid nitrogen creating a cold surface upon which condensibles (such as water) freeze. With the cold-finger, chamber pressures below  $10^{-7}$  Torr are achieved.

The top and side ports of each six-way cross accept standard 10 inch ISO flanges. These interchangeable flanges may have windows for optical access, high-vacuum feedthroughs (i.e. electronic, liquid, gas), or tapped holes as necessary for the experiment at hand. The beam defining elements are mounted from these flanges. These include: a two-wire Stern-Gerlach magnet and a 2nd series of transverse collimation slits (“2nd slit”) identical to those in the source region. Also within the main region are a pair of adjustable height vertical collimation slits — one located near the source region and one near the detector region. Together, the two pairs of collimation slits allow control over the atom beam height (0-3 mm) and width (20-100  $\mu\text{m}$ ). The Stern-Gerlach magnet was used to diagnose optical pumping of the atomic beam.

A rigid platform upon which a three-grating Mach-Zehnder atom interferometer is assembled is suspended within the main region. The platform and interferometer are new for the work reported here and described in detail in Section 2.3.

### 2.2.3 Detector Region

Another 1 cm gate valve leads from the main region into the detector region. In this region, atoms are detected when they hit a vertically oriented, 50  $\mu\text{m}$  diameter

Rhenium wire, resistively heated with a 140 mA current to a temperature of  $\approx 800\text{K}$ . The detector chamber is pumped by its own turbo pump (Varian V-80) and a liquid nitrogen cold trap. Typical pressures in the detector region are  $8 - 9 * 10^{-8}$  Torr.

Because the work function of the wire (7.88 eV) is greater than the sodium ionization potential (5.139 eV), a large fraction ( $> 1/2$ ) of the atoms which hit the wire are ionized. The sodium ions are focused and accelerated via an electric field into a high-gain channeltron electron multiplier (CEM) with an integrated amplifier which outputs a +5 V TTL pulse for each incident ion. The TTL pulses are collected via a computer controlled data-acquisition system. The raw atom beam flux is too large to be accurately measured  $> 1000$  kCounts/sec, but is reduced to between 1 and 100 kCounts/sec when the collimation slits and diffraction gratings are in place.

To keep the hot-wire free of impurities (which can lower its efficiency or lead to undesired background counts) a wire current of 200 mA is maintained between experimental runs, keeping the wire at a temperature near 1000K. Before each run, to increase the ionization efficiency of the hot-wire surface, the detector region is filled with 0.1 Torr  $\text{O}_2$  for two minutes. The hot wire is then turned down in 10 mA increments every 10 minutes until the operating current is reached.

Typical background counting rates, with electric fields optimized for detection of the atomic beam, are between 0.1 kCounts/sec and 1 kCount/sec. Because the hot wire is primarily sensitive to atoms with a small ionization potential (i.e. alkalis), the background count rate is most likely due to residual sodium built up on the chamber walls or adsorbed on the hot wire itself. We typically observe an increased background count rate for several days after the detector chamber has been opened for maintenance, possibly because this residual sodium has been dislodged. The background rate is also higher and exhibits large noise “spikes” just after replacing the CEM detector—decreasing to nominal levels within a week or two. This most likely results from contaminants on the CEM surface which are either pumped away or dislodged by sodium ions as the CEM is used. Finally, the lowest background rates are only obtained when using the liquid nitrogen cold trap, upon which sodium (and other detectable alkalis) freeze.

## 2.3 MIT Atom Interferometer

### 2.3.1 Overview

The MIT atom interferometer is a device which splits matter waves into two coherent components which propagate along spatially distinct paths and are then recombined. For the experiments in this thesis, coherent beam-splitting was accomplished using three 200 nm period transmission gratings (described in Section 2.4). After reviewing how interference fringes are formed and detected, I will describe the newly implemented interferometer platform and discuss some of its advantages and disadvantages.

### 2.3.2 Forming and Detecting an Atom Interference Pattern

Figure 2-2 is a simplified illustration of how atoms are made to interfere, and how that interference is detected. The first of the three diffraction gratings splits incident atom waves into several diffracted orders (with  $> 95\%$  of the atomic probability going into the 0th and  $\pm 1$ st orders). As the diffracted beam propagates towards the second grating, the orders separate transversely, diverging at the diffraction angle  $\theta = \lambda_{dB}/\lambda_g$  where  $\lambda_{dB} = h/mv$  is the deBroglie wavelength of the atoms ( $\lambda_{dB} = 0.06 \text{ \AA}$  for a 3000 m/s sodium atom beam and  $= 0.17 \text{ \AA}$  for a 1000 m/s beam) and  $\lambda_g$  is the grating period. The 0th and 1st diffracted orders are redirected by the second grating. At the third grating, the redirected orders overlap, forming a spatial interference pattern as shown in the inset of Figure 2-2. The third grating acts as a mask; transmitting few atoms when the grating bars are aligned with the maxima of the interference pattern, and many atoms when aligned with the interference minima. (In this Mach-Zehnder geometry, the period of the interference pattern is rigorously equal to the period of the diffraction gratings, if the gratings are equally spaced.)

To measure the atom interference pattern, we recorded the transmitted flux as a function of the phase of the spatial fringes with respect to the third grating bars.

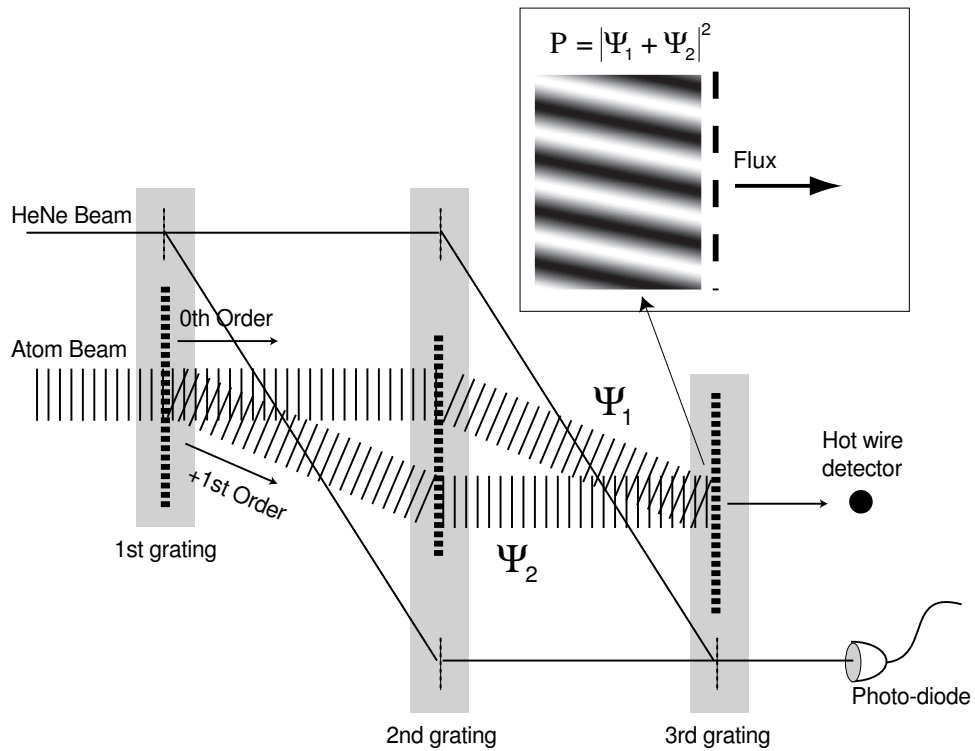


Figure 2-2: Formation and detection of atom interference fringes. The 0th and 1st diffracted atomic orders from the 1st grating are redirected by the second grating and overlap in the plane of the 3rd grating to form a spatial interference pattern. The pattern was detected as the transmitted flux through the 3rd grating, which acts as a mask. A parallel optical interferometer was used to track the relative positions of the atomic gratings.

This phase, called the “grating phase,” is given by [104]:

$$\phi_g = \frac{2\pi}{\lambda_g}(x_1 - 2x_2 + x_3) \quad (2.1)$$

where  $x_i$  is the transverse position of the  $i$ th grating with respect to an arbitrary zero position. A unique feature of the Mach-Zehnder interferometer geometry is that it is “white-fringe,” the grating phase is independent of the velocity of the sodium atoms (i.e. independent of the matter wavelength). We varied the grating phase using a piezoelectric transducer (PZT) to drive the translation stage upon which one of the three gratings is mounted.

Because the PZT has a hysteretic voltage response, and because the grating positions may also vary due to mechanical noise, we required an independent measurement of  $\phi_g$  in order to reconstruct the interference pattern. This measurement was accomplished using a laser interferometer, whose geometry parallels that of the atom interferometer. The optical and atom gratings are fixed to the same mounts so that they move together. The laser interference signal has a phase identical to Eqn. 2.1 with  $\lambda_g$  replaced by the optical grating period ( $\lambda'_g = 3.3\bar{3} \mu\text{m}$ ):

$$\phi'_g = \frac{2\pi}{\lambda'_g}(x_1 - 2x_2 + x_3). \quad (2.2)$$

To measure interference fringes we drove the PZT with a triangle wave (frequency 0.5-2 Hz), then made simultaneous measurements of the atomic flux and optical interferometer phase. The optical phase was used to determine  $\phi_g$  according to the relation  $\phi_g = \phi'_g \lambda'_g / \lambda_g$ . The flux was measured by recording the number of atoms counted in a 1 ms binning interval. Since the bin time was much shorter than the period of PZT driven grating motion, we assumed that the grating phase was constant over an entire bin.

Figure 2-3 shows a high-contrast atom interference pattern plotted as atom flux

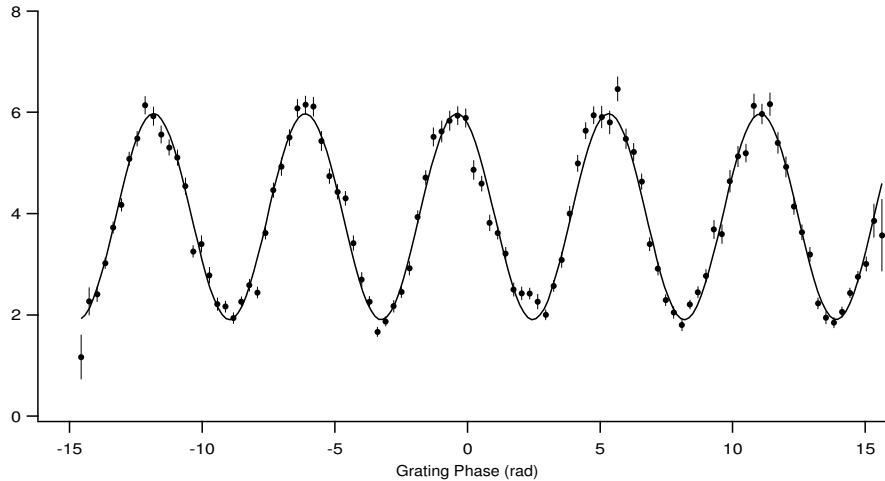


Figure 2-3: High contrast (52%) atom interference fringes obtained from 16 seconds of data (atom flux versus optical interferometer signal). The mean atomic flux is 3.94 kCounts/sec, and the signal-to-noise ratio is 32.4.

versus grating phase. The data are fit to a simple sinusoid:

$$I(\phi_g) = I_0[1 + C \cos(\phi_g + \theta)], \quad (2.3)$$

to determine the mean count rate,  $I_0$ , contrast,  $C$ , and phase,  $\theta$ , of the atom interference pattern. For the experiments described in this thesis, typical contrast values were between 10% and 30%, and mean count rates ranged from 1 – 50 kCounts/sec.

### 2.3.3 Interferometer Platform

The mechanical platform upon which the atom interferometer is mounted was a new innovation for the experiments described in this thesis. Originally, the three matter-wave diffraction gratings were mounted on independent vacuum flanges within the main region. They vibrated with the apparatus, and changed their relative positions as the vacuum chamber was stressed mechanically or thermally. In the new design, the main region accommodates an 8 foot long, 6 inch wide removable optical breadboard upon which the three atom diffraction gratings are mounted. The breadboard is inserted/removed by detaching the main region from the source region and sliding

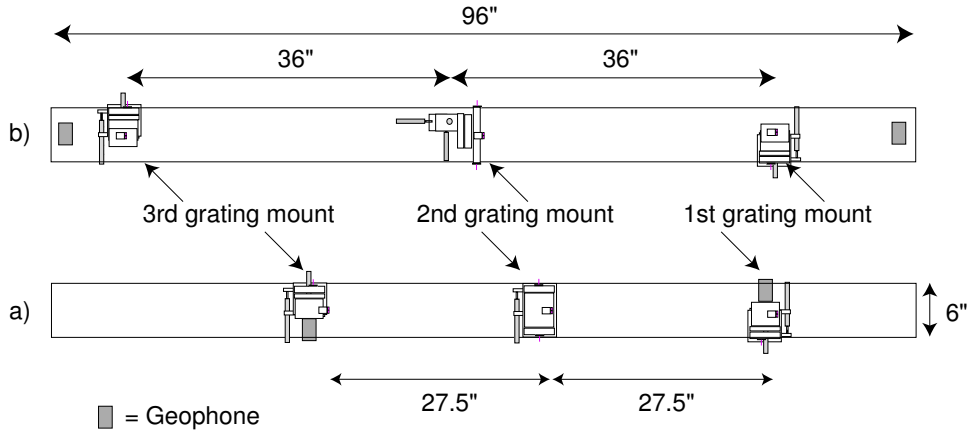


Figure 2-4: Scale drawing of the interferometer platform in two different configurations. The arrangement of diffraction gratings and geophone velocity sensors used for the photon decoherence experiment is shown in (a), while that for the index of refraction experiment is shown in (b). The distance from the 3rd grating to the detector was  $40.5 \pm 0.5$  inches for the photon experiment and  $21 \pm 0.5$  inches for the index of refraction experiment. The 2nd grating mount was redesigned between experiments (see Section 2.3.3).

the breadboard in lengthwise.

Figure 2-4 is a schematic of the breadboard with mounted gratings. All three sets of atom+optical gratings are mounted on motorized translation stages so that they may be moved in and out of the atom beam. Each mount accommodates up to two atom gratings. The extra gratings make available a greater variety of open fractions or allow two independent interferometers using different period gratings to be operated without breaking vacuum. The first and third gratings are mounted on motorized tilt plates which allow them to be rotationally aligned about the atomic beam axis (see Section 2.3.3). The tilt plates have a range of  $\pm 20$  mrad. Also mounted on the breadboard are three geophone velocity sensors, used to monitor the platforms' inertial motion.

Previous studies [54] have suggested that the nanofabricated gratings may, over time, become clogged with sodium or diffusion pump oil carried into the main region from the source. The clogging reduces the grating open fraction, and increases the rms open fraction variation. To minimize clogging, the 1st, 2nd, and 3rd grating

mounts were designed with integrated heaters and temperature sensors connected to a feedback circuit which stabilizes the grating temperatures at 125°C, 100°C, and 90°C, respectively.

The entire breadboard is suspended from two points on the inside of the main vacuum chamber using a modified 4-bar linkage (Figure 2-5). The height of the breadboard could be adjusted via linear motion feedthroughs at both suspension points connected to a lever assembly from which the breadboard hangs. We chose to use only two suspension points to minimize the coupling of mechanical vibrations from the vacuum chamber to the breadboard. Underneath the breadboard, at each of the two suspension points, are held a stack of four stainless steel masses which together more than double the suspended weight from 26 kg to 56 kg. The extra weight serves to lower the resonant frequency of the breadboard’s “bounce” mode, resulting in better high-frequency vibration isolation (see Section 2.3.3).

The 4-bar linkage was designed so that the transverse position of a centered grating does not change when the distribution of weight on the breadboard changes (see Figure 2-5). This factor is important during beam alignment when we do not wish the position of a already aligned grating to be perturbed when another grating is translated into place. With the 4-bar linkage as implemented, the displacement of one grating when another is translated in was typically only a few tens of microns — less than the width of the gratings.

Electrical control lines for the various positioning motors, heaters/thermocouples, piezoelectric transducer, and inertial sensors are connected through a single break-out panel mounted on the board. The outgoing wires are thin gauge and strain-relieved to introduce as little vibration noise as possible.

## **Platform Advantages and Disadvantages**

The advantages of the removable breadboard are threefold:

- *Vibration Isolation* - The random motion of the gratings due to mechanical noise (measured using the parallel laser interferometer) has been reduced from 50 nm rms to 10 nm rms.

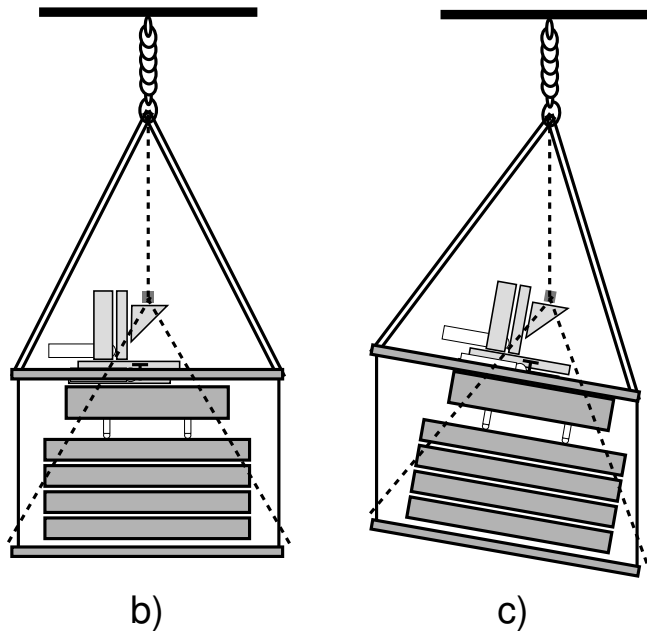
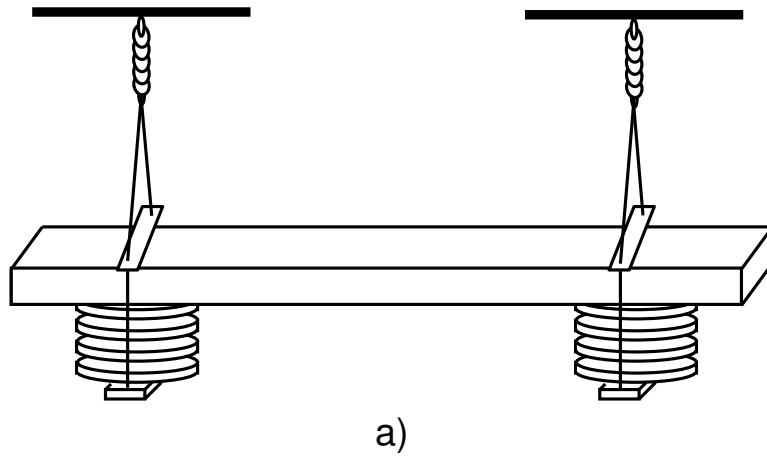


Figure 2-5: Schematic of the suspension system for the interferometer platform. (a) The platform sits on two stacks of stainless steel masses which hang within the main vacuum chamber from a pair of springs. (b) The assembly at each mount point constitutes a “4-bar linkage” which has the unique feature that no matter where the center of mass of the platform, an aligned atom grating will always lie directly underneath the suspension point (c).

- *Improved Grating Alignment* - The gratings can be aligned to  $< 1$  mrad outside the beam machine, eliminating the need for time-consuming in-vacuum alignment.
- *Flexible Interferometer Configuration* - The length of the interferometer and position of the gratings relative to optical access ports can be re-configured to meet changing experimental requirements.

Following a discussion of each of these advantages below, we will describe two unexpected problems with the new design: increased susceptibility to inertial noise and the observation of variable period interference fringes.

### **Vibration Isolation**

Vibration (seismic/acoustic) noise transmitted to the gratings causes them to move relative to each other, resulting in a grating phase that varies erratically in time, resulting in a reduced contrast [104]:

$$C \rightarrow C e^{-\frac{1}{2}\sigma_\phi^2}, \quad (2.4)$$

where  $\sigma_\phi = \frac{2\pi}{\lambda_g}\sigma_x$ , and  $\sigma_x$  is the rms grating motion due to vibrations. Because of the  $\lambda_g$  dependence, the same amount of vibration noise becomes a bigger problem when using smaller period gratings. If vibration noise is present, the signal-to-noise ratio  $S/N = C\sqrt{I_0}$  is reduced, increasing the statistical error bars on any phase/contrast measurement. Although the co-propagating laser interferometer is designed to measure grating motion (including both random and PZT driven motion), only one phase measurement can be associated with each binning period. Thus, motion which occurs on a time scale shorter than the bin time cannot be corrected for with the optical interferometer signal.

For the interferometer as originally constructed in 1991,  $\sigma_x$  was typically 35-45 nm. Major improvements in vibration isolation made in 1995 reduced the typical  $\sigma_x$  to 15-20 nm [54]. The most significant improvement was to hang the entire apparatus

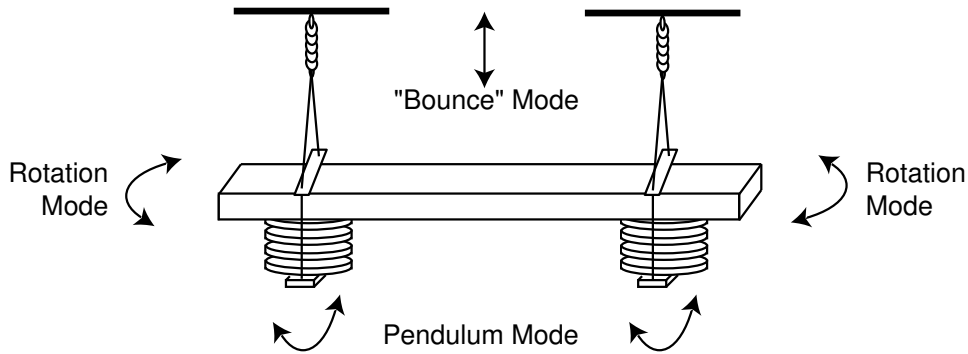


Figure 2-6: The fundamental modes of oscillation of the interferometer platform. The platform is free to bounce up and down on the springs from which it hangs, to swing from side to side as a pendulum, or to rotate about an axis normal to its surface. The resonant frequency of the “bounce” mode is  $\approx 5$  Hz, of the pendulum mode is  $\approx 1.5$  Hz, and of the rotation mode  $\approx 2$  Hz.

from the ceiling of the lab. The “pendulum” mode of the hanging apparatus acts as a low-pass mechanical resonator which attenuates any vibrations with frequency above its sub-hertz resonance. Other routes from vibration sources to the gratings (i.e. vacuum and cooling lines, electrical connections, airborne acoustic waves) short circuit the pendulum and continue to contribute to grating motion.

The vibration isolation of the new breadboard improves upon the previous design. We have incorporated two separate stages of isolation: a pendulum of resonant frequency  $\simeq 1.5$  Hz and a set of springs with resonant frequency  $\simeq 5$  Hz (see Figure 2-6). The only short circuit around these mechanical resonators to the gratings is through electrical connections made inside of the vacuum chamber. These improvements have further reduced  $\sigma_x$  to  $\approx 10$  nm, without the need for to suspend the entire 1.5 ton vacuum apparatus. At these noise levels, it has proven possible to observe high-contrast interference fringes with 100 nm period gratings (see Section 2.4).

### Improved Grating Alignment

The contrast of an atom interference pattern depends critically on the rotation alignment of the three diffraction gratings. Intuitively, if the gratings are misaligned by

half a grating period over the height of the atomic beam ( $100 \text{ nm}/1 \text{ mm} = 0.1 \text{ mrad}$ ), then the interference fringes formed at the top and bottom of the beam will be  $180^\circ$  out of phase and cancel each other out. A complete derivation of the contrast reduction as a function of beam height and grating misalignment can be found in the thesis of C. Ekstrom [34].

Once the gratings are nearly aligned, their rotation can be optimized by maximizing contrast with respect to small adjustments in the grating rotation. However, this requires that the gratings are sufficiently aligned that some contrast can be measured. Even using the smallest possible beam height that still provides a reasonable signal ( $\approx 0.1 \text{ mm}$ ) this implies that the gratings must be aligned to  $\approx 1 \text{ mrad}$  before they are installed in the vacuum chamber or that a time-consuming 2-dimensional search in rotation space must be performed.

When the gratings had been mounted on independent vacuum flanges, the initial alignment procedure consisted of mounting each flange upside down (with the grating outside the chamber), then observing the diffraction of a HeNe laser beam through the grating's  $2 - 4 \mu\text{m}$  support structure (see Section 2.4). The gratings were rotated until the diffracted spots from each lined up on the same vertical plumb. The ultimate accuracy of this technique was limited by the fact that the flanges themselves could not be reproducibly mounted to better than a few mrad. This resulted occasionally in multiple-day experimental runs being required to discover the correct rotation alignment.

Mounted on the breadboard, the gratings can now be aligned to  $< 1 \text{ mrad}$  routinely using the same HeNe diffraction technique as before. Because the board is rigid, this alignment is preserved once the board is inserted into the chamber. We have had remarkable success with this alignment procedure: after a new set of gratings has been installed, we typically have needed to search only for an hour or two to find a small atom interference signal (using the reduced height atom beam).

An additional alignment consideration is the longitudinal spacing between gratings. When the distance between the first and second gratings is different from that between the second and third gratings ( $\Delta L = L_{12} - L_{23} \neq 0$ ), the difference in path

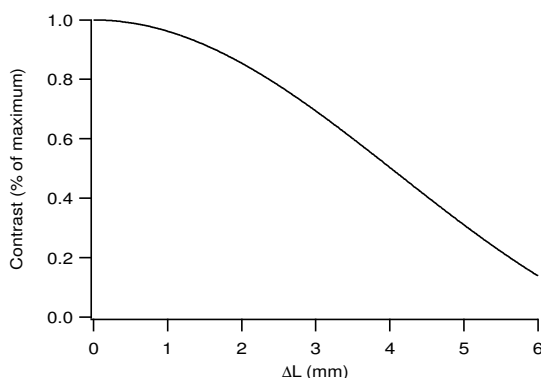


Figure 2-7: Interference contrast plotted as a function of longitudinal spacing error  $\Delta L$  (see Eqn. 2.5). Parameters from the photon decoherence experiment were used for this calculation:  $L = 27.5$  in.,  $w_s = 0.02$  mm,  $w_d = 0.05$  mm, and  $\lambda_g = 200$  nm.

length between the two arms of the interferometer is no longer velocity independent (i.e. the “white-light” character of the interferometer is destroyed). The reduction in contrast as a function of this grating spacing error is given by [23]:

$$C = C_0 \left| \text{sinc} \left( \frac{\pi w_s \Delta L}{\lambda_g L} \right) \text{sinc} \left( \frac{\pi w_d \Delta L}{\lambda_g L} \right) \right|, \quad (2.5)$$

where  $w_s$  and  $w_d$  are the widths of the 2nd collimating slit and detector respectively, This function is plotted in Figure 2-7 as a function of  $\Delta L$  for typical experimental parameters.

Again, because of inaccuracy in the placement of the large vacuum flanges on which the gratings were mounted, the spacing error is estimated to have been as large as 1-2 mm resulting in a 4–15% contrast reduction. In the current design, the grating spacing can be adjusted with high-precision ( $< 1$  mm) outside the vacuum chamber, and will remain accurate after insertion into the main chamber.

### Flexible Interferometer Configuration

For many atom interferometry experiments, it is necessary to introduce electromagnetic fields or additional atom optics, at specific positions with respect to the atom gratings. Because the location of the additional elements is limited by available

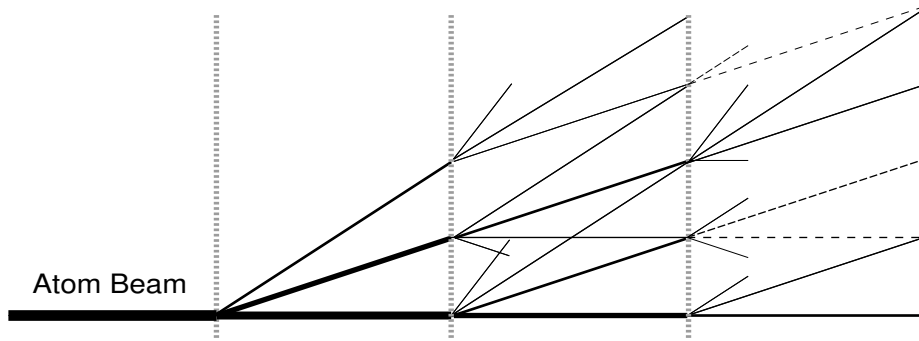


Figure 2-8: Schematic of a three-grating Mach-Zehnder interferometer showing some of the additional diffraction orders not considered in a simple two-path description of the interference signal. This more complete picture indicates the presence of more than one set of interfering paths (dashed lines). Also shown are other diffracted orders which do not contribute to any interference signal, but merely add to the background count rate and thus reduce the signal/noise ratio. Line thickness corresponds to the amplitude of a given path.

vacuum ports/windows or interior mount points, it is extremely valuable that the breadboard design allows gratings to be placed at any desired position within the chamber.

In this thesis, the decoherence experiment (Chapter 3) required optical access just in front of the third grating, and the index of refraction experiment (Chapter 4) required mounting a thin target-gas cell from an upper vacuum flange just before the second grating. Both of these arrangements, which would have been difficult to implement using the previous interferometer apparatus, were easily accomplished by adjusting the grating positions on the breadboard.

This flexibility can also be used to increase the signal to noise. The simple picture of two-path interference is complicated by the various other orders that are generated by the diffraction gratings as depicted in Figure 2-8. By choosing the distance between gratings and between the third grating and the detector appropriately, we can minimize the contribution of unwanted orders that overlap with the desired interference order in the detector plane [23].

## Susceptibility to Inertial Noise

One drawback of the new design is that the board is essentially unconstrained in the horizontal direction and its rotation mode (see Figure 2-6) is easily excited via low frequency noise. Because all three gratings are moving together, this mode does not contribute to an increased  $\sigma_x$ , nor does it effect either  $\phi_g$  or  $\phi'_g$ . However, it does cause a phase variation via the Sagnac effect [71, 54]. Just as before, this phase variation results in lower signal-to-noise and contrast fluctuations. The effect of Sagnac phase variations on contrast is described by Eqn. 2.4 with:

$$\sigma_\phi = \frac{4\pi m L^2 \lambda_{db} / \lambda_g}{h} \sigma_\Omega, \quad (2.6)$$

where  $m$  is the sodium mass,  $L$  is the distance between gratings, and  $\sigma_\Omega$  is the rms rotation rate of the breadboard.

To monitor the Sagnac rotation phase we mounted inertial sensors on the breadboard which produce a voltage proportional to velocity, and were used to measure the rotation of the board in the same way that the laser interferometer measures relative grating position. Using the sensors, we have measured  $\sigma_\Omega$  under standard experimental conditions (vacuum pumps turned on, water flowing through cooling lines, etc...) and typically less than 1% contrast loss for  $\lambda_g = 200$  nm period gratings. This measurement was made during the evening when most of our interference data is typically collected.<sup>1</sup>

## Observation of Variable Period Fringes

In a properly aligned, three grating Mach-Zehnder interferometer, the spatial period of the interference fringes is rigorously equal to the period of the diffraction gratings. However, our first interference fringes taken using the redesigned interferometer seemed to have a different period than the diffraction gratings. This early interference

---

<sup>1</sup>During daylight hours when there is more outside activity to cause low frequency seismic noise, the contrast loss due to rotation can be much greater. As a result, it has been impossible to collect interference data during the daytime over the past year, especially because construction activity in the lot adjacent to the building housing the atom interferometer.

data was best fit using a modified form of Eqn. 2.3:

$$I(\phi_g) = I_0[1 + C \cos(\beta\phi_g + \theta)], \quad (2.7)$$

where  $\beta$ , the inverse period of the atom interference fringes, varied between 0.5 and 3 as opposed to the expected value 1.

Further investigation revealed several notable features of this variable period problem:

- The best-fit value of  $\beta$  was most significantly different from unity just after a tilt adjustment of whichever grating was being driven by the PZT (for these observations, the 1st grating).
- The best-fit value of  $\beta$  depended strongly on the frequency and amplitude of the PZT drive.
- We consistently observed  $\beta < 1$  when interference data was taken while the PZT was retracting (i.e. the voltage applied to the PZT was decreasing). Conversely, we consistently observed  $\beta > 1$  when interference data was taken while the PZT was extending (i.e. the voltage applied to the PZT was increasing).

These observations are summarized in Figure 2-9 which shows the best-fit value of  $\beta$  as a function of time after making a tilt adjustment. Three sets of data were taken at different PZT “slopes” (amplitude times frequency of the PZT drive voltage), with the smallest slope showing the largest deviation from  $\beta = 1$ . Each set of data is also split into two groups (shown in black versus gray on the plot) depending on whether the PZT drive voltage was increasing or decreasing while a particular fringe was acquired.

Our best hypothesis for the origin of this variable period problem is that PZT was not only translating the desired grating back and forth, but was also driving the breadboard’s rotation mode (see Figure 2-6). Such driving would not be surprising given that grating mount being moved by the PZT was heavy ( $\approx 6$  kg) and located close to one end of the breadboard. Any rotation of the breadboard will add an

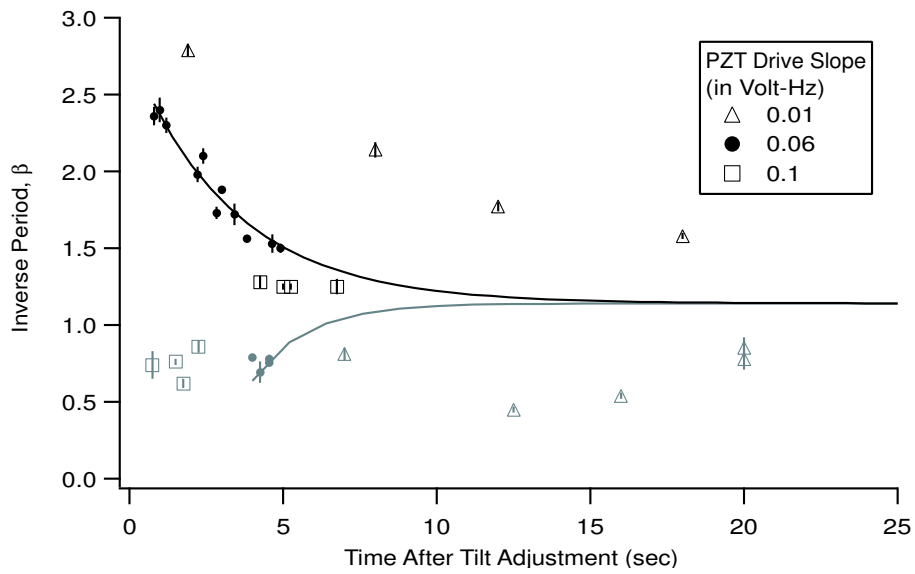


Figure 2-9: Inverse period of atom interference fringes,  $\beta$ , plotted versus the number of seconds after having made a tilt adjustment that the fringe data was taken. The legend indicates at which of three different PZT “slopes” (amplitude times frequency of the PZT drive) the data was collected. The black (gray) symbols indicate data acquired while the PZT drive voltage was increasing (decreasing).

oscillating Sagnac phase to the atom interference pattern whose sign depends on the sense of the rotation (and therefore on the direction of PZT travel). This additional phase will cause more/fewer oscillation of the atom interference signal to be observed in a given time interval, giving the appearance of increased/reduced period fringes.

This hypothesis does not fully explain all of the experimental observations. For example, the dependence on time after a grating tilt adjustment is not clear. Unfortunately, the geophone velocity sensors mounted on the breadboard could not be used to confirm that the board was indeed rotating because they lose sensitivity below 5 Hz (the PZT drive frequency was  $\leq 1$  Hz).

Our solution to this problem was to first change our operating configuration so that the 2nd atom grating, the closest to the middle of the breadboard, was the one being driven by the PZT. This change had the added advantage that the same amount of grating phase shift could be applied with only half the absolute motion of the PZT (see Eqn. 2.1). We also redesigned the 2nd grating mount to reduce the mass being driven by the PZT from 6 kg to  $< 1$  kg. Since these modifications, the best-fit value of  $\beta$  has consistently been within error of unity.

## 2.4 Diffraction Gratings

### 2.4.1 Overview

Nanofabricated diffraction gratings are the enabling atom-optical technology for our interferometer. An SEM micrograph and schematic of one of the 200 nm period gratings used for the experiments in this thesis is shown in Figure 2-10. The grating is formed in a thin (100 nm) silicon nitride membrane lying on top of a thicker 250  $\mu\text{m}$  silicon substrate. A window (typically 3-5 mm tall and 40 – 500  $\mu\text{m}$  wide) is etched into the silicon to allow the atoms to pass unobstructed through the grating. The support structure visible in the SEM image is necessary to keep the grating bars from warping or breaking. Between 3 and 6 grating windows are fabricated together on an  $\approx 1 \text{ cm} \times 1 \text{ cm}$  chip.

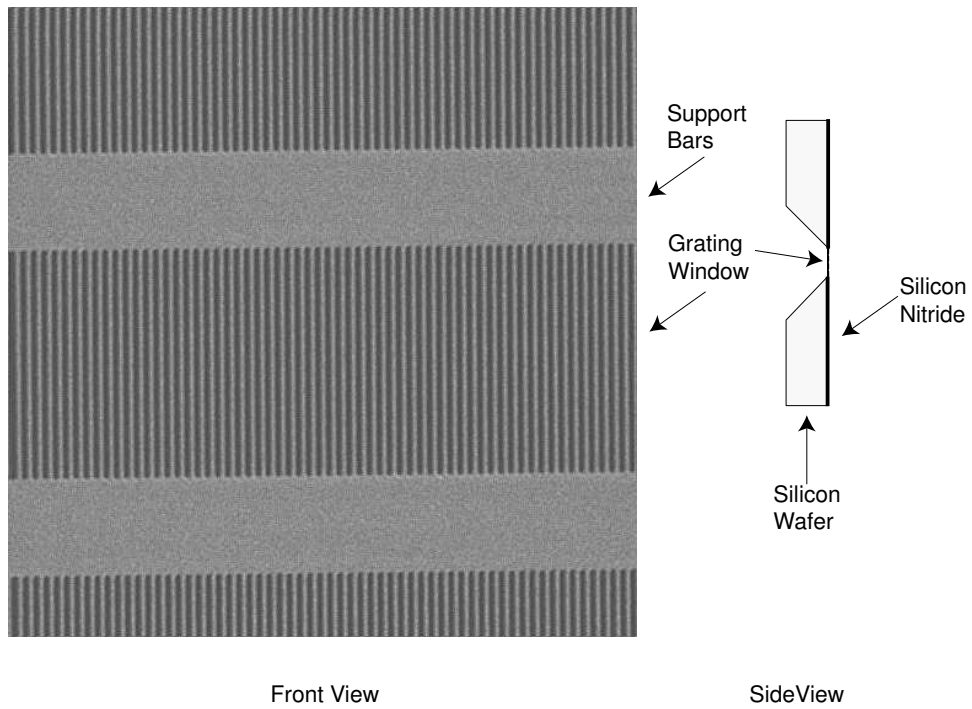


Figure 2-10: (Left) SEM micrograph of a 200 nm period atom diffraction grating fabricated by former members of this group in collaboration with staff of the National Nanofabrication Facility at Cornell University. The period of the horizontal support structure is  $6.5 \mu\text{m}$ . (Right) The diffraction grating is written into a 100 nm thick silicon nitride membrane atop a standard ( $250 \mu\text{m}$  thick) silicon wafer. A window has been etched into the silicon wafer that atoms may pass through it.

Matter-wave diffraction gratings have been fabricated using two different techniques: electron beam (e-beam) lithography and achromatic interferometric lithography (AIL). The e-beam technique was developed by our group in collaboration with staff of the National Nanofabrication Facility in Cornell (particularly Mike Rooks), and used to make a large number of 400, 200, 160, and 140 nm period gratings [62, 96]. The e-beam process, refined over several years, consistently produces high-quality gratings, but suffers from the drawback that it takes several hours to write a single grating chip.

The AIL technique was developed by the group of Prof. H. Smith of the MIT Electrical Engineering Department, and has been used to create gratings both for atom optics experiments and x-ray diffraction/spectroscopy. It involves generating a standing wave optical interference pattern using two laser beams at a large angle of incidence [102]. So far, only 100 nm period gratings have been produced, although a project to create 50 nm period gratings is underway. The main advantage of AIL is the ability to expose an entire wafer (up to 10 grating chips) at once, using relatively standard optical lithographic components. As we will see below, the AIL gratings produced thus far not been suitable for atom interferometry, but refinements to the process continue and there is an active effort to improve AIL grating quality to the level of the e-beam gratings.

Although the gratings used for the experiments in this thesis were all fabricated at NNF by previous graduate students using the e-beam technique, significant effort over the past few years has been devoted to evaluating AIL gratings and providing feedback on their design. The remainder of this section will discuss the evaluation of the most recently studied (“2nd generation”) 100 nm period gratings. We begin with a discussion of the important parameters that determine grating quality (for the purposes of atom interferometry). We then present atom diffraction and interference studies of the new AIL gratings. We end with a comparison of e-beam gratings and the two generations of AIL gratings.

## 2.4.2 Important Grating Parameters

When evaluating gratings for use in the atom interferometer, we are primarily concerned with three factors: open fraction, open fraction variation, and phase coherence.

### Open Fraction

The contrast observed in our atom interferometer depends on the open fraction,  $f$ , (ratio of gap width to grating period) of the gratings comprising it. The optimal open fractions, determined by maximizing the signal to noise ratio of the detected fringes, are between 0.4 and 0.6, varying slightly depending on the experimental configuration (atom beam collimation, distance between gratings, distance from the last grating to the detector, and velocity of the sodium beam). We have developed a numerical simulation to predict the theoretical maximum contrast as a function of grating open fractions for any given interferometer configuration. We used this simulation to choose from among the open fractions available in our grating inventory. Table 2.1, reproduced from Ref. [54], lists the contrast and signal-to-noise ratios expected for a variety of open fractions in two different interferometer configurations. Typically, 60% - 70% of the calculated maximum contrast is measured experimentally, with losses attributed to one of two possible sources: apparatus imperfections (i.e. vibrations, rotation noise, and stray magnetic field gradients) and grating imperfections (i.e. variations in the grating bar widths and positions).

### Open Fraction Variations

If the open fraction of a grating is not uniform over its face, there will be an exponential damping of intensity in the higher order diffraction peaks (see Appendix A):

$$\frac{I_n}{I_0} = e^{-(n\pi\sigma_f)^2} \text{sinc}^2(n\pi f), \quad (2.8)$$

where  $I_n$  is the intensity of the  $n$ th order diffraction peak and  $\sigma_f$  is the rms variation in open fraction. The intensity lost in the higher order diffraction peaks appears as a broad, incoherent background peak centered around the 0th order. Since, the

$f_1$	$f_2$	$f_3$	S/N	Contrast (%)	Note:
Slow Atom Beam Configuration					
0.56	0.50	0.37	41.4	65.4	Best
0.48	0.48	0.48	38.2	59.0	Best, all same $f$
Fast Atom Beam Configuration					
0.60	0.43	0.37	92.1	29.5	Best
0.43	0.43	0.43	82.8	30.4	Best, all same $f$

Table 2.1: Comparison of signal-to-noise ( $S/N$ ) and contrast predicted for gratings with different open fractions for two different interferometer configurations from Ref. [54]. The upper three rows refer to a slow atomic beam configuration ( $v = 1000$  m/s, using  $20 \mu\text{m}$  collimating slits). The lower three rows refer to a fast beam configuration ( $v = 3000$  m/s, using  $50 \mu\text{m}$  collimating slits). In both configurations, the distance between gratings was  $66$  cm, and the distance from the third grating to the detector was  $29$  cm. “Best” implies highest signal to noise ( $S/N$ ) for the configuration.  $S/N$  values depend on the (velocity-dependent) atom beam flux, and are therefore not comparable between the configurations.

largest possible contrast is, in general, achieved when the intensity of the first order diffraction peak is maximized, significant open fraction variation can substantially reduce contrast (see Figure 2-11).

### Phase Coherence

In order to observe high-contrast interference, the phase of the interfering matter waves must be uniform over their entire transverse area. Because the gratings essentially imprint a phase onto the matter wave, this becomes a requirement on the phase coherence of the gratings. A collimated atomic beam is typically  $\approx 1$  mm tall and  $\approx 30 \mu\text{m}$  wide, thus, for optimal contrast, the phase of the grating bars must be uniform over this entire area. If the phase of the grating bars drifts by  $\pi$  radians (i.e.  $100$  nm displacement of the grating bars relative to their ideal location) over the  $1$  mm beam height, no contrast will be observed. We therefore require phase coherence at the several ppm level in order to observe interference.

Phase errors come about in different ways for the two fabrication techniques. In the electron beam case, they arise when there is drift or an abrupt shift in the position of the electron beam when writing a grating [54]. In the AIL case, phase errors result from imperfections in the optics used to collimate and focus the laser light used to

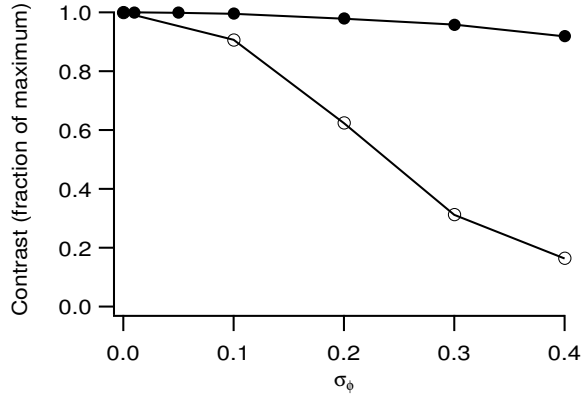


Figure 2-11: Contrast loss due to rms open fraction variation,  $\sigma_f$ . The nominal open fractions are those listed as “Best” in Table 2.1. Solid circles (●) refer to the slow atom beam configuration, and open circles (○) to the fast atom beam configuration.

form the optical standing wave.

### 2.4.3 Characterization of 100 nm Period Gratings

In the thesis of T. Hammond [54], a set of 100 nm period diffraction gratings “1st generation” was studied. Disappointingly low contrast was observed and was attributed poor grating quality combined with experimental factors such as clogging of the smaller period gratings with diffusion pump oil. We have recently studied two sets of 2nd generation 100 nm gratings that benefit from several changes to the fabrication process meant to improve their phase coherence and reduce open fraction variation. For identification purposes, the most significant difference between the two sets of gratings we studied was the width of the free-standing silicon-nitride grating window: 0.2 mm in one case, and 1 mm in the other.

#### Expected Performance of 0.2 mm Wide Gratings

The open fraction of the gratings was determined prior to the search for interference by performing fits to atomic diffraction patterns such as Figure 2-12. We were pleased to observe, in high-resolution scans, up to seventh order diffraction peaks. The open fraction of all the grating windows we examined was found to be roughly constant.

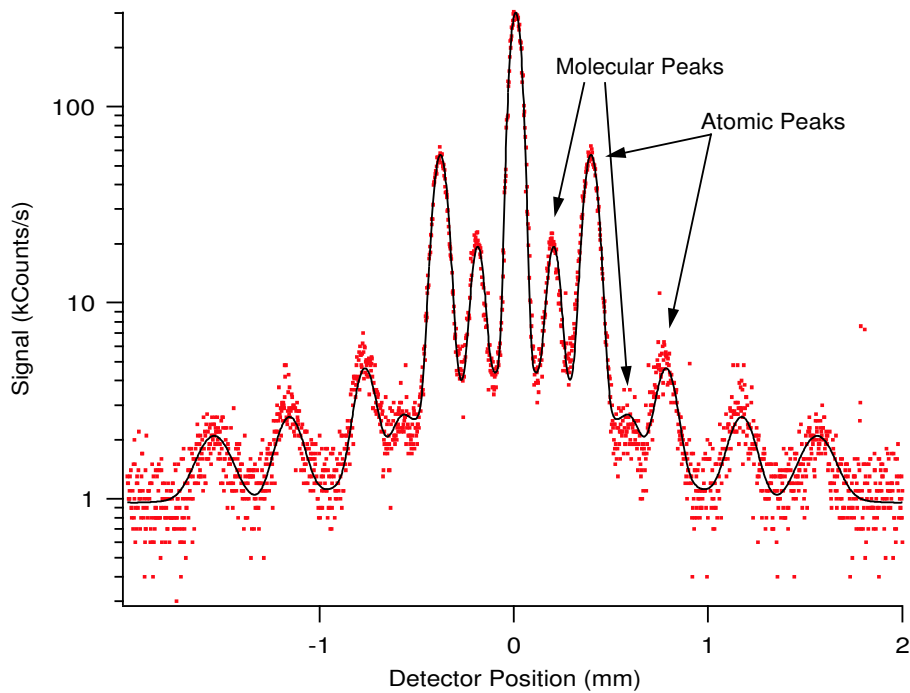


Figure 2-12: Sodium diffraction data taken with 0.2 mm wide, 100 nm period transmission gratings. Solid line is a least-squares fit which determines the open fraction to be  $59.0 \pm 0.3\%$

The gratings windows we eventually used to search for interference had open fractions  $f_1 = 59\%$ ,  $f_2 = 58\%$ ,  $f_3 = 58\%$ . The measured diffraction patterns also place a limit on the open fraction variations in these gratings:  $\sigma_f < 0.1$ , albeit with some uncertainty due to theoretical subtleties in modeling the effect of open fraction variation on diffraction patterns. These parameters yield a predicted contrast of 39.5% for the interferometer geometry shown in Figure 2-4a, using a fast atom beam configuration ( $v = 3000$  m/s using  $50 \mu\text{m}$  collimating slits) and 49.8% for a slow atom beam configuration ( $v = 1500$  m/s using  $20 \mu\text{m}$  collimating slits).

### Measured Performance of 0.2 mm Wide Gratings

With the gratings rotationally aligned to better than 0.1 mrad we observed 13.9% contrast in the fast ( $v = 3000$  m/s) atomic beam configuration, 38% of the predicted value. We obtained this contrast only when the atomic beam was vertically restricted

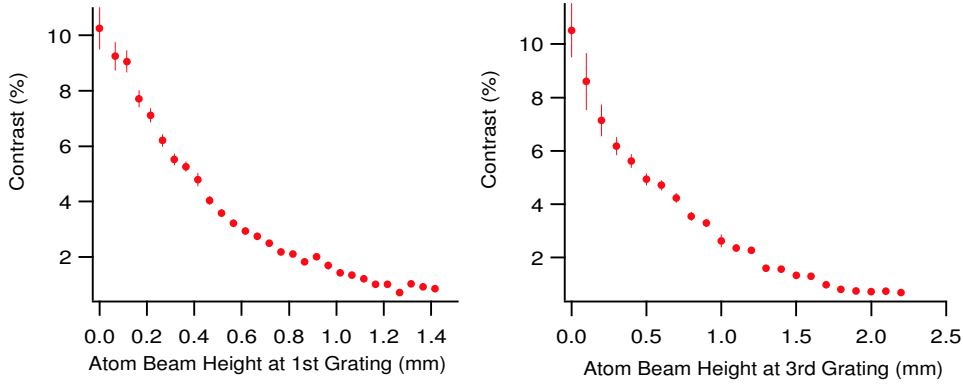


Figure 2-13: Contrast versus height of the atomic beam at the position of the first grating (left) or third grating (right). In both cases, the interferometer is operating in the fast atomic beam configuration ( $v = 300$  m/s) with 0.2 mm wide 100 nm period gratings. While the height of the beam at the 1st (3rd) grating was varied, the height at the 3rd (1st) grating was held constant at  $\approx 0.1$  mm.

to a height of 50  $\mu\text{m}$ . As shown in Figure 2-13, the contrast decreased to less than 1% when we attempted to use the entire 1 mm height of the atomic beam.

In a slower (1500 m/s) neon separated beam configuration, we observed 8% contrast with a 1 mm tall atomic beam. (The lower flux of a neon seeded beam made it impossible to further decrease the atomic beam height.) This is only 16% of the expected value. Our observation of a relatively smaller fraction of expected contrast for the slow versus the fast atomic beam configuration suggests that up to 50% of the contrast lost may have been due to inertial noise, the magnitude of which scales exponentially as  $\lambda_{db}^2$  or  $v^{-2}$  (see Section 2.3.3).

### Analysis of 0.2 mm Wide Gratings

The strong variation in contrast as a function of beam height indicates one of two potential problems: the gratings were not well-aligned rotationally, or there is a phase/period variation in the grating as a function of height. The first alternative can be entirely ruled out:

- The exhaustive search through rotation space for the correct alignment, with resolution better than 0.1 mrad. (This misalignment would cause only  $\approx 5\%$

reduction in contrast.)

- Widening the beam on either the first or third gratings resulted in a contrast reduction of roughly the same magnitude. This implies that both first and third gratings would have to have been misaligned with respect to the second grating.
- We observed a variation in contrast as we scanned the atomic beam from top to bottom of the third grating, with beam height held constant. Because, in this case, the height of that atomic beam does not change, this observation cannot be accounted for by rotation misalignment.
- We observed that the phase of the interference remains constant as a function of vertical position. This observation is not consistent with a rotation error, which would cause a linearly varying phase as a function of vertical position.

The strong implication from these observations is that these 100 nm gratings suffered from poor phase coherence. While this may have been due to residual problems in the fabrication process, it is also possible that our mechanism for mounting the gratings may have caused or exacerbated a vertical variation in phase/period. In these experiments, the grating chip was held in place within the vacuum apparatus by clamping one edge. The force of the clamp may have stressed the silicon nitride membrane forming the grating, causing it to warp or spread. To avoid the stressing the membrane, we now epoxy the entire chip to a small aluminum mount. This not only eliminates the clamping stress, but also permits easy handling of these delicate structures.

### **Performance of 1 mm Wide Gratings**

In analyzing diffraction (e.g. Figure 2-14) from the 1 mm wide gratings, three features came immediately to our attention:

- In contrast to the 0.2 mm wide gratings, diffraction peaks beyond the first order were barely visible.

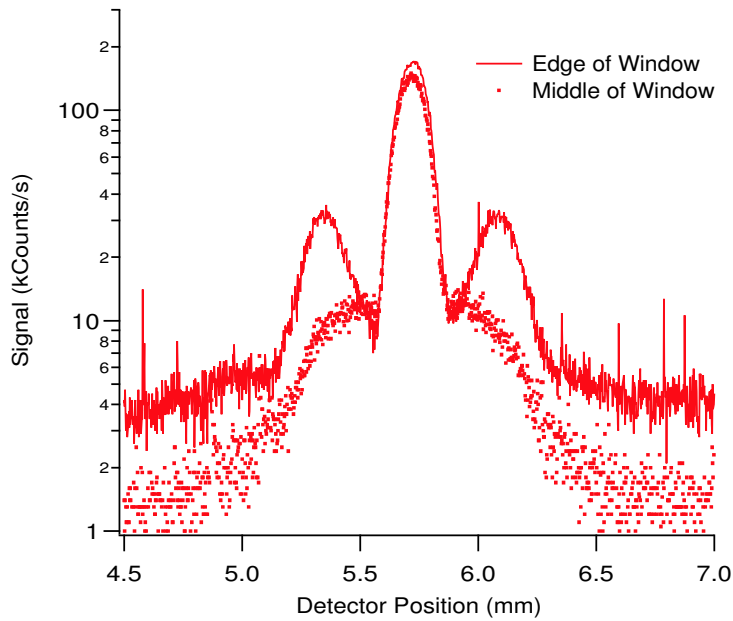


Figure 2-14: Two diffraction patterns obtained from a single 1 mm wide 100 nm grating. The diffraction pattern taken with the atomic beam passing through the edge of the window ( $\approx 0.48$  mm from the center) shows first order diffraction peaks corresponding to a 65% open fraction ( $\sigma_f \approx 0.1$ ). The diffraction pattern taken with the atomic beam passing through the center of the window shows first-order diffraction peaks corresponding to a 73% open fraction ( $\sigma_f \approx 0.3$ ). The smearing of the peaks in the latter case is explained by the large open fraction variation. The difference in overall background count level between the two patterns is related to detector conditions and is not important.

- There was strong variation in open fraction over the face of the grating: typically 73% in the middle of the grating window and 65% on the edges.
- The  $\approx 70\%$  open fraction of these windows are not ideal for a high-contrast interferometer, yielding signal-to-noise ratios an average of two to three times smaller than for a set of three 48% open gratings.

Given the poor quality of the 1 mm window diffraction patterns, we made only a brief, unsuccessful attempt to look for interference with these gratings.

## Analysis of 1 mm Wide Gratings

Our measurements conclusively demonstrate that the open fraction in the middle of these gratings is significantly larger than on the edges. Two possible explanations are: non-uniform exposure or etching of the grating bars during fabrication, or a large number of broken bars in the middle of the grating window. Given a large open fraction variation, the inability to observe higher order diffraction peaks follows directly from Eqn. 2.8.

We examined the 1 mm gratings in using a SEM, and found that most of the bars in the middle of the grating window were either broken or stuck together (see Figure 2-15). Because this damage was not observed when the gratings were initially examined in the SEM (just after fabrication), we hypothesized that their unusually large width made them especially susceptible to damage during handling/experimentation. The graduate student who fabricated the gratings (Tim Savas), suggested that the warping of the grating bars might have resulted from mistakenly applying the gratings' silicon nitride layer under compression rather than under tension as is usual (and necessary for the bars to remain straight).

### 2.4.4 Conclusion

Our attempts to use 100 nm diffraction gratings in the atom interferometer are summarized in Table 2.2. We have discussed our results with Prof. Smith's group and, as a result, several improvements to the AIL process for grating fabrication have been implemented including narrower and smaller period support structure, smaller window width, and better alignment of the standing wave optics. We have received a set of 3rd generation 100 nm period gratings that incorporate these improvements, but have not yet attempted to use them in the atom interferometer. Such an attempt will be carried out by subsequent graduate students on this project.

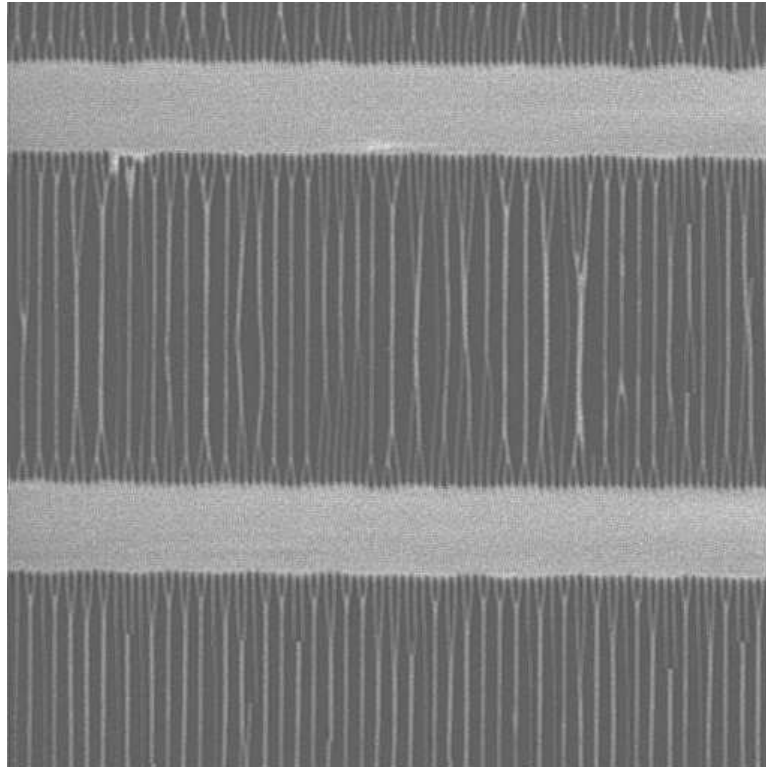


Figure 2-15: SEM micrograph of the 1 mm wide 100 nm period grating corresponding to the diffraction pattern in Figure 2-14. This image (taken near the center of the grating window) reveals that nearly all of the grating bars are stuck together, explaining the large open fraction variation inferred from sodium diffraction patterns.

	1st Generation	2nd Generation (0.2 mm Wide)	2nd Generation (1 mm Wide)
Tested By	T. Hammond (1996)	D. Kokorowski (1999)	D. Kokorowski (1999)
Open Fraction	62%	58%	65-73%
Measured Contrast (fast beam configura- tion)	2.9%	14.9%	No contrast
(slow beam configura- tion)	4.8% (1000 m/s)	8% (1500 m/s)	No contrast
Predicted Contrast (fast beam configura- tion)	10.4%	39.2%	
(slow beam configura- tion)	37.0% (1000 m/s)	50% (1500 m/s)	

Table 2.2: Summary of our measurements of atom interference using 100 nm period gratings. With these gratings, we have only been able to obtain 10-40% of the theoretically predicted contrast, compared to typically 60-70% using 200 nm gratings fabricated using e-beam lithography.

# Chapter 3

## Measuring Decoherence with an Atom Interferometer

### 3.1 Introduction

This chapter presents a series of experiments related to decoherence in an atom interferometer. Decoherence arises because no quantum system can be completely isolated from its environment (which formally consists of everything in the universe other than the system itself). Decoherence is the result of interactions between a quantum system and this external environment, and manifests as the transformation of coherent quantum superpositions into incoherent mixtures. In the context of separated beam atom interferometry, decoherence refers to those interactions between an atom and its external environment (e.g. E-M fields, background gas particles, or material structures) that destroy the spatial coherence between the two interfering paths.

#### 3.1.1 Motivation

There are several reasons for ongoing study of the phenomena surrounding decoherence. It is of general interest to understand how quantum mechanics reduces to classical mechanics in the macroscopic world. Decoherence is a fundamental limit to

large-scale quantum computation [118] and communication [17] and must be overcome before such devices can be practical. Finally, decoherence has thus far been studied only in a few, relatively simple systems, many of which exhibit common behavior. A wealth of phenomena predicted using decoherence theory has yet to be explored experimentally, even in a qualitative way [7].

Reasons to study photon scattering as a cause of decoherence, and in particular to extend previous studies from the single- to the multiple-photon regime include the following:

- Photon scattering is one of the most significant causes of decoherence for the macroscopic objects of everyday life (see Table 3.2).
- The atom-photon interaction is well understood quantum mechanically. Unlike more complicated systems, the results of a photon decoherence experiment can be compared to first-principles calculations of the expected decoherence rate. No such explicit comparison with theory has been performed in the many-photon limit.
- In the many-photon limit, photon decoherence exhibits the same general behavior as predicted for many other decohering environments. In the single-photon limit, photon decoherence exhibits qualitatively different behavior. The transition between these two has never been explored.

### 3.1.2 Chapter Outline

After a brief overview of the main concepts of decoherence theory and previous experimental work, four decoherence experiments employing the atom interferometer are discussed:

- A measurement of decoherence due to spontaneous photon scattering (Section 3.3).
- A measurement of decoherence due to two successive photon scattering environments (Section 3.3.4).

- A measurement of decoherence due to background gas scattering (Section 3.5).
- A comparison between the decoherence due to a photon scattering environment and the dephasing (a “decoherence-like” loss of contrast) caused by deterministic scattering from a diffraction grating (Section 3.6).

## 3.2 Theory and Previous Experiments

### 3.2.1 General Decoherence Theory

The theory of decoherence is an attempt to explain the “difference in appearance between quantum and classical [behavior] under the assumption of a universally valid quantum theory” [131]. It arose from the observation that not all conceivable quantum superpositions are found in nature. For example, superpositions of states with different electric charge or of integer and half-integer spin are allowed quantum mechanically but have never been directly observed. And superpositions of macroscopically distinct states (Schroedinger cat states) have been observed only fleetingly.

The first attempts at a theory of decoherence consisted of postulated “superselection rules” that excluded the never-observed superpositions either on an ad hoc basis [126, 127, 112], or on the hypothesis that macroscopic and microscopic objects are simply not governed by the same physical laws [2]. These original theories were challenged by the apparent universality of quantum theory, as well as the fact that certain unlikely superpositions can in fact be experimentally observed, albeit under highly controlled conditions [3].

In fact, effective superselection rules exist within standard Copenhagen quantum mechanics. For example, in the Feynman gedankenexperiment discussed above, it is the interaction with photons that destroys the electron interference pattern and leads to particle-like (non-interfering) behavior. This idea of interaction with an external environment leading to classical behavior has evolved into a formal theory of “Environmentally-Induced Superselection” (EIS), which offers a prescription for determining the superselection rules that are enforced by a particular environment.

More important than this prescription is the realization that all classical behavior arises from interactions with an uncontrolled environment. The decoherence of any quantum system can, in principle, be understood by correctly accounting for these system-environment interactions. Conversely, quantum mechanical features remain when a system is isolated from any external environment.

In many cases, decoherence can be related to a flow of quantum information from the system to the environment where it quickly becomes (for all practical purposes) inaccessible. In the case of the Feynman light microscope, for example, loss of visibility of the interference pattern occurs when the light wavelength is shorter than the separation between the two slits, allowing which-path information to be obtained from a single scattered photon. The direct connection between fringe visibility in an interferometer and the transmission of which-way information to the environment has been proven under very general conditions [37] and verified experimentally [33].

The general procedure for computing the time evolution of a quantum system coupled to an external environment involves first calculating the time evolution of the combined system+environment density matrix, then ignoring the environment by tracing over all environment degrees of freedom. If  $\rho = \rho_s \otimes \rho_e$  is the initial density matrix of system+environment (a direct product of the density matrices for system and environment alone), the total density matrix at any later time can be computed using the Heisenberg equation of motion:

$$i\hbar\dot{\rho} = -[\rho, H], \quad (3.1)$$

where  $H = H_s + H_e + H_{se}$  is the Hamiltonian for the system which can in general be divided into a sum of operators that act only on the system ( $H_s$ ), only on the environment ( $H_e$ ), and on both system and environment ( $H_{se}$ ). At any later time, the reduced density matrix,  $\rho_s$ , of the system alone can be calculated from  $\rho$  by a basis-independent trace over environment degrees of freedom:

$$\rho_s(t) = \text{Tr}_e \rho(t). \quad (3.2)$$

Environment	Master Equation
Scalar Field [119]	$\dot{\rho}_s = \frac{1}{i\hbar}[H_s, \rho_s] + \frac{\gamma}{i\hbar}[x, \{p, \rho_s\}] - \frac{2\gamma m \hbar(t, T)}{\hbar^2}[x, [x, \rho_s]] - \frac{4\gamma f(t, T)}{\hbar}[x, [p, \rho_s]]$
Thermal Bath of Oscillators [20]	$\dot{\rho}_s = \frac{1}{i\hbar}[H_s, \rho_s] + \frac{\gamma}{i\hbar}[x, \{p, \rho_s\}] - \frac{2\gamma m k_B T}{\hbar^2}[x, [x, \rho_s]]$
Monoenergetic Scatterers [58]	$\dot{\rho}_s = \frac{1}{i\hbar}[H_s, \rho_s] - \Gamma[x, [x, \rho_s]]$

Table 3.1: The master equations for a variety of decohering environments, with reference to the original derivation.

The trace is formally equivalent to measuring all of the environment degrees of freedom, then ignoring the results. Given this complete ignorance of the state of the environment, all remaining knowable information about the system is contained in  $\rho_s$ .

In many cases, a master-equation for  $\rho_s$  can be derived which contains terms accounting for the influence of the environment on the system, but which requires knowledge only of general characteristics of the environment (i.e. temperature) and does not explicitly include each environment degree of freedom. Several such master equations, for a variety of decohering environments, are presented in Table 3.1.

We will be particularly interested in the master equation describing an environment of monoenergetic scatterers, written here in the position basis and neglecting

	10 $\mu\text{m}$ Dust Particle	Bowling Ball
Lab Vacuum ( $10^{-11}$ torr)	$10^{23}$	$10^{31}$
300K Photons	$10^{19}$	$10^{27}$
Cosmic Microwave Background	$10^6$	$10^{17}$
Solar Neutrinos	$10^1$	$10^{13}$

Table 3.2: Localization Rates ( $\text{cm}^{-2}\text{s}^{-1}$ ). These order of magnitude estimates from Ref. [115] indicate the relative importance of various environments (including photons, gas particles, and neutrinos) for decoherence of two “macroscopic” objects: a 10  $\mu\text{m}$  diameter dust particle and a bowling ball. The localization rate,  $\Gamma$ , determines how quickly the spatial coherence of an object dissipates due to interaction with an external environment (see Eqn. 3.4).

internal dynamics of the system (i.e. assumed  $H_s = 0$ ):

$$\dot{\rho}_s(x, x') = -\Gamma(x - x')^2 \rho_s(x, x'). \quad (3.3)$$

We will return to the issue of non-negligible internal dynamics in Section 3.3.4 below.

The solution to Eqn. 3.3 is [4]:

$$\rho_s(x, x', t) = e^{-\Gamma^2 |x-x'|^2 t} \rho_s(x, x', 0). \quad (3.4)$$

where  $\Gamma(k_0)$  is determined by the energy and density of the scatterers as well as the scattering cross section. This solution represents exponential damping of off-diagonal terms in the system’s spatial density matrix. Because these terms represent the coherence between spatially separate components of the system’s wavefunction, coherence which disappears at a rate proportional to the square of the separation between components. All of the master equations listed in Table 3.1 with a term proportional to  $[x, [x, \rho_s]]$  are expected to exhibit this Gaussian behavior in some limit (i.e. in the high temperature limit for a thermal bath of oscillators). Theorists have warned, however, that this Gaussian behavior is not necessarily universal [7]. Already, counterexamples in which decoherence has a different spatial or time dependence have been predicted [42, 7] and, in one case, experimentally confirmed [26].

### 3.2.2 Previous Experiments

A variety of experiments have been performed which demonstrate the basic features of decoherence or study a specific decohering environment.

Our own group studied the transition from coherent diffraction to classical diffusion of atoms through standing wave light grating as the number of decohering, spontaneous photon scattering events was increased [46]. Pfau et. al. [89] measured the destruction of a two-slit diffraction pattern due to a single spontaneously scattered photon in a direct realization of the Feynman gedankenexperiment discussed above. Our group performed a study of the loss of coherence in an atom interferometer due to a single spontaneously scattered photon, and demonstrated that the coherence could be recovered if an appropriate measurement could be made of the scattered photon's final direction [25]. Clauser and Li [27] demonstrated that an atom interference pattern could be observed in a non-white fringe interferometer by using Doppler sensitive photon scattering to selectively decohere a single velocity class. More recently, Mei and Wietz [79] demonstrated that interfering contrast in a multiple-path Ramsey interferometer could actually be increased using spontaneous photon scattering to selectively decohere an out-of-phase path.

The general decoherence behavior predicted by Eqn. 3.4 arises and has been studied in the context of an atom interacting with a high-Q cavity [18], and trapped ions interacting with a fluctuating electric field [83]. Although not framed in the language of decoherence, interferometry experiments with neutrons interacting with a disordered solid explored decoherence phenomena a regime where the decoherence rate is independent of spatial separation [113]. A more recent experiment studied a similar long-range "saturation" of decoherence by introducing a disordered collection of microspheres into an optical interferometer [26].

Finally, the role played by decoherence in establishing quantum-classical correspondence has been studied in chaotic systems such as the delta-kicked rotor [43, 5].

### 3.3 Decoherence due to Photon Scattering in an Atom Interferometer

In this experiment, we studied the spatial decoherence caused by an environment of photons. The MIT atom interferometer was used to prepare atoms which are coherently separated into components up to 20  $\mu\text{m}$  apart, and also to monitor coherence via the interference fringe contrast. Atoms were subject to significant decoherence through the scattering of laser light whose mode and intensity are easily controlled. These features allowed us to quantitatively study decoherence as a function of the ‘size’ of an object as well as on the number of elementary scattering events. We observed a qualitative change in decoherence versus path separation as the number of photons increases, and verified quantitatively the decoherence rate constant in the many-photon limit. This experiment was the subject of a recent publication in Physical Review Letters [65], which is reproduced as Section B of this thesis. The discussion below will begin with a brief overview of the theory, experiment, and major results, then discuss experimental details not described in the published article.

#### 3.3.1 Photon Decoherence Theory

We begin by considering an atom whose transverse wavefunction is peaked at two positions which we may label  $x$  and  $x + d$ . If the atom spontaneously scatters a single photon, the atom and photon become entangled:

$$\begin{aligned} |\psi\rangle_i &= (|x\rangle + |x + d\rangle) \otimes |k_0\rangle \xrightarrow{\text{scat.}} \\ &|x\rangle \otimes |\phi_x\rangle + |x + d\rangle \otimes e^{ik_0d} |\phi_{x+d}\rangle, \end{aligned} \quad (3.5)$$

where  $|\phi_x\rangle$  is the wavefunction of a photon spontaneously emitted from position  $x$ ,  $|k_0\rangle$  is the initial (plane wave) state of the photon, and the factor  $e^{ik_0d}$  accounts for the difference in spatial phase of the initial photon between the two positions. We rewrite Eqn. 3.5 as a density matrix and, following the procedure outlined in Section 3.2.1, trace over the basis of scattered photon states to derive a reduced density matrix for

the atom alone:

$$\rho(x, x + d) \xrightarrow{\text{scat.}} \rho(x, x + d) \beta(d), \quad (3.6)$$

where  $\beta(d)$  is known as the decoherence function and has the properties  $|\beta(d)| \leq 1$  and  $\beta(0) = 1$ . The decoherence function is equal to the inner product of the two possible final photon states, which are identical apart from an overall translation:

$$\begin{aligned} \beta(d) &= e^{ik_0d} \langle \phi_x | \phi_{x+d} \rangle = e^{ik_0d} \langle \phi_x | e^{-i\hat{k}_x d} | \phi_x \rangle \\ &= \int d\Delta k P(\Delta k) e^{-i\Delta k d}, \end{aligned} \quad (3.7)$$

where the operator  $\hat{k}_x$  is the generator of photon translations along the  $\hat{x}$  axis. The resulting decoherence function is also equal to the Fourier transform of a probability distribution  $P(\Delta k)$ , with  $\Delta k$  representing the change in momentum of the photon along the  $\hat{x}$  axis.

A similar expression for  $\beta(d)$  is derived by Chapman [24] starting directly from the observation that when an atom within the interferometer scatters a photon into a particular final direction, the phase between the interfering paths is shifted:

$$\begin{aligned} |\psi\rangle_i &= (|x\rangle + |x + d\rangle) \otimes |k_0\rangle \xrightarrow{\text{scat.}} \\ &(|x\rangle + e^{i\Delta\phi}|x + d\rangle) \otimes |k_f\rangle. \end{aligned} \quad (3.8)$$

The magnitude of the phase shift is given by:

$$\phi = (\vec{k}_f - \vec{k}_0) \cdot \vec{d} = \Delta k d, \quad (3.9)$$

where  $\vec{k}_0$  is the initial momentum of the photon,  $\vec{k}_f$  is the final photon momentum and again  $\Delta k = (\vec{k}_f - \vec{k}_0)_x$ . Rewriting Eqn. 3.8 as a density matrix and, tracing over the allowed final momentum states of the photon we derive the same expressions as before for the reduced density matrix (see Eqns. 3.6-3.7).

When more than one photon is scattered, as long as successive scattering events are independent, the total decoherence function simply includes one factor of  $\beta$  for

each scattered photon:

$$\beta_{\text{total}}(d) = \sum_{n=0}^{\infty} P(n)\beta^n(d), \quad (3.10)$$

where  $P(n)$  refers to the probability that  $n$  photons were scattered. The distribution  $P(n)$  can be measured or calculated, though the number of photons scattered by a particular atom is intrinsically uncertain. The sum in Eqn. (3.10) is essentially a trace over this additional degree of freedom of the environment.

### 3.3.2 Apparatus and Procedures

The setup used to measure photon decoherence in an atom interferometer is shown in Figure 3-1. We added to the basic interferometer a region of resonant laser light ( $\lambda = 590$  nm) between the second and third gratings. As the atoms (which had been optically pumped into the  ${}^3S_{\frac{1}{2}}|F = 2, m_f = +2\rangle$  state) passed through the laser beam, they absorbed and spontaneously emitted (i.e. scatter) laser photons on the  ${}^3S_{\frac{1}{2}}|2, +2\rangle \rightarrow {}^3P_{\frac{3}{2}}|3, +3\rangle$  transition. The number of scattered photons was controlled via the intensity and mode of the laser light. The longitudinal position of the laser beam was adjusted to address a range of interfering path separations,  $d$ , between 0 and  $\approx 1.5\lambda$ .

Our experiments consisted of measuring the contrast reduction and phase shift of the atom interference fringes as a result of interaction with decohering light of a particular mode and intensity. We first measured the interfering contrast ( $C$ ) and phase ( $\phi$ ) with the atoms exposed to the laser light at some chosen path separation  $d$ . We will refer to this as the “decoherence-on” configuration below. We then measured the contrast ( $C'$ ) and phase ( $\phi'$ ) with the atoms exposed to the same laser light applied after the third grating (outside of the interferometer). We refer to this as the “decoherence-off” configuration. From these measurements we determined the magnitude of  $\beta$  as the ratio  $C/C'$ , and the phase of  $\beta$  as  $\phi - \phi'$ .

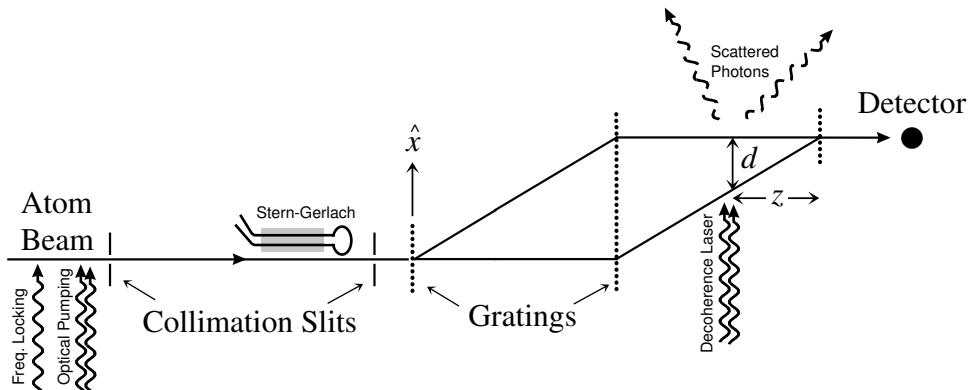


Figure 3-1: A schematic overview of the photon decoherence experiment. Before entering the atom interferometer, sodium atoms were optically pumped into the  ${}^3S_{\frac{1}{2}}|F = 2, m_f = +2\rangle$  state. The efficiency of optical pumping was monitored by measuring the deflection of the atomic beam in the gradient field produced using a two-wire Stern-Gerlach magnet. Within the interferometer, atoms continuously absorbed and spontaneously emitted photons from a variable intensity “decoherence” laser beam. Decoherence due to spontaneous emission results in reduced contrast interference fringes. The longitudinal position  $z$  of the laser beam could be continuously adjusted to address different atomic path separations  $d$ . The optical pumping and decoherence laser light was locked on resonance using the doppler technique described in Ref. [45].

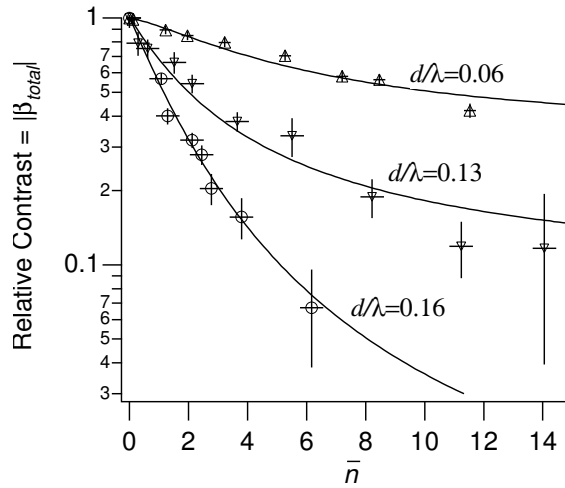


Figure 3-2: Loss of interfering contrast as a function of mean number of photons spontaneously scattered by atoms within the interferometer. Each curve represents a different path separation:  $d/\lambda = 0.06$  ( $\triangle$ ),  $0.13$  ( $\diamond$ ), and  $0.16$  ( $\circ$ ).

### 3.3.3 Results

A recently published paper describing our study of photon decoherence has been included as Appendix B. In this section, we simply highlight the main results.

Figure 3-2 demonstrates the approximately exponential reduction of spatial coherence as a function of the average number of scattered photons, while leaving the path separation fixed<sup>1</sup>.

Figure 3-3 shows the Gaussian reduction in contrast as a function of path separation for two different laser intensities.

Figure 3-4 shows measurements of the decoherence function for laser intensities corresponding to an average number of scattered photons,  $\bar{n}$ , ranging from  $\simeq 1$  to  $\simeq 8$ .

---

<sup>1</sup>The non-exponential asymptotic behavior at larger photon number is explained in detail in Appendix B

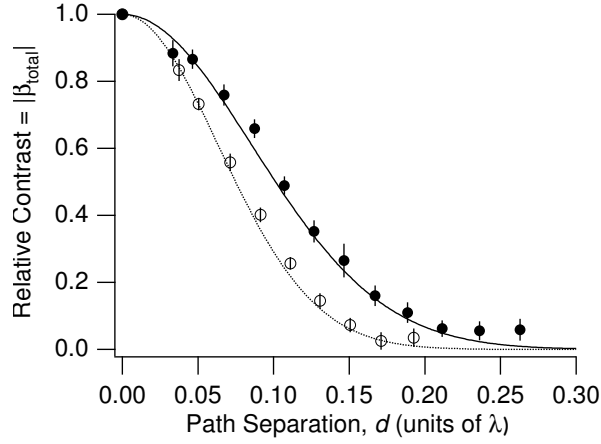


Figure 3-3: Loss of contrast in the many-photon regime. Overlaid are theory curves generated from Eqn. 9 of Appendix B using parameters (●)  $\bar{n} = 4.8 \pm 0.2$ ,  $\sigma_n = 1.8 \pm 0.1$  and (○)  $\bar{n} = 8.1 \pm 0.3$ ,  $\sigma_n = 3.5 \pm 0.1$ ) determined from independent beam deflection measurements.

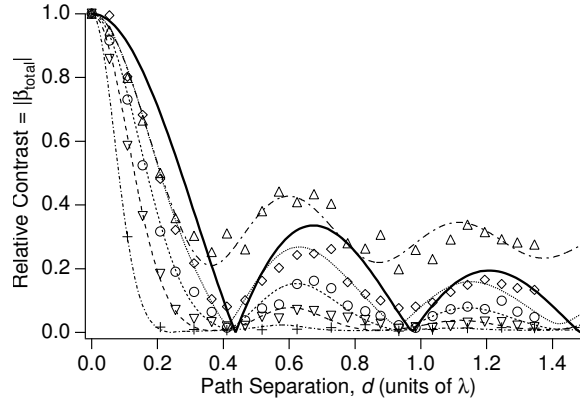


Figure 3-4: The total decoherence function,  $|\beta_{total}|$ , measured as the normalized contrast after spontaneous photon scattering. The solid line is the single-photon decoherence function. Also displayed are the best fits from which we determine  $\bar{n} = 0.9$  ( $\Delta$ ), 1.4 ( $\diamond$ ), 1.8 ( $\circ$ ), 2.6 ( $\nabla$ ), and 8.2 ( $+$ ).

### 3.3.4 Experimental Details

In addition to a working interferometer, this experiment required an optical pumping region for state preparation and a laser decoherence region. The laser source for both of these consisted of a Coherent 699 ring dye laser pumped by an Coherent Sabre Argon ion laser, the combination providing approximately 400 mW of single-mode light. The laser was locked to the sodium  ${}^3S_{1/2}|2, +2\rangle \rightarrow {}^3P_{3/2}|3, +3\rangle$  transition using the Doppler fluorescence technique described in Ref. [45]. The laser light passed through an electro-optic modulator to create sidebands at 1.713 GHz, then was coupled into 30 m of polarization preserving optical fiber for transport to the atom interferometer. A coupling efficiency of 30-40% was typical, providing more than enough light to meet the experimental requirements.

#### Optical Pumping

Approximately 20 mW of the laser light was used to optically pump the sodium atoms into their  ${}^3S_{1/2}|F = 2, m_f = +2\rangle$  ground state just prior to the first collimation slit. The optical pumping setup was essentially identical to the one described in Ref. [24], with the notable addition of an intensity stabilizer to compensate for observed long-term fluctuations in the laser intensity. These fluctuations were primarily due to instabilities in the dye jet of the Coherent 699, resulting from an underpowered dye pump. This could easily be fixed by installing a larger pump. Also, we noticed a long-term drift in the polarization of light output from the optical fiber. Because we used a polarizing beam cube to divide the laser light between optical pumping and decoherence regions, this polarization drift caused intensity drift in both regions.

The efficiency of the optical pumping scheme was studied using the strong gradient field of a 2-wire Stern-Gerlach magnet (described in Ref. [108]). By comparing the state sensitive deflection of the atomic beam in the Stern-Gerlach magnet, with we found that  $> 95\%$  of the atoms in the atomic beam were pumped into the correct state.

## Laser Decoherence Region

The decoherence environment consisted of photons from a laser beam directed along the  $\hat{x}$  axis which intersects both interfering paths (see Figure 3-1). The circularly polarized laser light is tuned to the same  ${}^3S_{\frac{1}{2}}|2, +2\rangle \rightarrow {}^3P_{\frac{3}{2}}|3, +3\rangle$  transition used for optical pumping. Because the atoms are dipole forbidden from decaying to any state other than  ${}^3S_{\frac{1}{2}}|2, +2\rangle$ , they can continuously scatter photons without falling out of resonance (the natural linewidth is  $\sim 200$  photon recoils wide).

The optical setup for the decoherence region is shown in Figure 3.3.4. An variable attenuator was used to control and stabilize the intensity of the laser light. Combined with an adjustable beam waist (described below), this allowed us to vary the average number of photons scattered per atom from  $< 1$  to  $\approx 12$ .

A telescope (composed of fixed lens L2 and translatable lens L3) was used to adjust the laser beam waist in the horizontal direction (along the atomic beam axis) between  $100 \mu\text{m}$  and  $1 \text{ mm}$ . Cylindrical lens L1, oriented horizontally, provided a laser waist of  $\approx 1 \text{ cm}$  in the vertical direction (perpendicular to the atomic beam), so that the entire  $1\text{mm}$  height of the atomic beam would be nearly uniformly illuminated.

In order to address path separations from  $0-1.5\lambda$  it was necessary to translate the laser beam longitudinally by  $\pm 15 \text{ mm}$ . This was accomplished by refracting the laser light through a pair  $1/2$  inch thick glass (BK7) windows ( $n = 1.509$ ) oriented at an angle to the incident laser beam (see Figure 3.3.4). When the optical flats are rotated, the laser beam is translated while remaining perpendicular to the atomic beam. This was important because if the angle had changed by as little as a few milliradians, the laser light would have been Doppler shifted out of resonance with the atoms. This system for translating the laser beam represents an improvement over the setup used in our group's previous photon scattering experiments [24].

The laser beam waist and intensity together determined the distribution  $P(n)$  of number of photons scattered per atom. For every laser waist setting used in the experiment, the average number of photons scattered per atom,  $\bar{n}$ , was determined as a function of laser intensity,  $I$ , by measuring the deflection of the atomic beam

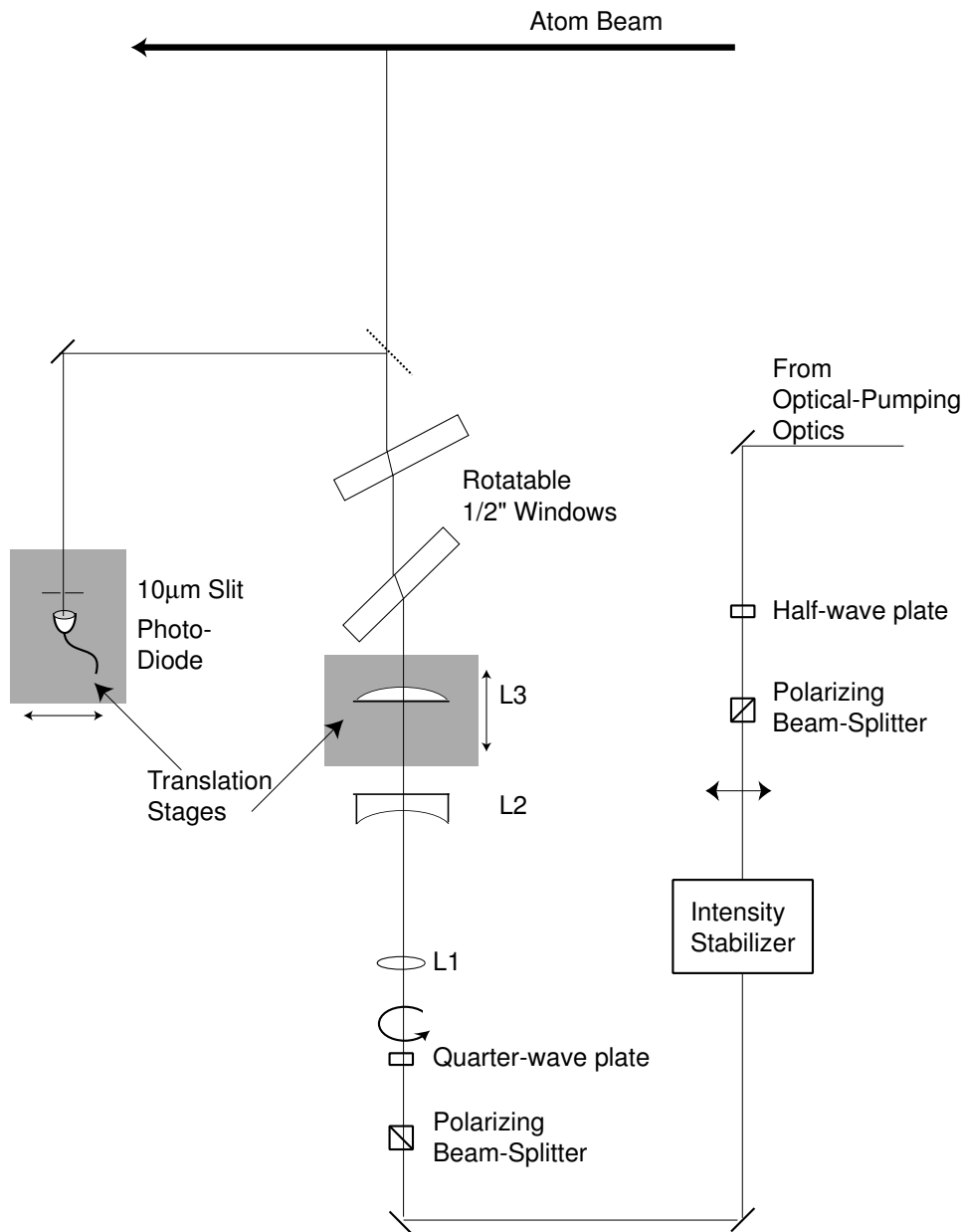


Figure 3-5: Optical system used to control the intensity, polarization, shape, and position of the decoherence laser light. The laser intensity was controlled using an Intensity stabilizer. The light was then circularly polarized to drive the sodium  ${}^3S_{1/2}|2, +2\rangle \rightarrow {}^3P_{3/2}|3, +3\rangle$  transition. Cylindrical lens L1 controlled the height of the laser beam, while the pair L2-L3 controlled its width along the atomic beam axis. A pair of rotatable, 1/2 inch thick glass windows were used to translate the laser beam longitudinally (and thereby address different path separations). For diagnostic purposes, a 10  $\mu\text{m}$  slit mounted in front of a photodiode on a translation stage could be used to measure the laser beam's horizontal profile.

with the laser on versus off (each scattered photon contributes, on average,  $1 \hbar k$  of transverse momentum to the atom).

We also measured, for each waist and laser intensity, the increase in width of the atomic beam with laser on versus off. From this measurement we extracted the rms spread,  $\kappa$ , in transverse momentum transferred to the atoms by the scattered photons. This spread includes a contribution both from the spread in number of scattered photons,  $\sigma_n$ , and the spread in transverse momentum,  $\sigma_k$ , accompanying a single spontaneous emission ( $\sigma_k = \frac{2}{5}k_0$  for the circularly polarized light used in this experiment). The value of  $\sigma_n$  accounts both for the intrinsic randomness of the spontaneous emission process, as well as the different amount of time that atoms of different velocities spend traveling through the laser beam. In Figure 3.3.4, measurements of the total momentum spread, given by:

$$\kappa = \sqrt{\bar{n}\sigma_k^2 + \sigma_n^2 k_0^2}, \quad (3.11)$$

are plotted as a function of the average number of scattered photons, for a laser waist of 350  $\mu\text{m}$ .

The results of our measurements of  $\bar{n}$  and  $\kappa$  were used to make the theoretical predictions with which our data are compared.

### Zero Phase Drift

For any given set of data, we would ideally find that all of the interference fringe patterns measured in the decoherence-off configuration have the same phase. However, it is generally the case that these measurements of this decoherence-off or “zero-phase” drift at a rate of up to a few radians per hour. One source of this drift is thermally induced changes in the relative position of the atom gratings versus the optical gratings used to determine their position. Another possibility is that imperfect alignment coupled with pointing instability causes the phase of the optical interferometer to drift in time.

Figure 3-7 shows a typical series of zero-phase measurements taken over the course

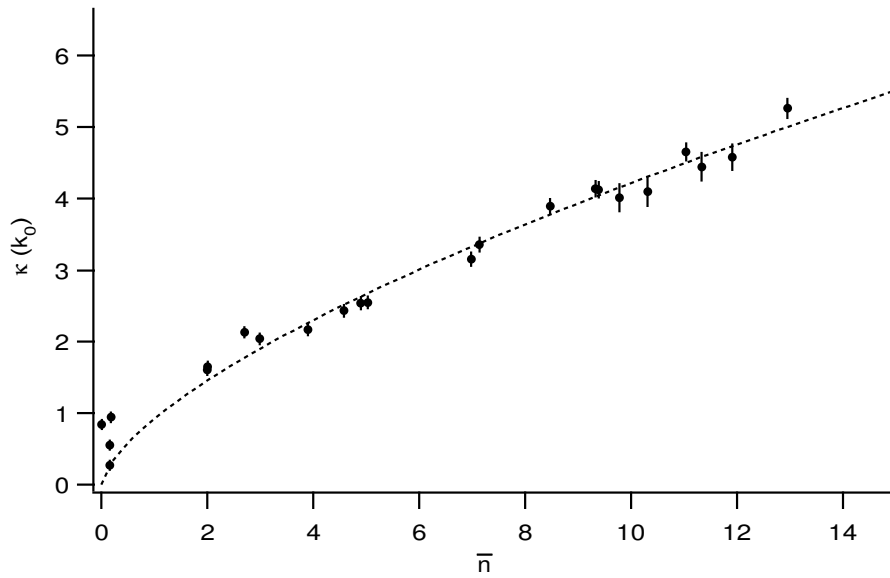


Figure 3-6: Spread in momentum,  $\kappa$ , transferred to atoms as they pass through the decoherence laser region, in units of the photon wavevector  $k_0$ . The momentum spread is plotted versus the average number,  $\bar{n}$ , of photons scattered. For these measurements, the decoherence laser waist (along the atom beamline) was  $350 \pm 5 \mu\text{m}$ , and the atom beam velocity was  $\approx 3110 \pm 10 \text{ m/s}$ .

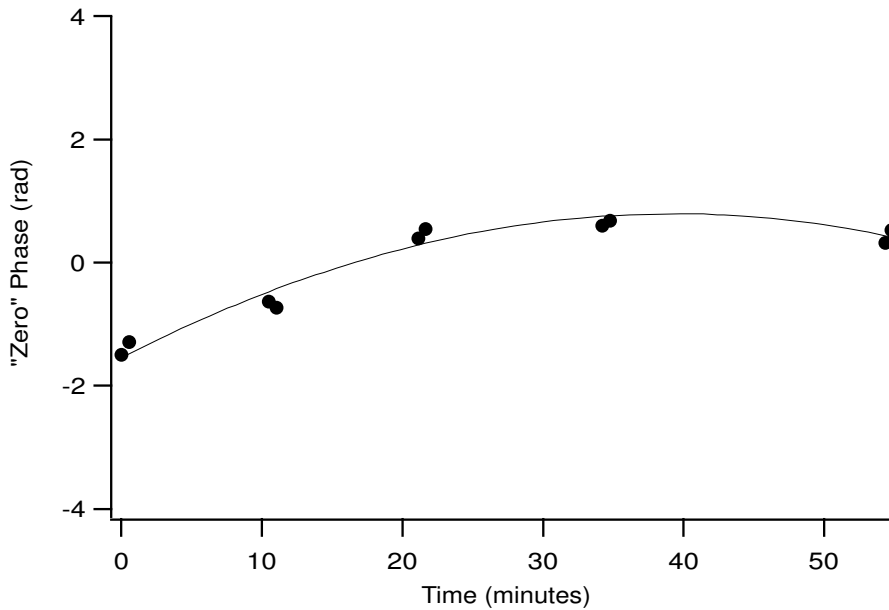


Figure 3-7: Plot of the interfering phase measured in the “decoherence-off” configuration (i.e. the “zero-phase”) as a function of time. Statistical error bars are too small to be visible. Phase drift rates of 1-2 mrad/hour are typical, and much reduced compared to experiments performed before the implementation of the new interferometer platform.

of an hour. Also shown is a polynomial fit to the phase data, which is our best prediction for how the true zero-phase varied as a function of time during this particular data set. The decoherence-on phase measurements for this data set were interspersed between the zero-phase measurements. We determined the phase of the decoherence function by subtracting the interpolated zero-phase from the measured decoherence-on phase.

### Spread in $d$

In our analysis, we have assumed that the separation between the two interfering paths at the point of light scattering is fixed, and is exactly the same for every atom in the beam. This assumption neglects the fact that the atom paths are converging as they approach the third grating, so that the path separation is not constant as the atoms pass through the finite-width laser beam. Taking the path separation to

be constant is equivalent to neglecting  $H_s$  in the master equation for monoenergetic scatters (see Table 3.1). Furthermore, because the atom diffraction angle is velocity dependent, atoms of different velocities have different path separations at the point of intersection with the decoherence light.

We can account for both of these effects by replacing Eqn. 3.10 for the total decoherence function, with the following expression:

$$\beta_{\text{total}}(d_1, d_2, \dots, d_n) = \sum_{n=0}^{\infty} P(n) \beta(d_1) \beta(d_2) \dots \beta(d_n), \quad (3.12)$$

where  $\beta$  is the single-photon decoherence function. Unfortunately, while we could determine the average atom path separation at the center of the laser beam simply by measuring the distance between the laser beam and the third grating, we had no way of determining the individual  $d_i$ . It was therefore impossible to use Eqn. 3.12 to make quantitative theoretical predictions to compare against our experimental results.

We can however derive an approximate expression for  $\beta_{\text{total}}$  by setting  $d_i = \bar{d} + \Delta d_i$ , and expanding Eqn. 3.12 with the  $\Delta d_i$  as small parameters:

$$\beta_{\text{total}}(\bar{d}) = \sum_{n=0}^{\infty} P(n) \beta^n(\bar{d}) + O\left(\left(\frac{\Delta d_i}{\bar{d}}\right)^2\right), \quad (3.13)$$

where  $\bar{d}$  is defined as the average path separation for all scattered photons (i.e.  $\bar{d} = \sum_i d_i / n$ ). For our experimental parameters,  $\Delta d_i \ll \bar{d}$ , and Eqn. 3.13 gives a value for  $\beta_{\text{total}}$  within a 1 – 2% of Eqn. 3.12.

To make theoretical predictions using Eqn. 3.13 for comparison with our measurements, we needed to know the value of  $\bar{d}$ . We chose to extract  $\bar{d}$  from the phase of the decoherence function itself. In the many-photon limit, this phase is equal to  $\arg(\beta_{\text{total}}) = \bar{n} \bar{d} k_0$  (see Eqn. 9 of Appendix B). To obtain  $\bar{d}$  we first determined  $\bar{n}$  from independent atom beam deflection measurements, then calculated  $\bar{d} = \frac{\arg(\beta_{\text{total}})}{\bar{n} k_0}$ .

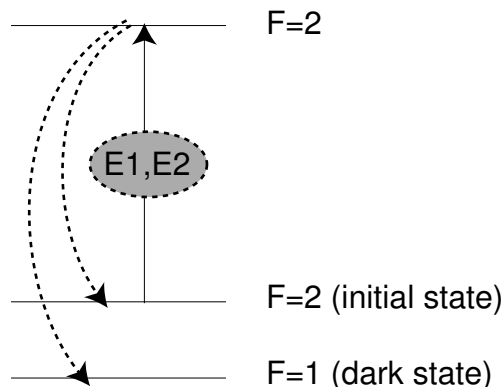


Figure 3-8: In the experiment to study decoherence from two successive environments, atoms are prepared in the  ${}^3S_{\frac{1}{2}}|F = 2, m_f = 2\rangle$  ground state as before. However the decohering light is no longer tuned to a cycling transition, but rather is applied between the  ${}^3S_{\frac{1}{2}}|F = 2\rangle - {}^3P_{\frac{3}{2}}|F = 2\rangle$  manifolds. With each photon scattered, therefore, the atom has a chance to fall into the “dark” ground manifold  ${}^3S_{\frac{1}{2}}|F = 1\rangle$ .

### 3.4 Decoherence from Two Successive Environments

In this experiment we measured the decoherence caused by two successive photon decoherence environments. The experiment illustrates the concept of environmentally-induced superselection (EIS), and demonstrates that an atom’s spatial coherence may be maintained even when it changes internal state within the interferometer.

The “superselected” states of a system are defined as those states towards which the system evolves under the influence of a given environment, typically the stationary solutions ( $\dot{\rho}_s \rightarrow 0$ ) of the relevant master equation<sup>2</sup>. For the master equation describing many-photon decoherence (Eqn. 3.3),  $\dot{\rho}_s \rightarrow 0$  when either  $\rho_s(x, x') \propto \delta(x - x')$  or  $\Gamma \rightarrow 0$ . We can arrange  $\Gamma = 0$  by exploiting the fact that different internal states of the atom interact differently with the environment (i.e. the light field).

Consider a sodium atom optically pumped into the  ${}^3S_{\frac{1}{2}}|F = 2, m_f = 2\rangle$  state. If the atom is subject to decohering light resonant with its  ${}^3S_{\frac{1}{2}}|F = 2\rangle - {}^3P_{\frac{3}{2}}|F = 2\rangle$

<sup>2</sup>When no such stationary solutions exist, a set of approximate classical states may be identified as those which minimize the entanglement between system and environment [134].

transition<sup>3</sup>, it will eventually be optically pumped into the  ${}^3S_{\frac{1}{2}}|F = 1\rangle$  state (see Figure 3-8). Because the light field does not interact strongly with atoms in the  ${}^3S_{\frac{1}{2}}|F = 1\rangle$  state,  $\Gamma = 0$  for these atoms. Any spatial coherence remaining when the atom arrives in the  ${}^3S_{\frac{1}{2}}|F = 1\rangle$  state is immune from further decoherence.

To demonstrate this, we implemented a pair of decohering environments E1, E2 within the interferometer (see Figure 3-9). The intensity of the light in environment E1 was sufficient to scatter  $\approx 3$  photons from every atom. Because E1 was located just behind the first grating where  $d \ll \lambda$ , this environment caused no significant spatial decoherence (the contrast in Figure 3-9b is essentially equal to that in Figure 3-9a). Roughly the same intensity light was used in environment E2, located between the second and third gratings, but because  $d \gg \lambda$  for this region, a single scattered photon caused essentially complete spatial decoherence (Figure 3-9c).

When the atom is exposed to both decohering environments, spatial coherence is regained (Figure 3-9d). The reason is that within E1, the atom has been optically pumped into the  $F=1$  manifold so that  $\Gamma = 0$  and therefore  $\dot{\rho}_s = 0$  in E2. The change in internal state of the atom has no effect on the interference pattern because the internal state provides no which-path information. The spatial superposition state of the atom upon reaching E2 is already one of that environment’s “superselected” states, and does not further decohere. Although atoms exist in a non-classical superposition state throughout the experiment, because this superposition is not decohered by either environment E1 or E2, we refer to the atoms as being in a “decoherence-free subspace” (DFS) of the available quantum states [86, 30, 130, 74, 129, 9]. More complicated DFS’s have been studied in entangled multi-particle systems [70].

### 3.5 Decoherence due to Background Gas Scattering

In this experiment, we measured the spatial decoherence caused by increasing the ambient pressure within the interference chamber, increasing the collision rate between

---

<sup>3</sup>The  $m_f$  quantum number is unimportant for a basic understanding of the experiment

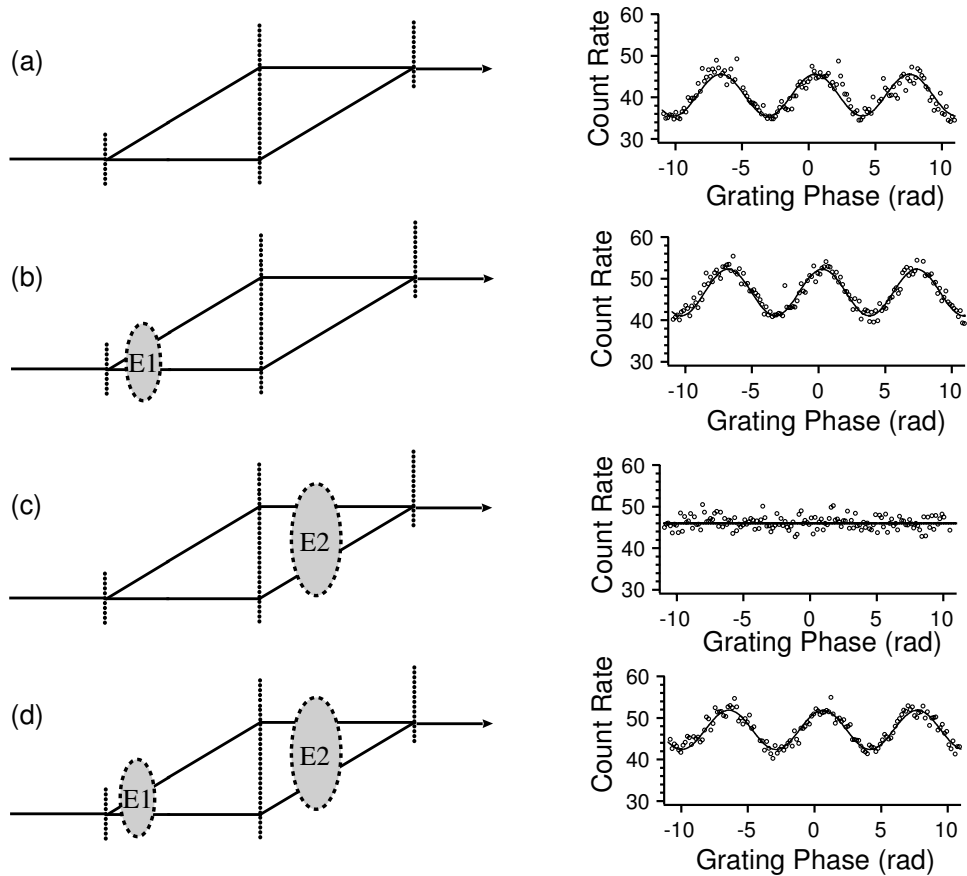


Figure 3-9: Decoherence due to two successive photon environments (E1 and E2). (a) With the light turned off in both E1 and E2, interference fringes are observed. (b) Environment E1 alone causes little spatial decoherence. (c) Environment E2 alone causes nearly complete spatial decoherence. (d) Because, in E1, atoms are optically pumped into a classical (dark) state, they are no longer subject to spatial decoherence in E2.

interfering atoms and background gas particles. We demonstrated that decoherence is not always proportional to the number of scattering events.

Referring to Table 3.2, we see that scattering of background gas particles can be a much more significant source of decoherence for macroscopic objects than photon scattering — even at ambient pressures of  $10^{-11}$  Torr. The localization rates in the table were calculated using the formula:

$$\Gamma = k^2 \sigma n \quad (3.14)$$

where  $k = 2\pi/\lambda$  is the wavevector and  $n$  the flux of scattering particles and  $\sigma$  is the cross section of the macroscopic object for the scattering particles. Although the flux of room-temperature blackbody photons is six orders of magnitude larger than that of gas particles at  $10^{-11}$  Torr, the deBroglie wavelength (which sets the scale for how effectively an environment particle can “measure” the position of the quantum system) of massive particles at room temperature is roughly five orders of magnitude smaller than the photon wavelength.

We studied spatial decoherence due to gas scattering by measuring the contrast of our atom interference signal as a function of background gas pressure. Using a controlled leak, we varied the pressure in our main region between  $2 * 10^{-7}$  and  $2 * 10^{-6}$  Torr, corresponding to a range of mean free paths for atom in the beam between roughly 1 m and 10 cm. The results of this experiment, both contrast and mean atom flux as a function of pressure, are displayed in Figure 3-10.

We can see the effect of background gas scattering in the reduction of atomic flux: atoms are lost from the atomic beam at high main chamber pressures. However, no statistically significant contrast reduction is apparent.

The explanation is that, after scattering from a background gas particle, the vast majority of sodium atoms end up with enough change in momentum that they no longer reach our hot wire detector. In other words, the cross section for scattering

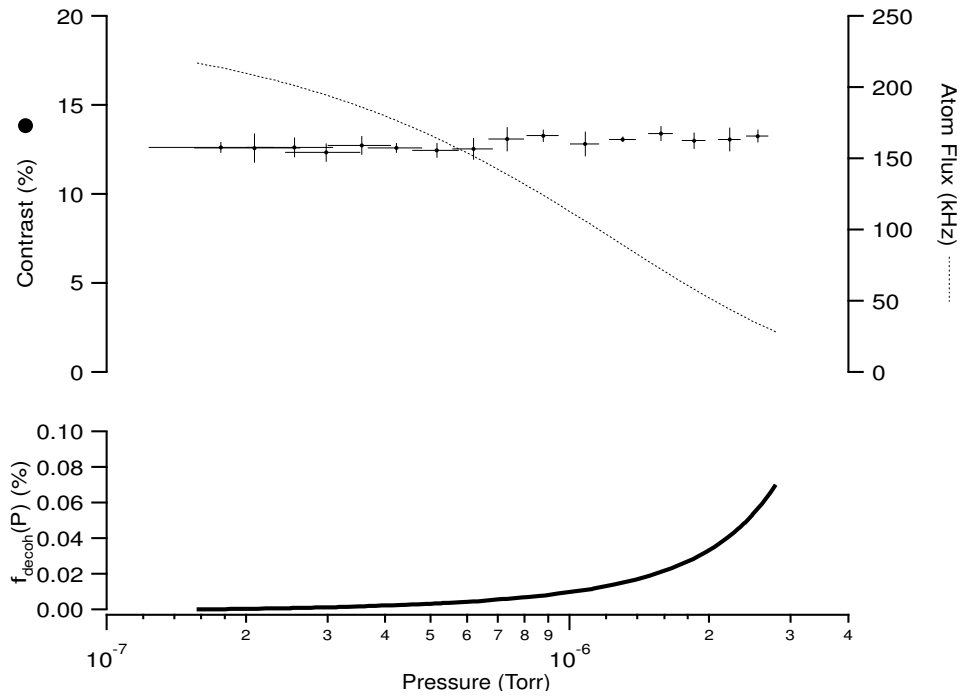


Figure 3-10: Interfering contrast and mean atom count rate plotted as a function of the pressure in the main vacuum chamber. Despite the decohering effect of the scattering from background gas particles, contrast remains constant as the pressure increases by an order of magnitude, because our hot-wire selectively detects those atoms which have not scattered. The fraction of atoms reaching the detector which *have* scattered, plotted in the lower half of the figure, is less than 0.1% over the entire pressure range studied.

into the solid angle,  $\Delta\Omega$ , subtended by the hot-wire detector:

$$\sigma_{det} = \int_{\Delta\Omega} \frac{d\sigma}{d\Omega} d\Omega, \quad (3.15)$$

is much smaller than the total scattering cross section  $\sigma_{tot}$ . To quantify this claim, we computed the ratio  $\sigma_{det}/\sigma_{tot}$  using a simple hard sphere (radius = 4Å) model for the sodium-background gas potential. For the conditions under which the data in Figure 3-10 were taken, ( $v = 3000$  m/s and a 1 mm tall by 50  $\mu\text{m}$  wide detector wire), we find  $\sigma_{det}/\sigma_{tot} \approx 10^{-4}$ .

The number of atoms which reach the detector after scattering is given by:

$$FN\sigma_{det}, \quad (3.16)$$

where  $F$  is the atom beam flux,  $N$  is the number of scatterers, and  $\sigma_{det}$  is the cross section for scattering into the solid angle subtended by the detector. Similarly, the number of atoms which reach the detector without having scattered is given by:

$$F(A - N\sigma_{tot}), \quad (3.17)$$

where  $A$  is the area of the atomic beam and  $\sigma_{tot}$  is the total scattering cross section. Those atoms which have not scattered are not subject to decoherence.

Using Eqns. 3.16 and 3.17, we calculate as a function of background gas pressure the fraction of atoms reaching the detector which *have* scattered and *are* therefore subject to decoherence as:

$$f_{decoh}(P) = \frac{F\sigma_{det}}{F A - F\sigma_{tot} + F\sigma_{det}} = \frac{1}{\frac{\sigma_{tot}}{\sigma_{det}} - 1} \frac{I(P=0) - I(P)}{I(P)}, \quad (3.18)$$

where  $I(P)$  is the count rate as a function of background gas pressure. This fraction, plotted in the lower half of Figure 3-10, grows with pressure, but remains less than 0.1% for the entire range of pressures we studied. Thus, our claim that most of the atoms reaching the detector are not subject to decoherence, is justified. Our current

apparatus does not have sufficient signal-to-noise to study higher background gas pressures for which  $f_{decoh}$  may become significant.

## 3.6 Decoherence versus Dephasing

### 3.6.1 Introduction

Despite decades of work and hundreds of papers published on the subject, there currently exists no single, well-accepted definition of decoherence. In some sense, no such definition is necessary. What is more important is that the physical model describing how a given system's density matrix evolves appropriately includes any influence of its environment. However, to the extent that any of broad class of different "environments" similarly influence a variety of different quantum systems, it is useful to group them together under the single label "decoherence."

The atom-photon scattering which leads to loss of contrast in our atom interferometer is one member of this class of "decoherence" processes. The essential feature of this process is the entanglement between the atom's position and the quantum state of the scattered photon. This entanglement is what makes "which-path" information available in the environment, and is the starting point for explaining the loss of interfering contrast.

There exist another set of "dephasing" processes which also reduce interfering contrast, but which do not involve entanglement, and therefore differ fundamentally from atom-photon decoherence. To make this often subtle distinction between dephasing and decoherence more clear, we have performed an experiment which is formally nearly identical to the photon decoherence experiment, but which would generally be considered an example of inhomogeneous broadening. Inhomogeneous broadening occurs when different members of an ensemble have a different value of some classical parameter (e.g. position, velocity) that influences their phase. This leads to what we will call "classical dephasing."

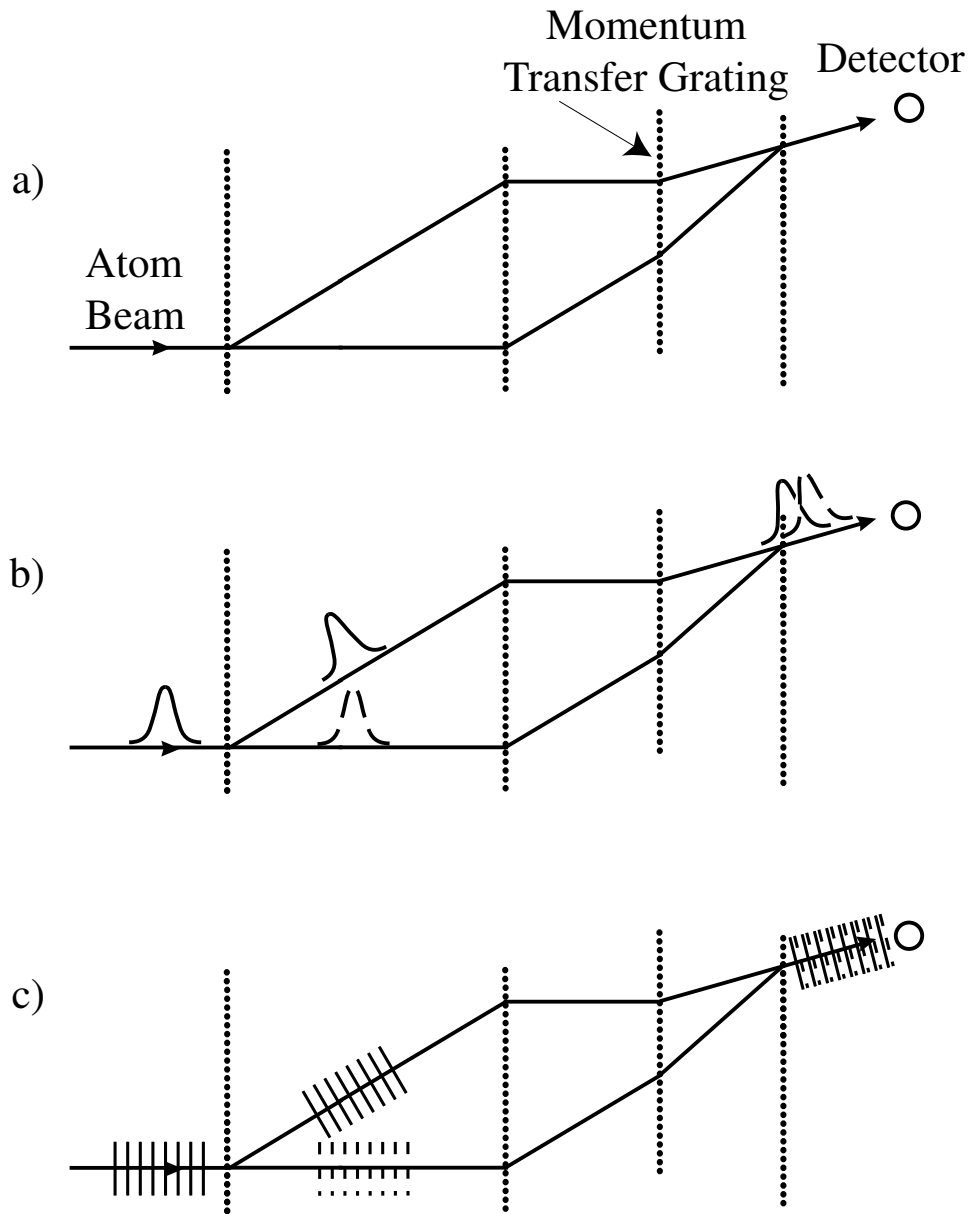


Figure 3-11: Schematic of an experiment to demonstrate the distinction between dephasing and decoherence. A fourth diffraction grating is introduced (a) into the Mach-Zehnder interferometer, causing a length difference between the interfering arms. A resulting loss of contrast can be explained as arising from different times of arrival (b) for atomic wavepackets traversing each path, or simply as a sum over the out-of-phase interference patterns (c) formed by each velocity component of the atom beam.

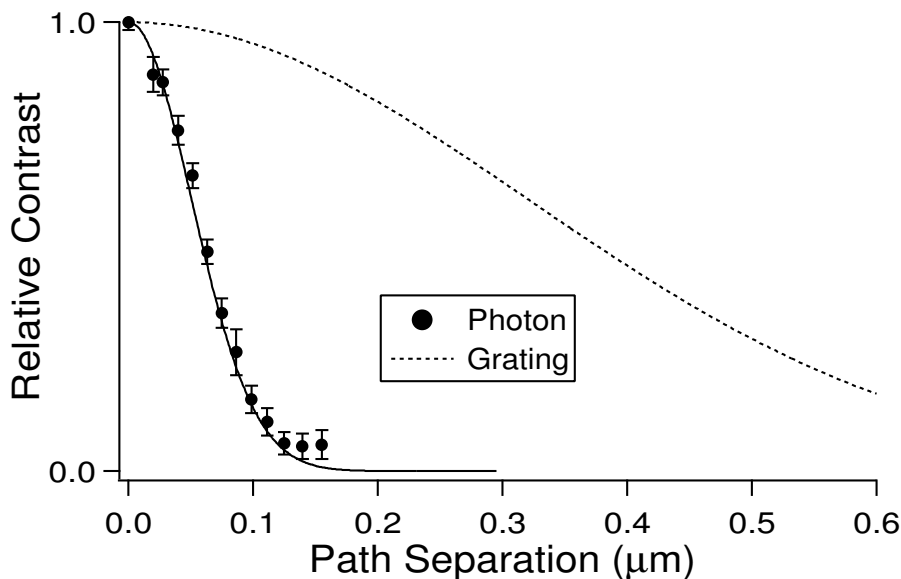


Figure 3-12: A comparison of the contrast loss versus path separation due to multiple-photon scattering (from Figure 3-3) and the addition of a fourth diffraction grating. In both cases, the contrast decreases exponentially with path separation squared.

### 3.6.2 Fourth-Grating (Dephasing) Experiment

The experiment (see Figure 3-11) consisted of introducing a fourth grating into the second half of the interferometer, then selectively measuring the interference pattern produced by those atoms which are first order diffracted at the fourth grating.<sup>4</sup> The contrast of this pattern, measured as a function of the longitudinal position of the fourth grating, is displayed in Figure 3-12. The results show a Gaussian reduction in contrast as a function of path separation at the point of diffraction — identical in form to the contrast loss observed in the multiple-photon decoherence experiment.

### 3.6.3 The “Decohering Environment”

To make as close an analogy as possible to the photon experiment, we first consider what might act as the decohering environment in the fourth-grating experiment. The first order diffraction of an atom by the fourth grating is formally equivalent to photon

<sup>4</sup>Further details of this experiment will be included in the forthcoming thesis of Tony Roberts.

scattering, and results in a phase shift between interfering arms analogous to Eqn. 3.9:

$$\Delta\phi(v) = k'_g d(v). \quad (3.19)$$

The only difference from the photon case is that here the momentum transferred to the atom is fixed by the period of the grating  $k'_g = 2\pi/\lambda'_g$ . (Here, the primes indicate that the period of the momentum transfer grating may be different from that of the three gratings forming the interferometer.)

We note that the diffraction angle,  $\theta_D = \lambda_{dB}/\lambda_g$  and therefore the path separation,  $d$ , are a function both of the interferometer grating period and the atom's deBroglie wavelength. The symmetric Mach-Zehnder geometry ensures that  $d = 0$ , independent of velocity, at the position of the third grating. But at the position  $z$  of the fourth grating, the path separation is velocity dependent:

$$d(v) = \frac{\lambda_{dB}}{\lambda_g} z = \frac{h}{\lambda_g m v} z. \quad (3.20)$$

Because diffraction at the fourth grating causes a velocity dependent phase shift via the velocity dependent path separation, when we average over the velocity distribution of the beam, the contrast of the resulting interference pattern is reduced. This should be compared to Eqn. 3.9 where a phase difference between paths is associated with each possible direction of a scattered photon. It was the average over this unobserved photon degree of freedom that caused a reduction in contrast. In the same way, averaging over the longitudinal velocity distribution of our atomic beam,  $P(v)$ , causes a reduction in contrast:

$$C = C_0 \int dv P(v) e^{i\Delta\phi(v)}, \quad (3.21)$$

Note the similarity between this expression and Eqn. 3.7 for contrast loss in the photon case: longitudinal velocity  $v$  is analogous to the change in photon momentum  $\Delta k$ , and formally plays the role of an ignored environment degree of freedom since our detector is not sensitive to longitudinal velocity.

### 3.6.4 Comparison with Photon Decoherence

In the photon case, we were able to derive contrast loss from two perspectives: which-path and phase-diffusion. Equation 3.21 suggests that we might equivalently consider the loss of contrast in the fourth-grating experiment to be a form of phase diffusion. However, in the photon case, a scattered photon is in a coherent superposition of all of its possible final momentum states, whereas the longitudinal quantum state of the atom beam is totally incoherent [99]. In the fourth grating experiment, it is therefore appropriate to think of each atom as having a particular, well defined longitudinal velocity. Thus, the average over longitudinal velocity is really an average over different atoms. This differs from the average over photon momentum in the photon decoherence experiment, which can be considered an average over a single photon's coherent momentum components. Thus, although the expressions we have derived for contrast loss are similar in the photon decoherence (Eqn. 3.7) and fourth-grating (Eqn. 3.21) experiments, the physical origin is somewhat different in the two cases.

We now explore whether the fourth-grating experiment can be explained in terms of the which path point of view (see Figure 3-11b). When the fourth grating is in place, the two paths of the interferometer are of different lengths. Thus it is possible, in principle, to determine which path the atom takes by measuring the time of flight between the paths' mutual starting and ending points. However, in order to measure the time of flight, it would be necessary to prepare each atom at a known position, time, and mean velocity prior to entering the interferometer. The preparation procedure modifies the atoms' longitudinal density matrix, introducing off-diagonal elements [90], and thus is not perfectly analogous to the experiment actually performed.

In attempting to explain the loss of contrast in the fourth-grating experiment both from phase-diffusion and which-path points of view, we have identified fundamental differences between the fourth-grating and photon-decoherence experiments. These differences suggest the possibility that the fourth grating experiment is an example

of classical dephasing and does not represent “decoherence” in the same sense as the photon experiment.

### 3.6.5 Distinguishing between Decoherence and Dephasing

Wojciech Zurek has proposed [133] an informal test to distinguish between dephasing and decoherence. His argument is based on decoherence experiments in which it is theoretically possible to recover lost coherence by measuring the state of the decohering environment (i.e. the momentum of the scattered photons in our photon decoherence experiments). He claims that in a true decoherence experiment, in order to recover coherence it will be necessary to know (either by measurement or explicit state preparation) the quantum state of the environment both before and after the environment-system interaction has occurred. If a single measurement of the environment, either before *or* after the system-environment interaction, is sufficient for full contrast recovery, then the experiment represents nothing more than classical dephasing.

Applying this test, the fourth-grating experiment falls clearly into the category of classical dephasing. If the longitudinal velocity of an atom is measured, either before or after the atom passes through the interferometer, then the phase shift of that atom’s interference fringes (Eqn. 3.19) is completely determined. The loss of contrast evident in Figure 3-12 can be completely recovered by binning the detected atoms according to their measured longitudinal velocity to build up a separate interference pattern for each velocity class, then shifting the phase of each pattern by the amount calculated from Eqn. 3.19. When the fringe patterns from separate velocity classes are now combined, they will all be in phase, and would show no evidence of contrast loss. Since only one measurement is required, the grating experiment fails Zurek’s test for true decoherence.

In the photon decoherence experiment, lost contrast can be recovered if the final (momentum) state of any scattered photons is measured. Just as in the grating case, the atoms can be binned according to the measurement results, and the fringe pattern in each bin can be adjusted in phase by an amount  $\Delta\phi = \Delta Kd$ , where

$\Delta K = k_{final} - k_{initial}$ . But this phase correction depends on both the initial and final momentum state of the photon. In our case, the initial state was not measured, but rather each photon was prepared in the same momentum state  $|k_0\rangle$  by the laser. Because knowledge of both the initial and final state was necessary to determine  $\Delta\phi$ , the photon experiment satisfies Zurek’s decoherence test.

We can design a nearly identical photon experiment which again fails Zurek’s test (see Figure 3-13). In this thought experiment, we excite the atom before it enters the interferometer. This amounts simply to changing the atom’s internal state, and thus has no effect on the interfering contrast. We can arrange for the atom to spontaneously decay within the interferometer with near certainty by making the interferometer long enough. This spontaneous emission process imparts a random phase between the two atom paths  $\Delta\phi = k_{final} d$ , and if the path separation is sufficiently large, no interference pattern will be observed. There will be a loss of contrast that results from the average over the final photon momentum alone (i.e. replacing  $P(\Delta K)$  with  $P(k_{final})$  in Eqn. 3.7).<sup>5</sup>

A single measurement (for each atom) of the direction of the emitted photon can be used to determine  $\Delta\phi$ , and thereby recover lost contrast as in Ref. [25]. Because full contrast can be recovered with only a single measurement this experiment would not qualify as an example of decoherence according to Zurek’s definition.

I propose modifying Zurek’s test and suggest that, if lost contrast can be recovered by measuring the quantum state of the environment before the system-environment interaction has occurred, then the interaction does not represent decoherence, but rather classical dephasing. This definition excludes the grating experiment, but includes both incarnations of the photon decoherence experiment, as intuition dictates. The definition specifies only “measurement” not “measurement and preparation” of the environment, because it is often possible to prepare an environment that causes no decoherence (i.e. detuning the laser light in the photon decoherence experiment so

---

<sup>5</sup>For simplicity, we imagine that the path separation in this hypothetical experiment is constant, so that the phase shift after scattering  $\Delta\phi = k_{final} d$  is independent of where, within the interferometer, the spontaneous emission occurs.

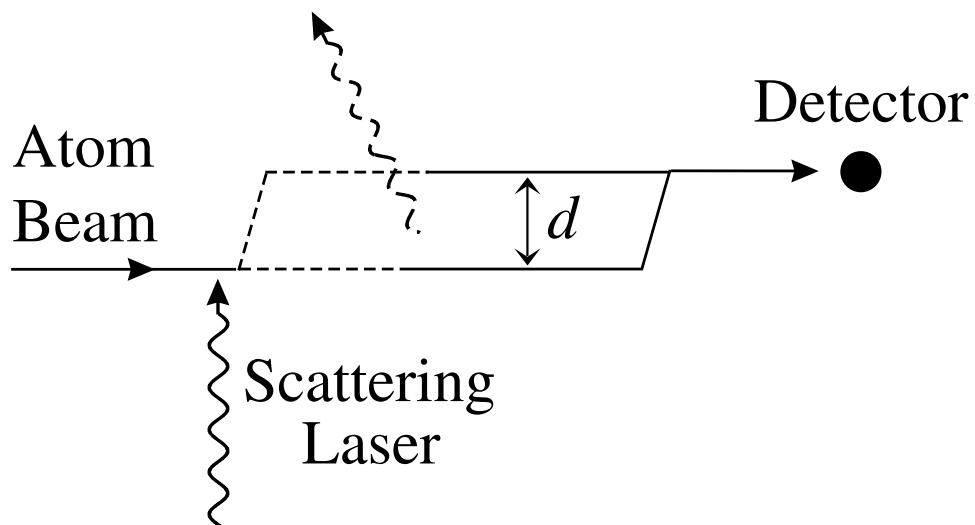


Figure 3-13: Schematic of a thought experiment in which contrast lost due to photon scattering can be recovered in a single measurement. Atoms are excited before entering an interferometer with path separation  $d$ , and spontaneously decay within the interferometer. Because photon absorption occurs outside the interferometer, the initial photon momentum state is essentially irrelevant to the experiment.

that no photons are scattered). Note that this definition also excludes some published experiments which claim to study decoherence. For example, in the paper of Myatt et. al. [83], decoherence is caused by a random voltage applied to the electrodes of an ion trap. Though impractical, full contrast could in principle have been recovered in their experiment by measuring this random voltage before it is applied to the ions, then correcting the measured interference signal according to the applied voltage.

The physics of contrast loss in the fourth-grating experiment is obviously straightforward. However, the ambiguity that arises when casting this experiment into the language of decoherence suggest the need for clarification of the distinction between decoherence and classical dephasing. Zurek's heuristic test and my proposed modification represent only a beginning. Future work will hopefully achieve a rigorous and precise definition of "decoherence," sharpening our understanding of this phenomenon.

# Chapter 4

## Measuring the Matter-Wave Index of Refraction with an Atom Interferometer

### 4.1 Introduction

This chapter presents preliminary results of an experiment to measure the index of refraction of an argon gas for sodium matter waves (“sodium-argon index”). In analogy to classical optics, the index of refraction is a measure of the phase shift and attenuation of an incident matter wave as it propagates through a target medium.

#### 4.1.1 Motivation

Measurements of the matter-wave index of refraction can yield detailed information about the atom-atom interaction potential,  $V(r)$ . Ab initio calculations of these potentials are prohibitively complex for all but the simplest of atomic systems. Where simpler theoretical models exist, they contain free parameters which can only be determined experimentally. Until more experimental data becomes available, it is impossible to determine which models provide the best approximation of the true potentials. Compared to the several types of experiments (see Section 4.2.1) from

which information about the interatomic potential has been obtained, measurements of the matter-wave index of refraction are distinguished by their sensitivity to the long-range form of  $V(r)$  [39].

Studies of the matter-wave index of refraction also promise to reveal atom optical analogies to well-known optical phenomena. Originally discovered as an optical phenomenon, “glory scattering” is known to be a feature of atom optics as well. In atom-atom collisions it manifests as “glory oscillations” in the magnitude and phase of the forward scattering amplitude as a function of collision energy. Previous atom-atom scattering experiments have explored glory oscillations in the total scattering cross section [120], but no experiment has yet been sensitive to glory oscillations in phase. A previous attempt by our group [54] to observe glory oscillations in phase and amplitude was inconclusive, but suggested that the phenomenon would become apparent if statistical error bars were reduced and systematic effects addressed.

### **4.1.2 Chapter Outline**

Section 4.2 of this chapter reviews previous theoretical and experimental studies of the sodium-argon interaction potential. A technique for measuring the matter-wave index of refraction using an atom interferometer is then presented, along with previous sodium-argon index measurements. Apparatus and analysis refinements are next discussed which have lead to significantly reduced statistical error compared with previous experiments (Section 4.3). Next (Section 4.4), a study is made of possible systematic errors and methods developed to minimize them. Finally, implications and prospects for future work are discussed (Section 4.5).

## **4.2 Theory and Previous Measurements**

### **4.2.1 Ground State Sodium-Argon Interaction Potential**

A large existing body of theoretical and experimental work on the sodium-argon system, made it an attractive candidate for our own study. The interaction potential

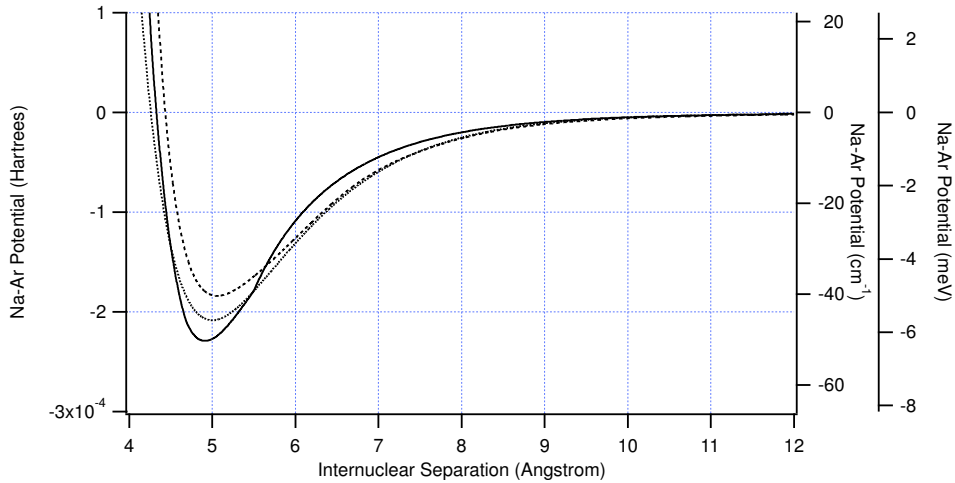


Figure 4-1: Sodium-argon interaction potentials. Long range van der Waals attraction and short range electrostatic repulsion combine to create a well of depth  $\approx 2 * 10^{-4}$  Hartrees ( $\approx 40 \text{ cm}^{-1}$ ) at an internuclear spacing of  $\approx 5 \text{ \AA}$ . The solid curve is a theoretical model based on a modified form of the Born-Mayer potential [114]. The dotted curve is a Morse potential (fit to data from various atom-atom scattering experiments) to which a van der Waals tail (calculated theoretically) has been added [39]. The dashed curve is a modified 6-12 potential with parameters determined from measurements of the differential sodium-argon scattering cross section [31].

between a sodium and argon consists of a short range repulsion (due to the exchange interaction and electrostatic repulsion) and a long range van der Waals attraction forming a well at an intermediate distance about  $\approx 5 \text{ \AA}$  (see Figure 4-1).

A variety of experiments have probed the sodium-argon interatomic potential. These experiments fall into of three general categories: measurements of the differential or total sodium-argon scattering cross section, measurements of sodium optical line broadening in the presence of an argon gas, and NaAr molecular spectroscopy. In analyzing the experimental results, a relatively simple functional form with several free parameters is typically used to approximate the true potential. The parameters are adjusted to give the best fit to experimental data. Among the most commonly invoked approximate functional forms are the Lennard-Jones 6-12 potential,

$$V(r) = \frac{-\lambda_6}{r^6} + \frac{\lambda_{12}}{r^{12}}, \quad (4.1)$$

the Morse potential,

$$V(r) = D \left[ e^{-2\alpha(r-r_0)} - 2e^{-\alpha(r-r_0)} \right], \quad (4.2)$$

and the modified Born-Mayer potential,

$$V(r) = Ae^{-Br} - \sum_{n=6,8,10} \frac{C_n}{r^n}, \quad (4.3)$$

where, in each case,  $r$  refers to the internuclear separation. As more experiments have been performed, variations of these potentials have been introduced to allow more flexibility in fitting experimental results. To date, the cross-section measurements have provided the most precise overall determination the sodium-argon ground state potential, with spectroscopic results more accurate near the potential minimum. Ab initio calculations of the potential have been performed [11, 87, 103], but due to uncertainty in how to handle the hard core, they differ significantly in their prediction of the well-depth and location.

An estimate of the mutual consistency of previous experiments and calculations can be obtained from a comparison of the potential minimum,  $D_e$ , and its location,  $r_m$ , derived from each (see Table 4.1). Although this comparison is hindered by the lack of error estimates, the agreement between theory and experiment on the value of  $r_m$  is reasonably good, while the theoretical predictions for  $D_e$  are 10-20% greater than experimental results.

### 4.2.2 Matter-Wave Index of Refraction: Theory

Interferometric measurements of the matter-wave index of refraction [55, 105] have shown promise as a new method for the refinement of interatomic potentials [39]. These measurements are sensitive simultaneously to the short- and long-range interaction potential, and thus are a valuable complement to existing experiments. In this section, we introduce the matter-wave index of refraction and derive its relationship to the interatomic potential.

Consider an atomic plane wave passing through a region of target gas located

Source	$D_e$ ( $10^{-4}$ a.u.)	$r_m$ (Å)
Exp. (Molecular Spectroscopy) [107]	1.77	4.99
Exp. (Scattering Cross Section) [32]	1.88	4.8
Exp. (Scattering Cross Section) [19]	2.04	5.01
Exp. (Scattering Cross Section) [31]	$1.95 \pm .05$	$5.05 \pm 0.1$
Theory (Pseudopotential) [11]	2.29	4.97
Theory (Pseudopotential) [87]	1.97	5.03
Theory (Configuration Interaction) [103]	2.52	5.01
Theory (Self-Consistent Field Theory + long range van der Waals) [114]	2.33	4.91

Table 4.1: A summary of published values for the sodium-argon potential minimum ( $D_e$ ) and its location ( $r_m$ ). The first four sets of parameters were obtained from fits to experimental data; the type of experiment is indicated in parenthesis. The last four were derived from ab initio calculations; the method of calculation is indicated in parenthesis.

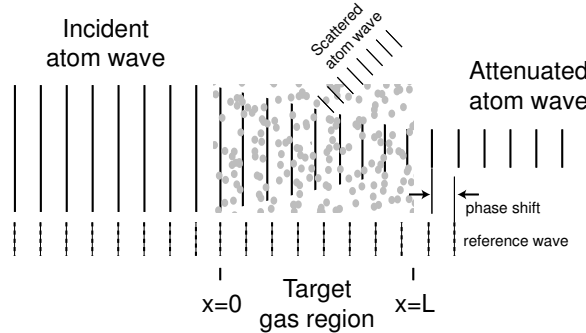


Figure 4-2: Illustration of the attenuation and phase shift of matter waves as they pass through a target-gas region located between  $0 < x < L$ . Within the gas region, incident atoms are subject to an average attractive potential which causes their wavevector to increase and leaves them phase shifted with respect to a reference wave when they emerge. The target gas also scatters a fraction of the incident atomic flux out of the original beam path. These two effects are parameterized in the real (phase shift) and imaginary (attenuation) components of the matter-wave index of refraction.

between  $x = 0$  and  $x = L$  (see Figure 4-2). For  $x < 0$ , we assume a wavefunction of the form:

$$\psi_{x<0}(x) = e^{ik_0x}, \quad (4.4)$$

where  $k_0$  is the wavevector of the incident atom. Within the target-gas region, the atom interacts with the atoms/molecules of the target gas and emerges phase shifted and with a reduced amplitude in the forward direction:

$$\psi_{x>L}(x) = e^{ik_0x} e^{i\hat{\phi}NL} e^{-\hat{\sigma}NL} + \sum_{\vec{k} \neq k_0\hat{x}} c(\vec{k}) \langle x | \vec{k} \rangle, \quad (4.5)$$

where  $N$  is the column density of scatterers in the gas,  $L$  is the length of the gas region, and  $\hat{\phi}$ ,  $\hat{\sigma}$  are dimensionless parameters. The first term in Eqn. 4.5 represents the portion of the atom wave that continues in the original direction, while the second term represents the amplitude for the incident atom to scatter into a different final momentum state.

The attenuation and phase shift of the atom wave that occurs within the gas region can be parameterized into a single, complex-valued index of refraction:

$$\psi_{x>L}(x) = e^{i(n-1)k_0L} e^{ik_0x} + \sum_{\vec{k} \neq k_0\hat{x}} c(\vec{k}) \langle x | \vec{k} \rangle, \quad (4.6)$$

where:

$$n = 1 + \frac{1}{k_0} (\hat{\phi} + i\hat{\sigma})N. \quad (4.7)$$

This matter-wave index of refraction is directly related to the forward scattering amplitude,  $f(|\vec{k}|, \theta = 0)$ , for a collision between an atom and gas particle [8, 38, 121]:

$$n = 1 + \frac{2\pi}{k_0} \left\langle \frac{f(k_r, 0)}{k_r} \right\rangle N \quad (4.8)$$

where  $k_r$  is the atom's wavevector in the center of mass frame of the collision. The  $\langle \rangle$  indicate an average over  $k_r$  to account for the velocity distribution of the target-gas atoms (see Section 4.2.4). Comparing Eqns. 4.7 and 4.8, we arrive at expressions for

the two dimensionless parameters:

$$\begin{aligned}\hat{\sigma} &= 2\pi \left\langle \frac{\text{Im}[f(k_r, 0)]}{k_r} \right\rangle \\ \hat{\phi} &= 2\pi \left\langle \frac{\text{Re}[f(k_r, 0)]}{k_r} \right\rangle.\end{aligned}\quad (4.9)$$

Of several different techniques for calculating  $f(k_r, 0)$ , partial wave theory is the most commonly used in literature discussing the matter-wave index of refraction. Using partial wave theory, the real and imaginary parts of  $f(k_r, 0)$  are calculated as a sum over the angular momentum components of the collision [101]:

$$\begin{aligned}\text{Im}[f(k_r, 0)] &= \sum_l \frac{(2l+1)}{k_r} \sin^2 \delta_l \\ \text{Re}[f(k_r, 0)] &= \sum_l \frac{(2l+1)}{2k_r} \sin 2\delta_l\end{aligned}\quad (4.10)$$

where  $\delta_l$  is the phase shift for the partial wave of angular momentum  $l$ .

The  $\delta_l$ 's are commonly calculated using either the eikonal or JWKB approximations. The JWKB method is more accurate and more computationally intensive of the two methods. The method is valid in regions where the interatomic potential varies slowly compared to the incident atom's wavelength. Near classical turning points where this assumption breaks down, standard formulas are used to smoothly connect the wavefunctions on either side of the turning point. The result is derived in many texts [101]:

$$\delta_l = \frac{\sqrt{2\mu}}{\hbar} \int_0^\infty \sqrt{E - V(r) - \frac{\hbar^2 l(l+1)}{2\mu r^2}} dr + \frac{\pi}{2} l - k_r r_0 + \frac{\pi}{4} \quad (4.11)$$

where  $\mu$  is the reduced mass of the system and  $r_0$  is the classical turning point.

A slightly less accurate [54] result can be obtained using the eikonal approximation in which one assumes that the incident atom travels past the scatterer along a straight-line trajectory. To calculate the phase shift for a partial wave of angular momentum  $l$ , one assumes a trajectory with impact parameter,  $b$ , chosen to give the appropriate angular momentum (i.e.  $b = l/v_r$ , where  $v_r = \hbar k_r/\mu$ ). The phase shift is computed

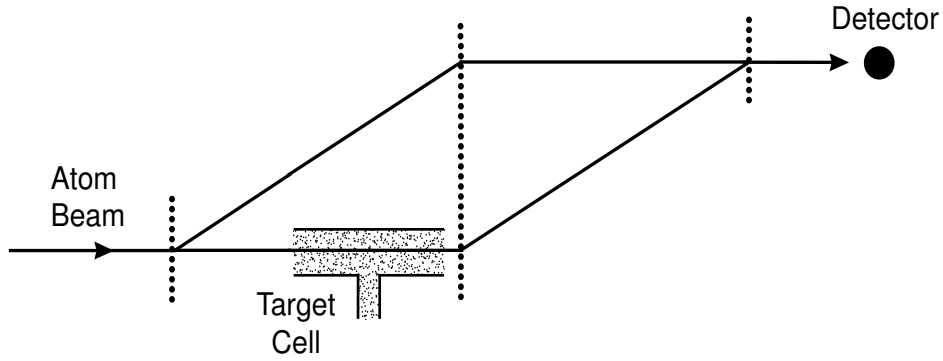


Figure 4-3: Schematic of the apparatus needed to measure the matter-wave index of refraction. A target-gas cell is introduced around one arm of a two path interferometer. The real and complex components of the matter-wave index of refraction can be deduced from the phase shift and attenuation that occurs when the cell is filled with gas.

as the integral of the interatomic potential along this trajectory:

$$\delta_l = \frac{-1}{\hbar v_r} \int V(\sqrt{b^2 + z^2}) dz. \quad (4.12)$$

To calculate the theoretical curves presented in this chapter, we have used the eikonal approximation exclusively.

### 4.2.3 Interferometric Measurement of the Index of Refraction

This section describes how a separated-beam atom interferometer may be used to measure the matter-wave index of refraction. The only additional apparatus needed is a cell, introduced around one interfering arm, which can be empty or filled with target-gas. A schematic of this arrangement is shown in Figure 4-3.

With no gas in the cell, the interference signal (atom flux versus grating phase) is given by:

$$I(\phi_g) = b + |a_1|^2 + |a_2|^2 + 2|a_1 a_2| \cos(\phi_g + \phi_{12})$$

$$= I_0[1 + C \cos(\phi_g + \theta)] \quad (4.13)$$

where  $a_{1,2}$  are the amplitudes of the two interfering paths,  $\phi_{12}$  is their phase difference, and  $b$  is the background count rate (i.e. from other, non-interfering diffraction orders). In the second line of Eqn. 4.13, we have introduced the mean count rate,  $I_0$ , contrast,  $C$ , and phase,  $\theta$ , of the interference pattern:

$$\begin{aligned} I_0 &= b + |a_1|^2 + |a_2|^2 \\ C &= \frac{2|a_1 a_2|}{b + |a_1|^2 + |a_2|^2} \\ \theta &= \phi_{12}. \end{aligned} \quad (4.14)$$

At this point, we also identify the amplitude of the sinusoidal interference fringes,  $CI_0 = 2|a_1 a_2|$ , which is independent of the background count rate.

When the cell is filled with gas, the atom wave passing through the cell will be phase shifted and attenuated according to Eqn. 4.5:

$$a_1 \rightarrow a_1 e^{i\hat{\phi}\eta} e^{-\hat{\sigma}\eta}. \quad (4.15)$$

(For reasons discussed in Section 3.5 and in Ref. [54], we can neglect the second term in Eqn. 4.6 and considered only the forward-scattered portion of the incident atomic flux). Also, because the density of gas within the target cell is in general not a constant, we have replaced the factor  $NL$  from Eqn. 4.5 with an effective number of scatterers defined by the integral:

$$\eta = \int_{-\infty}^{\infty} dx N(x), \quad (4.16)$$

where  $N(x)$  is the column density of gas in the target cell.

Using Eqn. 4.15 we find that the measured interference pattern with gas in the cell is given by:

$$I(\phi_g) = b + |a_1|^2 e^{-2\hat{\sigma}\eta} + |a_2|^2 + 2|a_1 a_2| e^{-\hat{\sigma}\eta} \cos(\phi_g + \phi_{12} + \hat{\phi}\eta)$$

$$= I'_0[1 + C' \cos(\phi_g + \theta')], \quad (4.17)$$

where,

$$\begin{aligned} I'_0 &= b + |a_1|^2 e^{-2\hat{\sigma}\eta} + |a_2|^2 \\ C' &= \frac{2|a_1 a_2| e^{-\hat{\sigma}\eta}}{b + |a_1|^2 e^{-2\hat{\sigma}\eta} + |a_2|^2} \\ \theta' &= \phi_{12} + \hat{\phi}\eta, \end{aligned} \quad (4.18)$$

and the new interference fringe amplitude is  $C'I'_0 = 2|a_1 a_2| e^{-\hat{\sigma}\eta}$ .

From the interference patterns measured with and without gas in the cell, we obtain the two experimental parameters:

$$\phi_{exp} = \theta' - \theta = \hat{\phi}\eta \quad (4.19)$$

$$\sigma_{exp} = -\ln \left[ \frac{C'I'_0}{CI_0} \right] = \hat{\sigma}\eta. \quad (4.20)$$

Because it is impractical to measure the density profile  $N(x)$  of gas in the target cell (needed to compute  $\eta$ ), we instead compute the ratio,

$$\rho_{exp} = \frac{\phi_{exp}}{\sigma_{exp}} = \frac{\hat{\phi}\eta}{\hat{\sigma}\eta} = \frac{\hat{\phi}}{\hat{\sigma}} \quad (4.21)$$

which we can compare directly with a theoretical prediction based on Eqns. 4.9.

#### 4.2.4 Velocity Averaging and Glory Oscillations

Before a direct comparison between theory and experiment can be made, Eqns. 4.9 must be appropriately averaged over a distribution of collision wavevectors,  $k_r$ . The appropriate distribution function, for a target gas of mass  $m_t$  in thermal equilibrium (at temperature  $T$ ) and an incident atomic wave of mass  $m$  and fixed velocity  $v_0 = \hbar k_0/m$  has been derived by Champenois et. al. [22]:

$$P(v_r) = \frac{2v_r^2}{\alpha\sqrt{\pi}v_0^2} \frac{m_t}{m+m_t} e^{-\frac{v_0^2+v_r^2}{\alpha^2}} \left[ \cosh\left(\frac{2v_r v_0}{\alpha^2}\right) - \frac{\alpha^2}{2v_r v_0} \sinh\left(\frac{2v_r v_0}{\alpha^2}\right) \right] \quad (4.22)$$

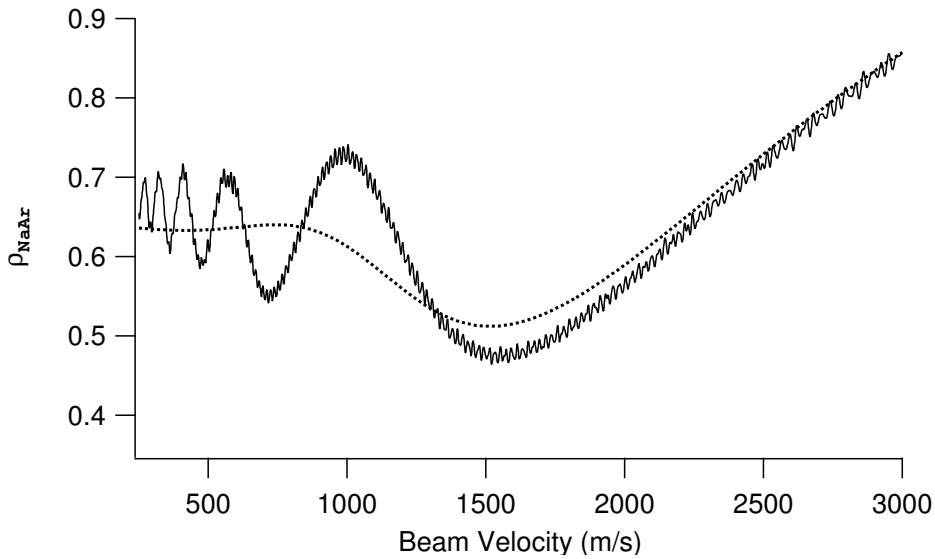


Figure 4-4: Two calculations of the sodium-argon index of refraction, based on the modified morse potential published in Ref. [39]. The thin, jagged line represents a calculation with no thermal averaging, while the dotted line includes an average over the velocity distribution of an argon target gas in thermal equilibrium at room temperature (300K). The fine-scale structure in the unaveraged curve results from imperfect numerical integration and is not physical.

where  $\alpha = 2k_bT/m_t$ . This velocity distribution can be converted into a wavevector distribution with the substitution  $k_r = \mu v_r/\hbar$ , where  $\mu$  is the reduced mass of the colliding particles.

Figure 4-4 shows the effect of velocity averaging on the predicted functional form of  $\rho_{\text{NaAr}}$ . The unaveraged curve exhibits large-scale oscillations in  $\rho_{\text{NaAr}}$  as a function of velocity. These are the glory oscillations referred to at the beginning of the chapter. They result from the interference of the two forward-scattered paths in a sodium-argon collision (see Figure 4-5). The phase difference between these paths varies with relative collision velocity and the paths alternately interfere constructively and destructively. This interference causes the characteristic oscillations in the phase and amplitude of the total forward-scattered wavefunction.

The damping of glory oscillations at beam velocities  $\leq 1500$  m/s is the most significant effect of velocity averaging (see Figure 4-4). Because the velocity average

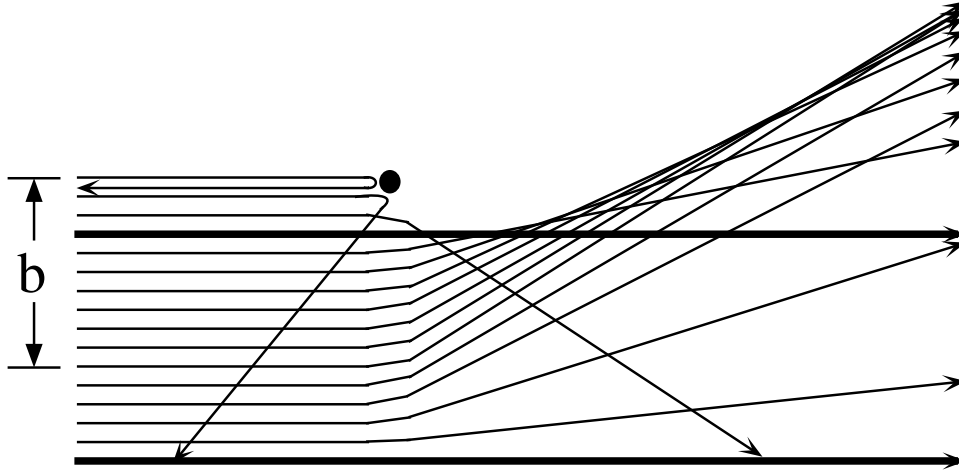


Figure 4-5: Schematic illustration of various atom-atom scattering trajectories as they depend on impact parameter,  $b$ . At large impact parameter, the incident atom continues undeflected (i.e. is forward scattered). At intermediate impact parameters, the atoms experience a van der Waals attraction, and at very small impact parameters, they experience hard-core repulsion. In between these two regimes is another impact parameter for which the incident atom is forward scattered.

makes glory oscillations more difficult to observe, one goal for future experiments is to narrow the velocity distribution of the target-gas atoms (see Section 4.5).

Strictly, an average over the velocity/wavevector distribution of the atomic beam ( $v_0 = \hbar k_0/m_{Na}$ ) must also be performed. It is important to note that the procedure for averaging over  $k_0$  is different from that for  $k_r$ . Whereas each individual incident atom interacts coherently with thousands of target atoms [54], the ensemble of atoms in the beam exist in an incoherent superposition of different velocities [99], each velocity forming its own independent interference pattern. What is ultimately measured is a classical average over these patterns. To average over  $k_0$ , it is the weighted average of interference patterns that must be calculated, rather than average values of  $\hat{\sigma}$  and  $\hat{\phi}$ . Because of the relatively narrow velocity distribution of a supersonic beam compared to a thermal gas, this second average can be safely neglected at the level of sensitivity of current experiments. However, it may be important to include an average over  $k_0$  in future experiments.

### 4.2.5 Previous Index of Refraction Measurements

Two previous experiments have been performed to measure the matter-wave index of refraction, both using the MIT atom interferometer. In 1995, Schmeidmeyer et. al. [105] measured the index of refraction of nine target gases (including argon) for sodium matter waves, but only at a single<sup>1</sup> sodium beam velocity ( $\approx 1000$  m/s). The results obtained were in rough agreement with theoretical predictions, but were not precise enough to be useful in refining interatomic potentials [22].

In 1997, Hammond et. al. [54, 55] studied the velocity dependence of the sodium-argon index. With the goal of observing glory oscillations,  $\rho_{\text{NaAr}}$  was measured over a range of sodium-beam velocities between 1000 and 2500 m/s. The data obtained suffered from unexpectedly large statistical errors. These errors were ultimately blamed on problems with the hot-wire/CEM detector and on large zero-phase drifts which occurred while the gas cell was filled/evacuated (see Section 4.4.5). The results were also systematically higher than theoretical predictions.

The results of these two previous experiments are shown in Figure 4-6. Also shown are theoretical predictions based on three representative interatomic potentials. A comparison of the theory and data suggests two requirements for any future studies of the sodium-argon index. First, the statistical error bars should be reduced in order for the damped glory-oscillation structure to become visible in the experimental data. Second, any factors that might be systematically affecting the measurements (especially at high-velocities) should be identified and either eliminated or corrected in post-analysis. The new measurements of  $\rho_{\text{NaAr}}$  described in this chapter address both of these issues.

## 4.3 Experiment

This section describes new measurements of  $\rho_{\text{NaAr}}$  as a function of sodium beam velocity. A description is given of the apparatus and procedures, highlighting improvements

---

<sup>1</sup>A limited amount of data was collected at other atom-beam velocities, but, due to questionable accuracy, was not published.

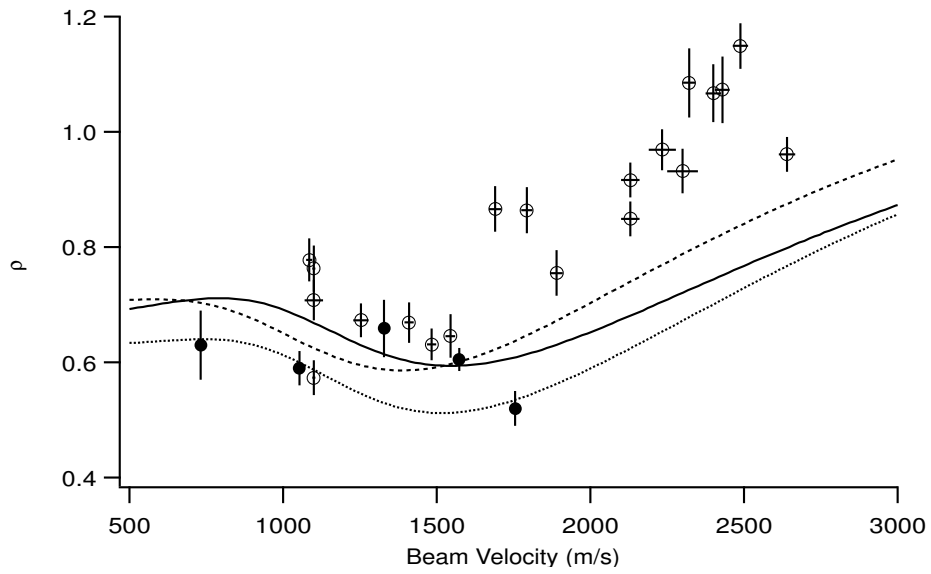


Figure 4-6: Previous measurements of  $\rho_{\text{NaAr}}$ . The filled circles (●) are values published by Schmeidmeyer et. al. [105] combined with unpublished results taken at the same time. The open circles (○) are values obtained by Hammond et. al. [54, 55]. Also shown are three theoretical predictions for  $\rho_{\text{NaAr}}$  based on the model potentials displayed in Figure 4-1.

over previous experiments. The new measurements are then presented and discussed.

### 4.3.1 Apparatus and Procedures

The apparatus (see Figure 4-7) and data-collection procedures for the current index of refraction experiment were largely similar to the previous two [54, 105]. We reused the target-gas cell employed by Hammond et. al., consisting of a 10  $\mu\text{m}$  thick silicon wafer (the “septum”) bonded to a 2 inch diameter glass flat into which a 3 mm tall, 5 mm deep channel had been cut (see Figure 4-8). The cell is connected to a low-pressure gas reservoir via 1/4 inch diameter tubing. The cell could be filled with gas from the reservoir by opening valve PV1 and closing valve PV2 — this will be referred to as the “gas-on” configuration below. To empty the gas cell, we closed valve PV1 and opened PV2, allowing gas in the cell to vent through two feet of 1/4 inch diameter tubing into the main vacuum chamber — this valve setting will be referred to as the “gas-off” configuration.

The equilibrium “gas-on” pressure of argon in the target cell is proportional to the argon pressure in the target-gas reservoir. We estimate the pressure in the target-gas cell to have been  $\approx 1/7$  of that in the target reservoir, based on beam attenuation measurements combined with calculations of the total scattering cross section. We operated the reservoir at argon pressures between 1 and 5 mTorr, adjusted by balancing the flow into the reservoir of pure argon gas from a high-pressure gas cylinder against the pumping speed of a turbo pump connected to the reservoir. The flow into the reservoir was controlled via an adjustable leak valve (LV). The pumping speed was restricted by partially closing a gate valve (GV) just above the pump inlet (see Figure 4-7).

To set up the experiment, we began by measuring a reference diffraction pattern produced by a collimated atom beam through the first diffraction grating. We then inserted the target-gas cell, which is located a few centimeters upstream of the second diffraction grating, such that the septum was positioned halfway between the 0th and 1st diffracted orders (the two orders that would eventually form the atom interferometer). The septum was wide enough that, even when carefully aligned, it attenuated

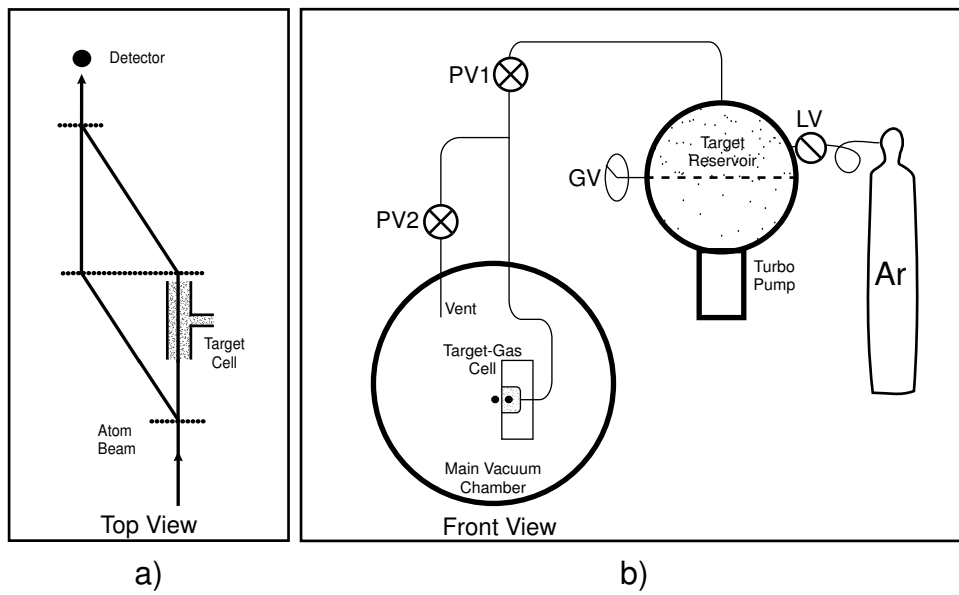


Figure 4-7: Schematic of the apparatus used to measure  $\rho_{\text{Na,Ar}}$ . (a) A target-gas cell was inserted into one arm of the atom interferometer. (b) The target cell was filled into from a larger target-gas reservoir, and emptied by venting into the main vacuum chamber. The dots on either side of the target-gas cell membrane represent the two paths of the interferometer.

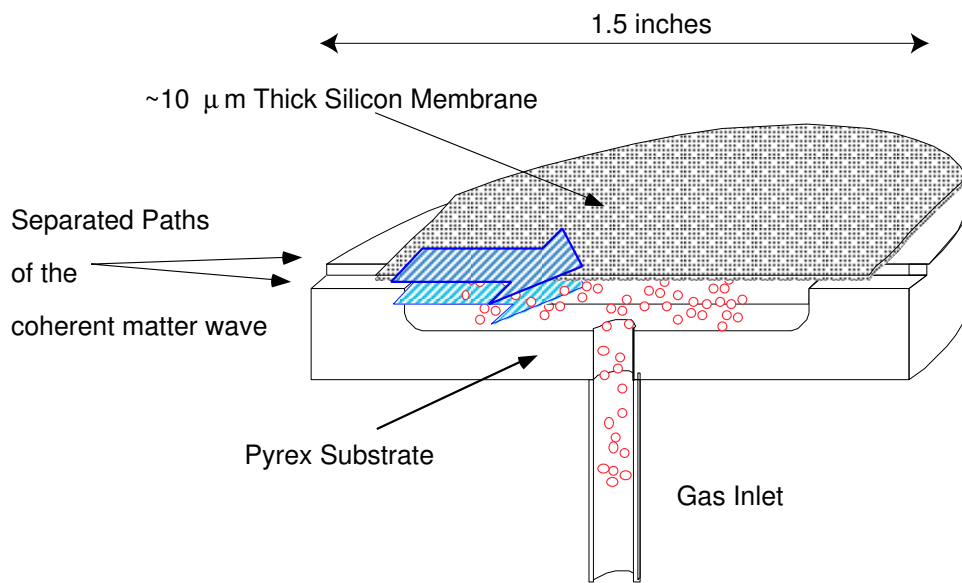


Figure 4-8: Schematic of the target-gas cell (described in detail in Ref. [54]). The cell consists of a  $10\ \mu\text{m}$  thick silicon membrane (the “septum”) anodically bonded to a  $1/4$  inch thick pyrex substrate into which a channel has been cut. As the two atom interferometer arms pass on either side of the silicon membrane, only one is exposed to the target gas.

both the 0th and 1st orders to some extent. Comparing diffraction patterns with the target cell in place to the reference diffraction pattern, we fine tuned the transverse alignment of the target cell until the both the 0th and 1st orders were attenuated by the same factor (to within 5 – 10%).

There are three advantages in positioning the target-gas cell around the 0th order of the first diffraction grating. First, due to its finite velocity width, a 1st order diffracted atomic beam is slightly wider than a 0th order beam (see Appendix A). By inserting the target-gas cell upstream of the second diffraction grating, we were working with the narrowest possible pair of diffracted orders and therefore allowing more space for the septum between them. Second, the most significant background signal from a non-interfering order (see Section 2.3.3) is due to the component of the atomic beam that is 0th order diffracted at both the first and second gratings. This is simply because the 0th order has the largest amplitude of any diffraction order. Thus, by choosing to attenuate the 0th as opposed to the 1st order when the gas-cell is filled, we more significantly reduce the background signal from non-interfering orders.

The third advantage is that attenuating the 0th order allows us to maximize our signal-to-noise ratio ( $S/N = C\sqrt{I_0}$ ) for the gas-on measurements. We deliberately used a first grating whose open fraction was slightly larger (0.56 versus 0.54) than ideal<sup>2</sup>, that is, a grating whose ratio of 0th order to 1st order diffraction is too large. In the gas-off configuration, using the larger open fraction grating resulted in a higher mean count rate, but smaller contrast and smaller overall signal to noise versus the ideal case. However, in the gas-on configuration, we effectively reduced the ratio of 0th order to 1st order diffraction amplitudes, bringing it closer to the ideal value. This resulted in an actual increase the contrast of the interference pattern for some of our gas-on data (see Figure 4-9). Overall,  $S/N$  was still smaller for the gas-on versus the gas-off data, but was larger than it would have been were the 1st order attenuated or a first grating of the “ideal” open fraction used.

---

<sup>2</sup>Where “ideal” is defined as the configuration of available open fractions that yields the highest measured signal-to-noise.

With the gas cell in place, the procedure for making a single measurement of  $\rho_{\text{NaAr}}$  was as follows. First, in the gas-off configuration, we acquired interference data for 5-10 seconds. The precise duration was chosen such that we could statistically resolve the phase of the interference pattern to  $\approx 0.1$  mrad. This first set of interference data was fit to Eqn. 4.13 to obtain  $C$ ,  $I_0$ , and  $\theta$ . Next we switched to the gas-on configuration and collected another 6-20 seconds of interference data. A larger time interval was often used for the second set of data because of the reduction in signal to noise caused by attenuation of the 0th order beam. The second set of data was fit to Eqn. 4.17 to obtain  $C'$ ,  $I'_0$ , and  $\theta'$ . Alternating gas-on and gas-off measurements were repeated 80-100 times, at a fixed reservoir pressure and beam velocity, to obtain one 20-minute “dataset.”

Figure 4-9 shows the fit results for a typical dataset. These data were further reduced as follows. First, any zero-phase drift was eliminated using an interpolation procedure similar to the one described in Section 3.3.4. Next, we determined  $\phi_{exp}$  (Eqn. 4.19) for each gas-on fringe by subtracting the interpolated gas-out phase from the measured gas-on phase. We then determined  $\sigma_{exp}$  (Eqn. 4.20) by taking the ratio of the gas-on to gas-off interfering amplitude (the interfering amplitude did not drift significantly from cycle to cycle). With these values we then generated a plot of  $\phi_{exp}$  to  $\sigma_{exp}$  (see Figure 4-10) to which we fit a straight line, fixed to pass through the origin. This fit yields a single value of  $\rho_{\text{NaAr}}$  (Eqn. 4.21) for the entire dataset.

### Adjusting the beam velocity

The mean velocity of the beam generated in our supersonic source (see Section 2.2.1) is given by:

$$v = \sqrt{\frac{5k_bT}{\bar{m}}} \quad (4.23)$$

where  $T$  is the temperature of the escape nozzle (typically 750°C) and  $\bar{m}$  is an effective mass of all particles in the beam weighted by their partial pressures (or equivalently their mole fractions):

$$\bar{m} = \frac{\sum_i m_i p_i}{\sum_i p_i}. \quad (4.24)$$

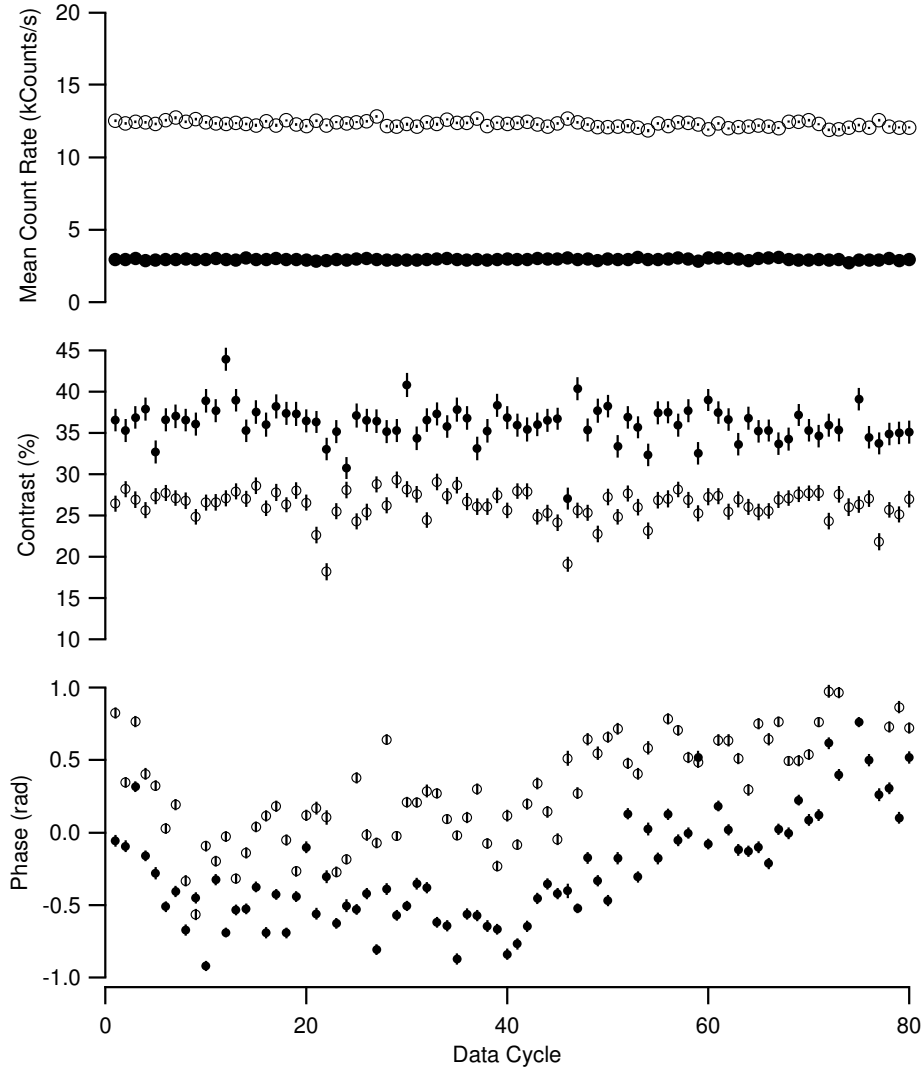


Figure 4-9: Mean count rate, contrast, and phase of measured interference patterns in the gas-on ( $\bullet$ ) and gas-off ( $\circ$ ) configurations for a  $v = 1564$  m/s sodium beam. The target reservoir pressure was 1.95 Torr. Because the amplitude of the interfering arm passing through the (initially empty) gas cell was larger than that passing outside the cell, the contrast actually increases from 26% to 36% when the gas cell is filled (though overall the  $S/N$  decreased from 29 to 19). A distinct phase shift between the gas-on and gas-off configurations is evident atop a slowly varying phase drift. This phase drift dominates our error in determining  $\phi_{exp}$ . From the 80 cycles of data displayed here, acquired in approximately 20 minutes, we found  $\rho_{\text{NaAr}} = 0.55 \pm 0.03$ .

To study the velocity dependence of  $\rho_{\text{NaAr}}$ , we adjusted the atomic beam velocity between datasets by varying the effective mass of the carrier gas mixture. We created a controlled mixture of two noble carrier gases using a pair of gas flow meters, with which we could produce any desired effective mass between 4 amu ( $= m_{\text{He}}$ ) and 130 amu ( $= m_{\text{Xe}}$ ).<sup>3</sup>

We found experimentally that it takes between 1/2 and 1 hour for the beam velocity to stabilize to within 1% of the new velocity after the flow controller settings are adjusted. We measured the beam velocity at the beginning and end of every dataset, and waited long enough after the flow controller adjustment that the velocity had stabilized to within 3% before beginning any data collection.

### 4.3.2 Improvements over Previous Experiments

The most significant improvement over the previous experiment of Hammond et. al. is that, for an equal or even smaller quantity of data, we have been able to reduce the statistical error bars on the measured value of  $\rho_{\text{NaAr}}$  by a factor of two. Two factors primarily account for the reduction in statistical error: better monitoring of zero phase drift and optimization of the pressure in the gas cell.

#### Zero-Phase Drift

In order to determine  $\phi_{exp}$ , we subtract the interpolated gas-out phase (zero-phase) from the gas-in phase (Eqn. 4.19). Because we cannot measure both phases simultaneously, we must interpolate adjacent zero-phase measurements to find the true zero phase at the moment the gas-in phase is measured. The interpolation becomes more reliable when there is less overall zero-phase drift and when the zero phase is measured more often.

In previous experiments, the typical zero-phase drift was 10 rad/hour. As a result of our improvements to the thermal stability and vibration isolation of the interfer-

---

<sup>3</sup>Within the source oven, the sodium partial pressure ( $< 5$  Torr) is typically less than 1% of carrier gas pressure ( $\approx 1800$  Torr). We therefore ignore the sodium contribution to the effective mass when calculating the ratio of carrier gas pressures necessary to achieve a desired velocity.

ometer (see Section 2.3.3), this drift rate has been reduced by nearly an order of magnitude to 1-2 rad/hour.

In the previous experiment, zero-phase measurements were made at a rate of  $\approx 1$  per minute. The limiting factor in this rate was the  $\approx 50$  s time constant for filling the gas cell (the emptying time was a small fraction of the filling time constant). In the current experiment we have been able to reduce the filling/emptying time constants to  $\approx 1$  s by shortening the length of tubing between PV1 and the gas cell, and by increasing the size of the gas tube leading from the pressure reservoir to the gas cell (from an inner diameter of 1/32 inch to 1/4 inch). This improvement allowed us to take zero-phase measurements at a rate of  $\approx 6$  per minute, leading to a much better determination of zero-phase drift.

### Optimized Target-Gas Pressure

In addition to allowing zero-phase measurements to be made more often, reducing the filling time constant so dramatically enabled us to take all of the gas-on data at an optimized gas cell pressure. If  $\sigma_{exp}$  and  $\phi_{exp}$  are small compared to their error bars, then the fractional error in  $\rho_{\text{NaAr}}$  is  $\gg 1$ . Thus, the best determination of  $\rho_{\text{NaAr}}$  is obtained from data with a large phase shift/attenuation, though not so large an attenuation that the atom interference pattern is undetectable over the background. Empirically, an attenuation  $e^{-\hat{\sigma}\eta} = e^{-2}$  is best, given our sources of phase noise. In the experiment of Hammond et. al., rather than wait several time constants for the gas cell pressure to equilibrate, data was collected at non-ideal pressures while the cell was filling and emptying. Taking data as the pressure in the gas cell is changing also introduces a systematic error in the measurements of  $\rho_{\text{NaAr}}$  (see Section 4.4.5). Because our filling time constant is now so short, we could afford to wait for the gas cell to come to equilibrium before collecting interference data, and still collect data with an 80% duty cycle.

The net result of these improvements can be seen in Figure 4-10, comparing a 50 minute long dataset from the previous experiment to a 20 minute long dataset from the current experiment. The statistical error in the final value for  $\rho_{\text{NaAr}}$  deduced from

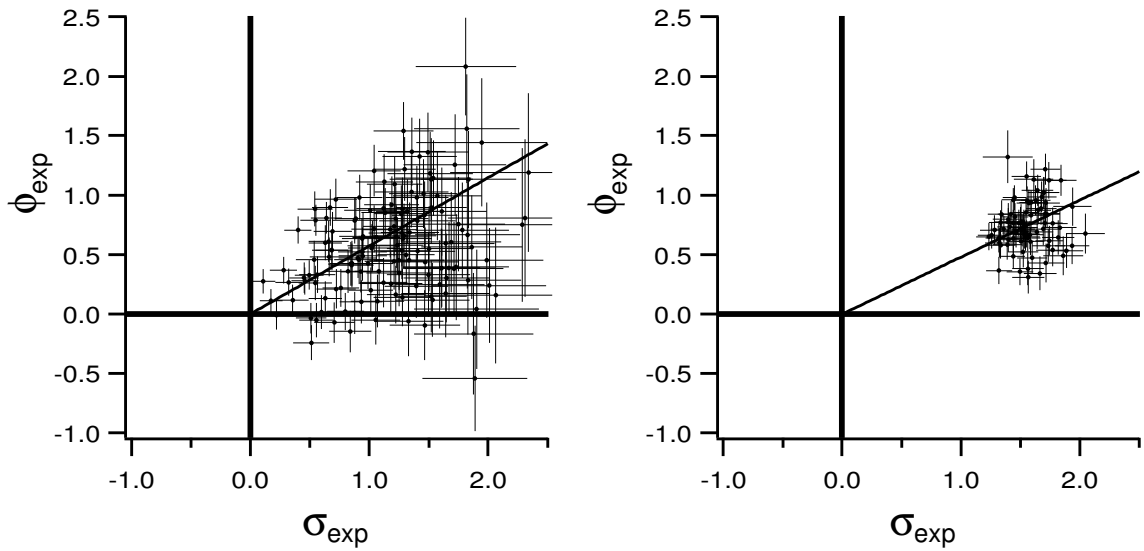


Figure 4-10: (Left) Plot of  $\sigma_{exp}$  versus  $\phi_{exp}$  from a typical 50 minute long dataset from the previous index of refraction experiment of Hammond et. al. [54] representing about 1 hour of data. A linear fit, fixed to pass through the origin, yields  $\rho_{NaAr} = 0.57 \pm 0.03$ , with a  $\chi^2$  of 40.4. (Right) Plot of  $\sigma_{exp}$  versus  $\phi_{exp}$  from a typical 20 minute long dataset from the current experiment. A linear fit to this data yields  $\rho_{NaAr} = 0.479 \pm .015$  with a  $\chi^2 = 3.7$ .

the current experimental data is half as large as that of the previous experiment. In addition, the  $\chi^2$  reported from a linear fit to the data has been reduced from 40.4 to 3.7. That the  $\chi^2$  is still larger than one is due to the presence of some remaining technical noise (i.e. zero-phase drift faster than our interpolation procedure can monitor) affecting the current experiment. We have analyzed the  $\sigma_{exp}$  and  $\phi_{exp}$  distributions independently (fit them to a constant) and note that the  $\chi^2$  for  $\phi_{exp}$  is consistently between 1.5 and 10 times larger than that of  $\sigma_{exp}$ , indicating that unaccounted-for phase noise is more significant than contrast noise. We have defined our statistical error bars to include the scatter observed experimentally (as derived from plots like the one in Figure 4-10) rather than simply the shot-noise limit from the actual atom-counting statistics.

We have also made one procedural improvement over the previous experiment. In that experiment, a single experimental run was devoted to measuring the atom-beam velocity as a function of seed gas mixtures. Velocity measurements were not repeated on subsequent evenings when the actual data was collected. We have observed, however, that even using the same flow controller settings, our atom beam velocity varied by as much as 50 m/s from run to run. This variation likely stems from the changes in the source oven temperature and the pressure in the seed gas lines leading to the flow controller. For this reason, in the current experiment we measured the velocity of the atom beam at the beginning of each run, and before and after each adjustment made to the flow controller settings. As a result, our velocity determination in the current experiment was better than  $\approx 10$  m/s.

### 4.3.3 New Measurements

New measurements of  $\rho_{\text{NaAr}}$  as a function of atom-beam velocities in the range 750 – 2200 m/ are plotted in Figure 4-11.

Our high-velocity data ( $v > 1500\text{m/s}$ ) show reasonable agreement with theory. At low velocity, our data falls substantially below the theoretical prediction and below the results of previous measurements. Although there is clearly structure in  $\rho_{\text{NaAr}}$  with respect to velocity, we have not yet observed a complete glory-oscillation cycle.

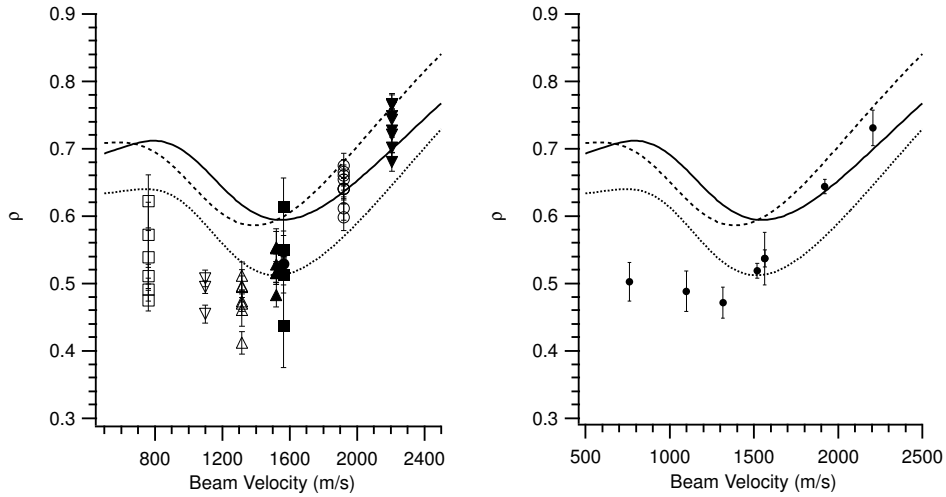


Figure 4-11: Summary of our new measurements of  $\rho_{\text{NaAr}}$  as a function of velocity. Between 2 and 8 datasets were acquired at each velocity. (Left) Results from the individual datasets. (Right) Results after averaging the data collected at a each atom-beam velocity. Also shown are three theoretical predictions for  $\rho_{\text{NaAr}}$  based on the model potentials displayed in Figure 4-1.

The discrepancy between the theory and our low-velocity data indicates a systematic error in the experiment for which we have not yet accounted or a shortcoming in the atomic theory. A thorough analysis of possible systematics is presented in Section 4.4. However, it is also worth studying whether enough flexibility exists within the theory to bring it into agreement with the low-velocity data.

To this end we have studied the low-velocity asymptotic behavior of  $\rho_{\text{NaAr}}$ . We find that as  $v \rightarrow 0$ , the value of  $\rho_{\text{NaAr}}$  is dominated by the long-range behavior of the interatomic potential, which can be represented to high accuracy as a van der Waals expansion:

$$V(r)_{r \rightarrow \infty} \approx -\frac{C_6}{r^6} - \frac{C_8}{r^8} - \frac{C_{10}}{r^{10}} - \dots \quad (4.25)$$

For the sodium-argon system, the currently accepted theoretical values for the van der waals coefficients (in atomic units) are:  $C_6 = 189 \pm 20$ ,  $C_8 = 10,700_{-430}^{+1,560}$ ,  $C_{10} = 835,000_{-115,200}^{+45,400}$  [114]. We have calculated the low-velocity limit of the sodium-argon index assuming a potential of the form given in Eqn. 4.25 and using various values of the van der Waals coefficients consistent with the stated theoretical limits. We find

that  $\rho_{\text{NaAr}}$  varies only between 0.67 (when  $C_6$  is minimized and  $C_{8,10}$  are maximized) and 0.69 (when  $C_6$  is maximized and  $C_{8,10}$  are minimized). Even among theories which hypothesize a different form for the long-range potential, the low velocity asymptote lies between  $\rho_{\text{NaAr}} = 0.64$  and 0.72 (see Figure 4-6).

Thus, uncertainty in the theoretical potential parameters is not large enough to account for the observed discrepancy between theory and experiment. The statistical error bars are not large enough to explain the discrepancy as a statistical fluctuation. We are therefore called to investigate possible systematic effects that might be skewing our measurements.

## 4.4 Analysis of Systematic Errors

The fact that both the current and previous experiments show significant deviation from theory demands an investigation into possible systematic errors. Hammond [54] discusses systematic effects briefly, concluding that none were significant compared to the statistical error bars of his experiment. For the systematic effects he considered, Hammond’s conclusion remains true for the current experiment.

However, we have identified several sources of systematic error that were not previously considered. Some of these are significant in the current experiment and most likely affected the results of the previous experiment as well. An explanation of each source of error is given below, along with an estimate of its contribution to the new sodium-argon index measurements. Where possible, an expression for the fractional shift  $\Delta\rho \equiv \frac{\rho_{\text{exp}} - \rho_{\text{true}}}{\rho_{\text{true}}}$  resulting from the systematic effect is derived. (Note: In this section, wherever  $\rho$  is used without any subscript, we are implicitly referring to the sodium-argon system.)

### 4.4.1 Other Interfering Orders

Our original analysis of the experiment in Section 4.2.3 dealt with only one pair of interfering paths (the “correct” interferometer). This assumption neglects the

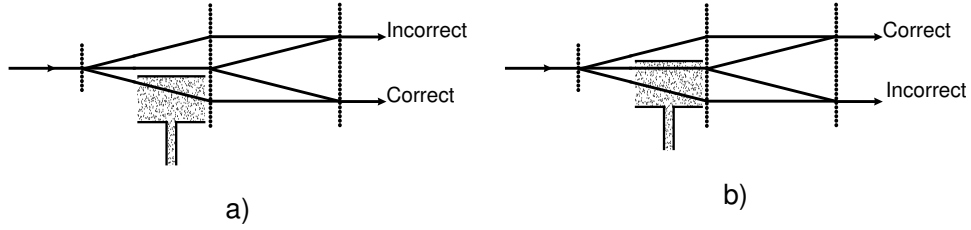


Figure 4-12: Illustration of the two pairs of paths which contribute most significantly to the detected interference signal. Only one of these pairs (labeled “correct”) has one arm passing inside and the other outside the gas cell. The other (labeled “incorrect”) may have both arms (a) outside or (b) inside the cell.

presence of a second<sup>4</sup>, symmetric pair of paths which also contributes to the measured interference signal as shown in Figure 4-12. We refer to this second pair of paths as the “incorrect” interferometer.

Although the correct and incorrect interferometers are spatially displaced from each other, because the atomic beam and detector are not infinitely narrow, there will in general be some fraction,  $f$ , of the detected interference signal that comes from the incorrect interferometer. For a Gaussian-shaped atom beam, of width  $\sigma_b$ , this fraction is:

$$f = e^{-\frac{1}{2} \left( \frac{2\theta_D L}{\sigma_b} \right)^2}, \quad (4.26)$$

where  $\theta_D = \lambda_{dB}/\lambda_g$  is the atom diffraction angle, and  $L$  is the distance from the first to the second atom grating (= 36 inches in the current experiment).

Because the arms of the incorrect interferometer are either both inside or both outside the gas cell, the phase and amplitude of the incorrect interferometer fringes were affected differently than those of the correct interferometer when we switched between gas-on and gas-off configurations. If we repeat the calculations leading to Eqn. 4.19, this time including the contributions of both the correct and incorrect

---

<sup>4</sup>In fact, there are an infinite number of additional interfering involving 2nd or higher diffracted orders. The small amplitude for these orders compared the 0th and 1st renders their contributions negligible.

interferometers, we find:

$$\phi_{exp} = \tan^{-1} \left( \frac{\sin \hat{\phi}\eta}{\cos \hat{\phi}\eta + f e^{\pm\hat{\sigma}\eta}} \right) \approx \hat{\phi}\eta - f \frac{e^{\pm\hat{\sigma}\eta} \sin \hat{\phi}\eta}{2}, \quad (4.27)$$

where in the last step we have approximated  $f$  as a small parameter. The plus sign applies when both paths of the incorrect interferometer pass outside the gas cell, and the minus when the both pass inside (see Figure 4-12).

Similarly, repeating the calculations leading to Eqn. 4.20, we find:

$$\sigma_{exp} = -\ln \left( e^{-\hat{\sigma}\eta} \frac{1 + f e^{\pm\hat{\sigma}\eta}}{1 + f} \right) \approx \hat{\sigma}\eta + f(1 + e^{\pm\hat{\sigma}\eta}). \quad (4.28)$$

Combining equations 4.27 and 4.28, we derive the following estimate of the systematic error caused by the presence of the incorrect interferometer as:

$$\Delta\rho = f \left( \frac{e^{\pm\hat{\sigma}\eta} - 1}{\hat{\sigma}\eta} - \frac{e^{\pm\hat{\sigma}\eta} \sin \hat{\phi}\eta}{\hat{\phi}\eta} \right) \quad (4.29)$$

The effect of this systematic is clearly minimized when both incorrect interferometer paths pass through the gas cell (when the minus signs in Eqn. 4.29 applies). We therefore chose to run the experiment in this configuration (pictured in Figure 4-12b).

Using Eqn. 4.29, we have calculated the systematic error in  $\rho_{exp}$  due to the presence of the “incorrect” interferometer. The results are displayed on the left hand side of Figure 4-13 for several different experimental configurations. The qualitative effect of the incorrect interferometer is to reduce the measured  $\rho$  below it’s true value. The severity of the error is negligible up to a cutoff velocity which is a strong function of  $\sigma_b$ : increasing the beam width by a factor of two dramatically increases the effect of this systematic. On the right hand side of Figure 4-13 we have applied the correction calculated from Eqn. 4.29 to the measured data. The value of  $\sigma_b$  used to correct each dataset was derived from diffraction patterns taken on the same evening. The values of  $\hat{\sigma}\eta$  and  $\hat{\phi}\eta$  were obtained from each dataset itself. The data at  $v = 1565$  m/s and  $v = 2207$  m/s have the largest correction because they were taken at smaller gas

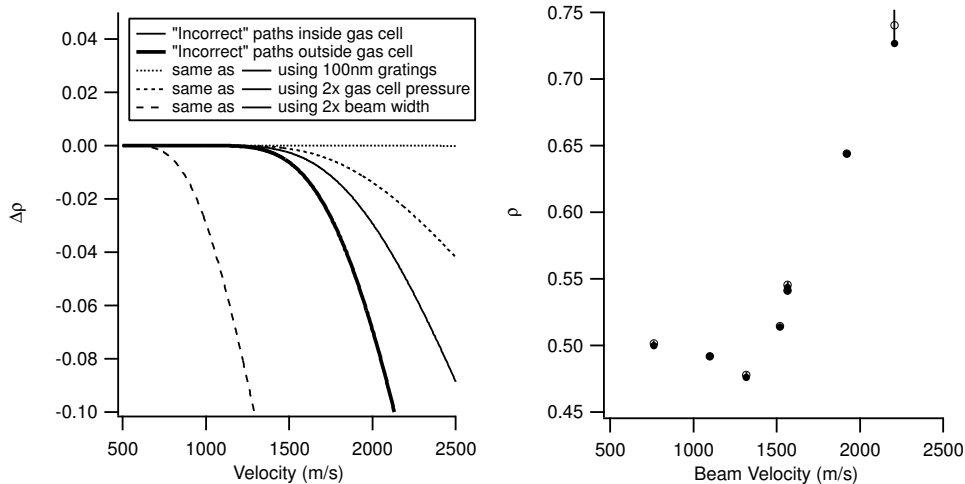


Figure 4-13: (Left) Calculation of the systematic shift caused by the presence of an “incorrect” interferometer. For this calculation, (unless otherwise noted) we have assumed a 200 nm grating period,  $\sigma_b = 0.032$  mm,  $\hat{\sigma}\eta = 1.66$ , and  $\hat{\phi}\eta = 1.21$ , (values appropriate for  $\rho \approx 0.7$ ). (Right) Experimental data corrected for this systematic using Eqn. 4.29. Raw data points ( $\bullet$ ) are shown without error bars. Corrected points ( $\circ$ ), obscured for the most part underneath the experimental data, are shown with error bars corresponding to the uncertainty of the correction.

cell pressures (on average) than data at the other velocities. The uncertainty in the correction arises from an imperfect knowledge of our atomic beam width.

Several approaches might be used to mitigate this systematic error in future experiments. As a first step, the interferometer should always be operated in the configuration such that both of the “incorrect” interferometer paths are attenuated. It may also be possible to block the undesired orders using a translatable razor edge or the edges of the diffraction grating windows themselves. Using smaller period gratings would also offer a huge improvement: if the 200 nm period gratings used in the current experiment were replaced with 100 nm period gratings,  $f$  (and therefore  $\Delta\rho$ ) would be reduced by a factor of  $e^{-4}$ .

#### 4.4.2 Molecule Interferometers

Our original analysis of the experiment in Section 4.2.3 considered a matter-wave beam composed entirely of sodium atoms. This assumption neglects the presence in

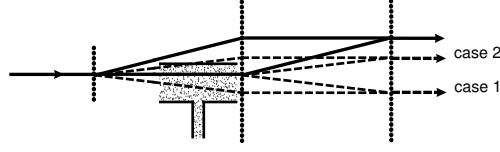


Figure 4-14: Illustration of the two pairs of molecular paths which contribute most significantly to the detected interference signal. One of these pairs (case 1) has both arms passing inside the gas cell. The other (case 2) has one arm obstructed by the target cell membrane.

the beam of a significant fraction (typically 10-15%) of sodium dimers ( $\text{Na}_2$ ), which also contribute to the interference signal. The dimers in our supersonic beam have the same velocity as the atoms but are twice as massive, and therefore have twice the atom's deBroglie wavelength and half the atom's diffraction angle. They also have a different interaction potential with argon, and therefore a different index of refraction. We now proceed to calculate the effect of sodium dimers on the measurement of  $\rho$ .

There are two symmetric molecule interferometers which most significantly contribute to the interference signal (see Figure 4-14). For the molecule interferometer in which both paths pass inside the gas cell (case 1), the fractional shift can be calculated using Eqn. 4.29 from the previous section with the replacements  $\hat{\sigma} \rightarrow \hat{\sigma}_{\text{mol}}$  (the dimensionless attenuation factor for sodium dimers) and  $f \rightarrow f_{\text{mol}}^1$  (the fraction of "case 1" molecules contributing to the detected interference signal).

For the molecule interferometer in which only one arm passes through the gas cell (case 2), the fractional error is given by:

$$\Delta\rho = \frac{f_{\text{mol}}^2}{\hat{\sigma}_{\text{mol}}\eta} \left( (\beta - 1) \cos \Delta\phi - \frac{\beta}{\rho} \sin \Delta\phi \right) \quad (4.30)$$

where

$$\beta = e^{-(\hat{\sigma}_{\text{mol}} - \hat{\sigma})\eta}, \quad (4.31)$$

$f_{\text{mol}}^2$  is the fraction of "case 2" molecules contributing to the detected interference signal, and  $\Delta\phi = (\hat{\phi}_{\text{mol}} - \hat{\phi})\eta$  is the difference in phase acquired by the atoms versus molecules in passing through the gas cell.

Before we can estimate the magnitude of the systematic error caused by molecules, we must determine the parameters  $f_{\text{mol}}^{1,2}$ ,  $\hat{\sigma}_{\text{mol}}$ , and  $\hat{\phi}_{\text{mol}}$ . We calculated  $f_{\text{mol}}^{1,2}$  using Eqn. 4.26, modified to account for the smaller dimer diffraction angle, and multiplied by the fraction of molecules in the atomic beam,  $f^{\text{beam}}$ . To determine  $f_{\text{mol}}^2$ , we included an additional factor to account for the fact that the septum of the target cell attenuates the +1 molecular order by typically more than 80%. This attenuation factor,  $f^{\text{septum}}$ , can be measured by comparing the diffraction pattern of the beam through the first grating, with and without the septum in place.

The final two parameters,  $\hat{\sigma}_{\text{mol}}$  and  $\hat{\phi}_{\text{mol}}$ , are more difficult to estimate since the index of refraction for sodium dimers passing through argon has never been measured. From our own measurements of atom-beam attenuation through a neon target gas, we observed [24] that the total scattering cross section for molecules is  $1.56 \pm 0.03$  times the atomic value. Based on this observation, we crudely estimate  $\hat{\sigma}_{\text{mol}} = (1.5 \pm 0.5)\hat{\sigma}$  for an argon target. We have no similar way of estimating  $\hat{\phi}_{\text{mol}}$ , so we have simply calculated  $\Delta\rho$  while allowing  $\Delta\phi$  to vary over  $2\pi$  and quoted the mean value as our correction, and the range of  $\Delta\rho$  values as our uncertainty in the correction.

Using Eqns. 4.29 and 4.30, we have calculated the systematic error in  $\rho_{\text{exp}}$  due to the presence of molecules. The results are displayed on the left hand side of Figure 4-15 for several different experimental configurations. The error is most significant for case 1 (both interfering molecule paths passing through the gas cell). The error in case 2 turns on at lower velocity, but grows more slowly. On the right hand side of Figure 4-15 we have applied the combined (case 1 and case 2) correction to the measured data. The values of  $\sigma_b$  and  $f^{\text{beam}}$  used to correct each dataset were derived from measurements made on the same evening. The values of  $\hat{\sigma}\eta$  and  $\hat{\phi}\eta$  were obtained from each dataset itself. The data at  $v = 1565$  m/s and  $v = 2207$  m/s have the largest correction because they were taken at smaller gas cell pressures (on average) than data at the other velocities. The uncertainty in the correction is dominated by our complete lack of knowledge of the parameter  $\hat{\phi}_{\text{mol}}$ .

As with the systematic error due to other interfering order, the best way to reduce this error would be to use smaller period diffraction gratings to better isolate the

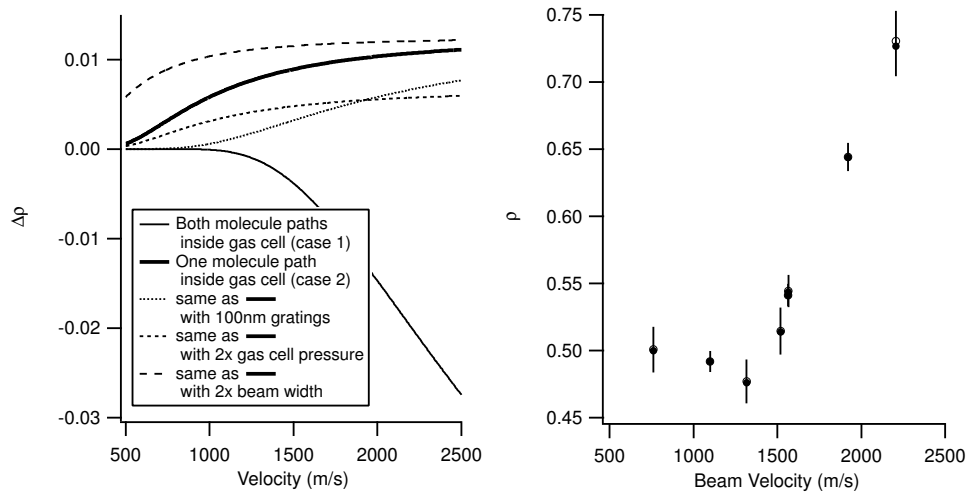


Figure 4-15: (Left) Calculation of the systematic error in  $\rho_{\text{NaAr}}$  due to the presence of molecules in the atomic beam. For this calculation, (unless otherwise noted) we have used:  $\lambda_g = 200$  nm,  $\sigma_b = 0.032$  mm,  $\hat{\sigma}\eta = 1.66$ ,  $\hat{\phi}\eta = 1.21$ ,  $\hat{\sigma}_{\text{mol}} = (1.5 \pm 0.5)\hat{\sigma}$ ,  $f^{\text{beam}} = 20\%$ , and  $f^{\text{septum}} = 20 \pm 10\%$ . (Right) Experimental data corrected for this systematic using Eqns. 4.29 and 4.30. Raw data points (●) are shown without error bars. Corrected points (○), obscured for the most part underneath the experimental data, are shown with error bars corresponding to the uncertainty of the correction.

atomic signal. Blocking the undesired molecule orders is more difficult than blocking undesired atomic orders due to the molecules' smaller diffraction angle. As before, using 100 nm in place of 200 nm period gratings reduces this systematic error by a factor of  $e^{-4}$ .

### 4.4.3 Attenuation of the Path Traveling Outside the Gas Cell

Our original analysis of the experiment in Section 4.2.3 assumed that the interferometer arm passing outside the filled gas cell (path 2) experiences no phase shift or attenuation. However, a small but unavoidable leakage from the ends of the gas cell means that the both interfering paths undergo some phase shift and attenuation (Figure 4-16a). This leads to a systematic shift in the value of  $\rho_{exp}$  that depends on the ratio of attenuation of the path 2 to path 1.

To estimate the size of this systematic, we repeat the calculations leading to Eqn. 4.19, with the modification:

$$\begin{aligned} a_1 &\rightarrow a_1 e^{(i\hat{\phi} + \hat{\sigma})\eta_1} \\ a_2 &\rightarrow a_2 e^{(i\hat{\phi} + \hat{\sigma})\eta_2} \end{aligned} \quad (4.32)$$

where  $\eta_1$  and  $\eta_2$  are the integrated densities of target-gas atoms along paths 1 and 2. This calculation yields the following fractional shift in  $\rho_{exp}$ :

$$\Delta\rho \approx -2\frac{\eta_2}{\eta_1}, \quad (4.33)$$

where we have assumed  $\eta_2/\eta_1 \ll 1$ .

To estimate the size of this systematic error, we measured the attenuation of a collimated atomic beam on either side of the filled gas cell (see Figure 4-16). We find that  $2\frac{\eta_2}{\eta_1} \approx 2.5 \pm 0.8\%$  for reservoir pressures between 1.6 and 4.6 mTorr (typical of the range of pressures used in the experiment). In Figure 4-17 we have applied this correction to our experimental data.

One way to reduce this systematic error is to redesign the gas cell to direct the

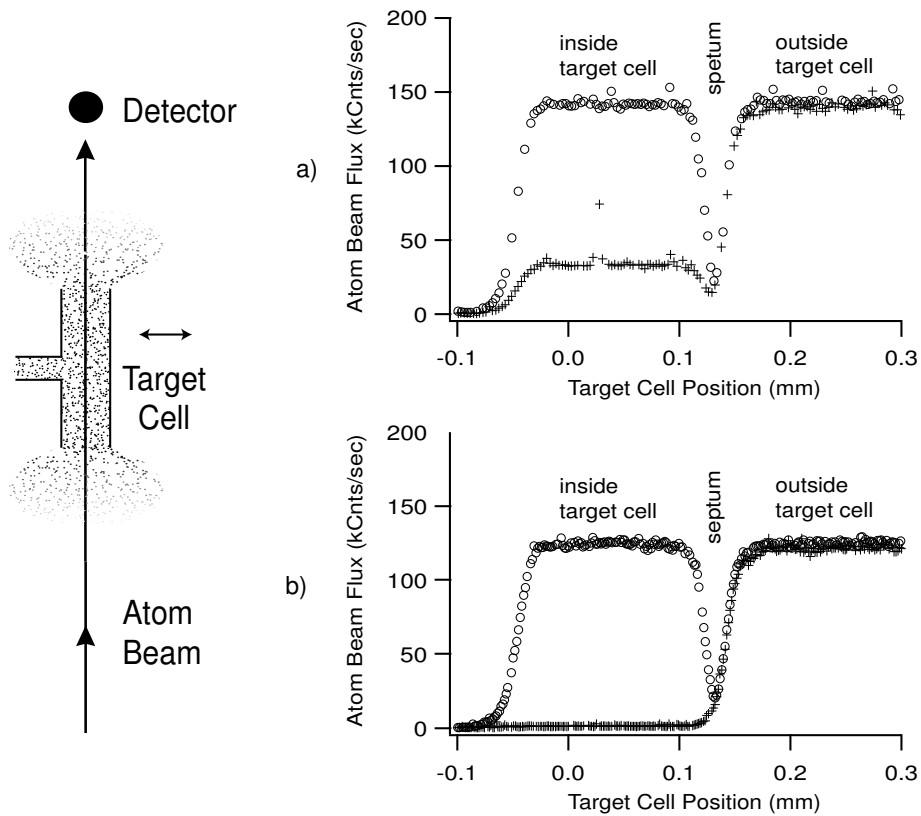


Figure 4-16: (Left) Experimental setup used to measure the attenuation of the atomic beam as it passes the filled gas cell. Atomic flux is monitored as a function of the transverse position of the target cell. (Right) Measurement results showing the difference in attenuation inside versus outside the target cell. The two plots (a,b) are for two different target reservoir pressures: 1.4 mTorr and 4.6 mTorr respectively. There is no significant variation in attenuation with respect to distance from the septum, either inside or outside the target cell.

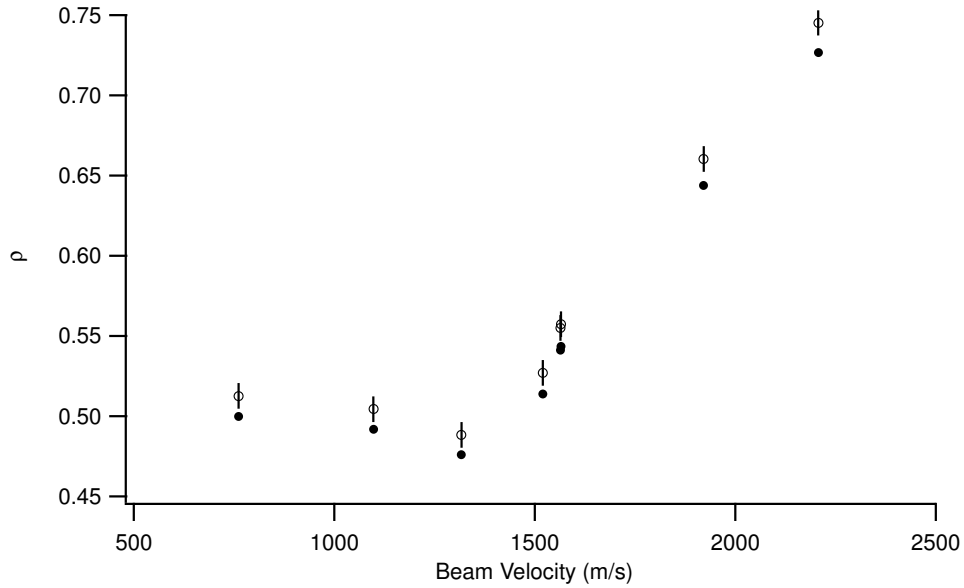


Figure 4-17: Experimental data corrected (using Eqn. 4.29) for the systematic error caused by attenuation of the interfering path which travels outside the target-gas cell. Raw data points (●) are shown without error bars. Corrected points (○) are shown with error bars corresponding to the uncertainty of the correction.

leaking target gas away from path 2. A simpler approach, however, is to make careful measurements of  $\frac{\eta_2}{\eta_1}$  at the reservoir pressures actually used in the experiment and correct the measurements in post-analysis. Collecting just five times as much data (as is plotted in Figure 4-16a,b) at each pressure, it should be possible to correct the data leaving  $\leq 0.1\%$  residual error.

#### 4.4.4 Impure Target Gas

Our original analysis of the experiment in Section 4.2.3 assumed that the gas admitted into the target cell from the target reservoir is 100% pure. However, contaminant gases can be introduced into the target cell via leaks in the vacuum lines connecting either the high-pressure gas cylinder to the target reservoir or the target reservoir to the target cell, or leaks in the pressure reservoir itself. If contaminants are present in the target cell, they will systematically influence the measured amplitude reduction and phase shift of the atom wave passing through it.

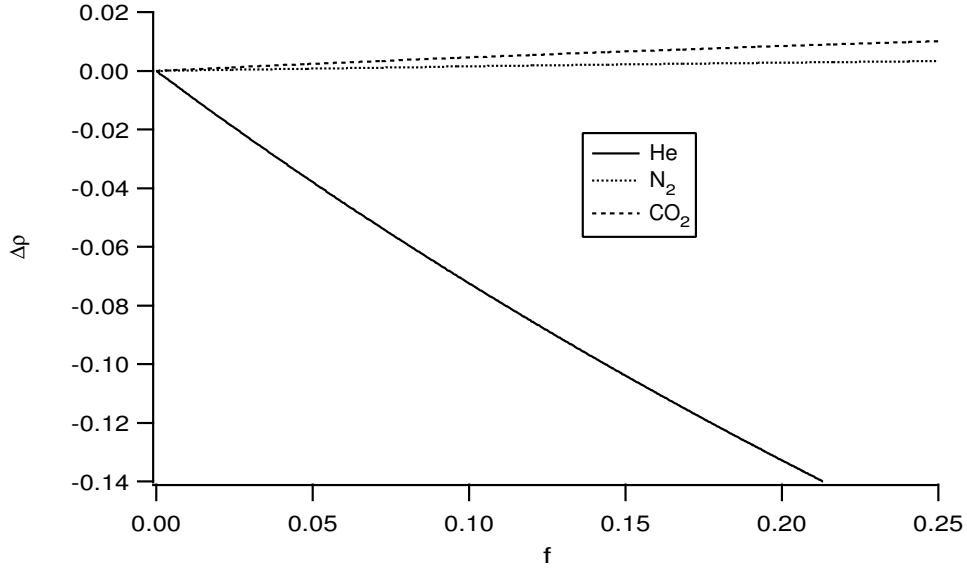


Figure 4-18: Fractional error in  $\rho_{\text{NaAr}}$  due to impure target gas, calculated using Eqn. 4.35 for three different potential impurities. Values of  $\rho_c$  and  $\hat{\sigma}_c$  were obtained from the measurements of Schmeidemeyer et. al. [105], and apply to a sodium beam of velocity 1000 m/s.

To estimate the size of this systematic, we repeat the calculations leading to Eqn. 4.19, with the modification:

$$a_1 \rightarrow a_1 e^{(i\hat{\phi} + \hat{\sigma})\eta} e^{(i\hat{\phi}_c + \hat{\sigma}_c)\eta_c} \quad (4.34)$$

where  $\hat{\phi}_c$ ,  $\hat{\sigma}_c$ , and  $\eta_c$  refer to the dimensionless phase shift, attenuation, and integrated density of the contaminant gas. The resulting fractional shift is given by:

$$\Delta\rho = \frac{\left(\frac{\rho_c}{\rho} - 1\right)}{1 + \frac{\hat{\sigma}_c\eta_c}{\hat{\sigma}\eta}} = \frac{\left(\frac{\rho_c}{\rho} - 1\right) f}{1 + f} \quad (4.35)$$

where the (un)sub-scripted variables refer to the (desired) contaminant gas alone and  $f = \frac{\hat{\sigma}_c\eta_c}{\hat{\sigma}\eta}$  is the ratio of the attenuation due to the contaminant gas versus the desired gas.

In Figure 4-18 we plot  $\Delta\rho$  as a function of fractional contaminant density,  $f$ , for three different possible contaminants. This plot is only a rough estimate of the error

because variation in  $\rho_c$  with respect to atom beam velocity has not been considered.

For a properly functioning gas handling system, the value of  $f$  should be  $\leq 0.1$ . However, after having collected most of our sodium-argon index data, we became aware of a leak in our gas handling system that had been contaminating our argon target gas. We noticed the leak when we measured a non-zero phase shift and attenuation of the atom interference fringes with a nominally “empty” target reservoir. Using Eqn. 4.35 we have investigated what effect this impurity had on our measurements of  $\rho_{\text{NaAr}}$ .

Because nitrogen represents the most abundant component (78%) of the air that was leaking into the target reservoir, to determine  $\rho_c$  and  $\hat{\sigma}_c$  we measured the velocity dependent sodium-nitrogen index. This measurement will be reported in more detail in a future thesis (the preliminary results are plotted in Figure 4-19). For each affected measurement of  $\rho_{\text{NaAr}}$ , we then determined  $f$  (which ranged between 0.05 and 0.17 depending on the experimental conditions) from a combination of the sodium-argon and sodium-nitrogen index measurements and the measured attenuation with the “empty” reservoir.

We calculated a correction to our measured values of  $\rho_{\text{NaAr}}$  using Eqn. 4.35. The results, plotted in Figure 4-19, indicate that our sodium-argon index measurements had been pulled in the direction of the sodium-nitrogen index. In these calculations we have assumed that the leak rate was the same for all of the affected data (collected on 3 separate evenings). Therefore, the error in the correction is due equally to our uncertainty in  $\rho_c$  and  $\hat{\sigma}_c$ , and our uncertainty in the value of  $f$  — we do not know whether the magnitude of the leak was the same for all of the affected data.

In the future, care should be taken that no impurities are compromising the desired index measurement. The best way to ensure this is to collect data as if to measure the index of refraction, but without deliberately leaking any target gas into the reservoir. If a phase shift/attenuation is observed, the system should be checked for leaks.

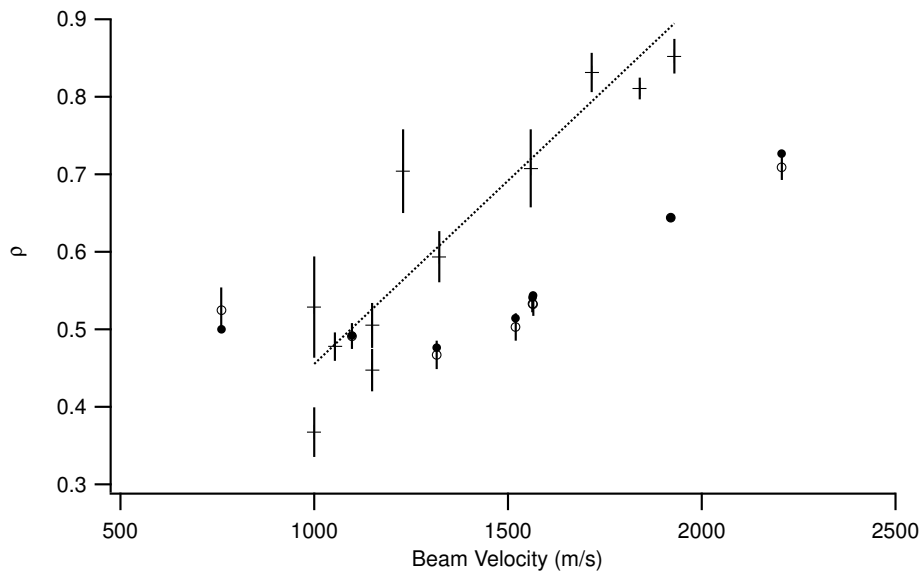


Figure 4-19: Effect of a nitrogen impurity (caused by a leak in the gas lines leading to the target-gas cell) on our measurements of  $\rho_{\text{NaAr}}$ . The dashed line is a simple linear fit to the sodium-nitrogen index measurements (+). Our raw experimental measurements of  $\rho_{\text{NaAr}}$  ( $\bullet$ ) are shown without error bars. The open circles ( $\circ$ ) are corrected values of  $\rho_{\text{NaAr}}$  using Eqn. 4.35, shown with error bars corresponding to the uncertainty in the correction. The measurement at  $v \approx 1900$  m/s is not corrected because the leak had been fixed before this data point was taken.

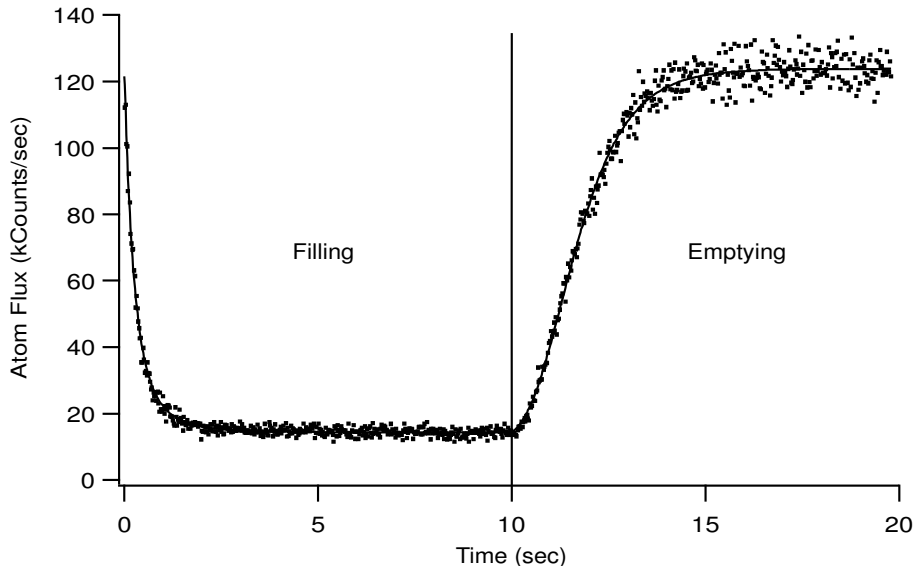


Figure 4-20: Measurement of the atomic flux transmitted through the target cell while the cell is filled/emptied. Filling of the initially empty cell begins at  $t = 0$  and emptying begins at  $t = 10$  s. From this data, we determined the filling and emptying time constants to be  $1.10 \pm 0.04$  s and  $0.91 \pm 0.01$  s, respectively.

#### 4.4.5 Gas Cell Filling/Emptying

Our original analysis of the experiment assumed that the density of gas within the target cell,  $\eta$ , does not vary as a function of time. In reality, when switching between the gas-on and gas-off configurations, the density of gas in the cell approaches equilibrium exponentially in time:

$$\eta(t) = \begin{cases} \eta_0 e^{-t/\tau_e} & \text{Emptying} \\ \eta_0 [1 - e^{-t/\tau_f}] & \text{Filling,} \end{cases} \quad (4.36)$$

where  $\tau_{e,f} \approx 1$  s are the emptying and filling time constants for our gas cell, measured by monitoring the attenuation of a raw atomic beam (no gratings in place) as the gas cell was filled/emptied (See Figure 4-20). Because  $\eta$  is time-dependent, both the gas-on and gas-off interference patterns are in fact averages over a pattern that is changing in time as the pressure changes in the cell. Thus, the measure values of  $\phi_{exp}$  and  $\sigma_{exp}$  are not correctly predicted by Eqn. 4.19.

One solution to this problem is to discard any data taken within a “waiting” time,  $\Delta t$ , equal to a few filling/emptying time constants, after opening/closing the target-gas valves. This was not practical in the previous velocity-dependent experiment [54] because the filling time constant was so long. In the current experiment a typical cycle of on/off data was collected in 16 seconds: integrating for a time interval  $T_{fill} = 8$  seconds in the gas-on configuration, and another  $T_{empty} = 8$  seconds in the gas-off configuration. The first three to four time-constants worth of data collected after switching between configurations were then discarded.

It is still important to check whether the approach to equilibrium is biasing our measurement of  $\rho_{\text{NaAr}}$ . Unlike the previous systematic effects considered, there is no simple analytic expression for  $\Delta\rho$ . However, we can estimate the effect of the time averaging on our measurements using the algorithm below:

1. Obtain from the measured gas-on and gas-off interference patterns, nominal values for phase, contrast, and mean count rate.
2. Using Eqns 4.14, 4.18, 4.36, and the nominal values from the previous step we determine the time-dependent contrast  $C(t)$ , phase  $\phi(t)$ , and mean count rate  $I_0(t)$ .
3. Calculate an averaged contrast  $\bar{C}$ , and phase,  $\bar{\phi}$ , that excludes data collected during the “waiting” time:

$$\bar{C}e^{i\bar{\phi}} = \frac{\int_{\Delta t}^{T_{fill,empty}} I_0(t) C(t) e^{i\phi(t)} dt}{\int_{\Delta t}^{T_{fill,empty}} I_0(t)}. \quad (4.37)$$

4. Calculate  $\rho_{avg}$  using the averaged contrast and phase, and  $\rho_{raw}$  from the raw (unaveraged) measured contrast and phase measurements.
5. Estimate  $\Delta\rho$  as  $(\rho_{avg} - \rho_{raw})/\rho_{raw}$ .

We have performed this analysis using typical values from one of our datasets measuring of  $\rho_{\text{NaAr}}$  at  $v = 2207$  m/s (gas-on:  $I_0 = 7.5$  kCounts/sec,  $C = 12.2\%$ ,  $\phi = 1.21$  rad; gas-off:  $I_0 = 39.5$  kCounts/sec,  $C = 13.1\%$ ,  $\phi = 0$  rad). The results

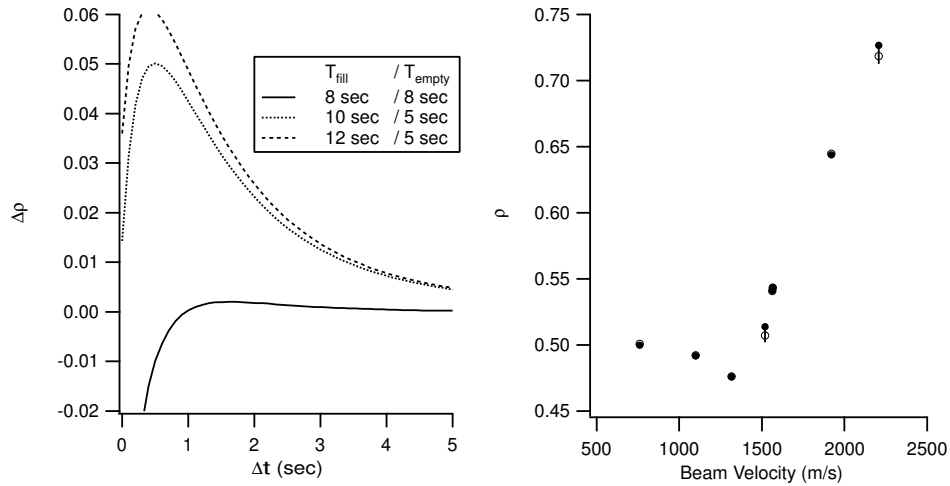


Figure 4-21: (Left) Calculation of the systematic shift caused by collecting data before the pressure in the target-gas cell has reached equilibrium. Each trace assumes the gas-on/gas-off integration times  $T_{fill}/T_{empty}$  indicated, and is plotted as a function of the “waiting” time interval  $\Delta t$  after switching between configurations during which the interference data was discarded. (Right) Experimental data corrected for this systematic using the procedure for estimating  $\Delta\rho$  described above. Raw data points (●) are shown without error bars. Corrected points (○) are shown with error bars corresponding to the uncertainty of the correction.

are displayed on the left hand side of Figure 4-21 which shows the variation in  $\Delta\rho$  as a function of the waiting time,  $\Delta t$ , for three different pairs of values for  $T_{fill}/T_{empty}$ . The error is large ( $> 5\%$ ) if  $\delta t = 0$ , but quickly drops to  $\leq 1\%$  for  $\Delta t$  a few time constants long. The error is less significant for longer integration times.

We calculated a correction to our measured values of  $\rho_{NaAr}$  using the procedure for estimating  $\Delta\rho$  described above. The results are plotted on the right hand side of Figure 4-21. The correction is largest for our measurements at  $v = 2207$  m/s and  $v = 1520$  m/s because for these velocities  $T_{fill}$  was only 5 seconds (versus 8 seconds for most of our datasets).

#### 4.4.6 Summary of Systematics

In this section we have examined five different sources of systematic error and estimated their effect on our new measurements of  $\rho_{NaAr}$ . In Figure 4-22 is displayed

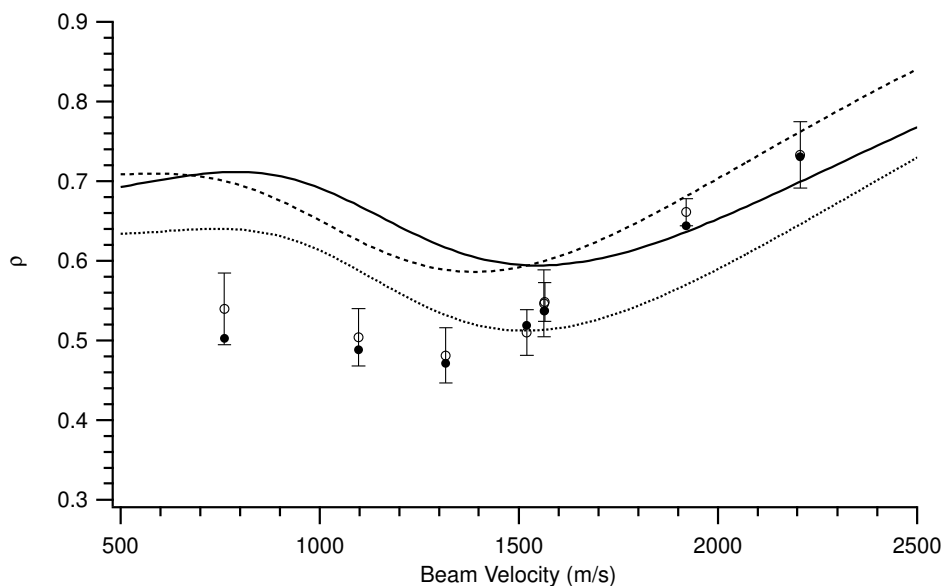


Figure 4-22: Measurements of  $\rho_{\text{NaAr}}$  corrected for the five systematic errors discussed in this section. Raw data points (●) are shown without error bars. Corrected points (○) are shown with error bars combining the statistical uncertainty plus the uncertainty of the systematic corrections. Also shown are the same three theoretical predictions that appear in Figure 4-11.

the combined effect of these systematics on the experimental data. Compared to the raw data, the corrected data are more consistent, though still not in complete agreement, with the theoretical predictions shown. The error in the corrected data includes uncertainties in the applied corrections as well as the statistical error in the raw data.

Table 4.2 lists the approximate magnitude, direction, and uncertainty of each systematic error we have considered. The largest systematic shift was due to the impure target gas, an effect easily eliminated by fixing any leaks in the gas handling system. We have also discussed straightforward techniques for significantly reducing the error due to: other interfering orders (use 100 nm gratings), molecules (use 100 nm gratings), and gas cell filling/emptying (use appropriate delay interval). While no remedy short of a gas-cell redesign presents itself for the remaining systematic, attenuation outside the gas cell, careful measurements of the attenuation as a function of target-cell pressure should allow the appropriate correction to be calculated to

	$\Delta\rho$ (200 nm gratings)	$\Delta\rho$ (100 nm gratings)
Other interfering orders	$-2 \pm 1\%$	$< 0.1\%$
Molecules	$-1 \pm 3\%$	$0 \pm 0.1\%$
Attenuation	$-2.5 \pm 0.8\%$	same
Impure target gas	$-5 \pm 3\%$	same
Target-gas cell filling/emptying	$1 \pm 0.5\%$	same

Table 4.2: Magnitude, direction (positive or negative), and uncertainty of  $\Delta\rho$  for the five systematic effects considered in this section. The two systematics related to detection of undesired atomic/molecular interfering orders can be significantly reduced using 100 nm instead of 200 nm atom diffraction gratings.

roughly 0.1%.

## 4.5 Future Prospects

Atom interferometry is becoming a standard tool for precision studies of interatomic potentials. In the long term, interferometry with Bose-Einstein condensates combined with techniques for coherent amplification of matter waves [56, 68] hold promise for significantly improved measurements of the matter-wave index of refraction, at least for small collision velocities. Continuing work in our own group on the matter-wave index of refraction will focus on eliminating the newly identified sources of systematic error, and making a convincing observation of glory oscillations.

To observe glory oscillations, two approaches are being considered: cooling the target gas and using target gases other than argon. As suggested by Hammond [54], cooling the gas cell reduces both the average and the spread in velocity of the target gas, so that more of the glory structure remains after the average over collision velocity. The theoretical prediction for  $\rho_{\text{NaAr}}$  with a liquid nitrogen cooled target gas is shown in Figure 4-23. Also shown are theoretical predictions for  $\rho_{\text{NaKr}}$  or  $\rho_{\text{NaXe}}$ . The glory oscillations have larger period in these systems than in  $\rho_{\text{NaAr}}$ , and because the target atoms are more massive, they have a reduced velocity and reduced velocity spread compared to argon at the same temperature. These two factors result in larger amplitude glory oscillations than are predicted for a room-temperature argon target.

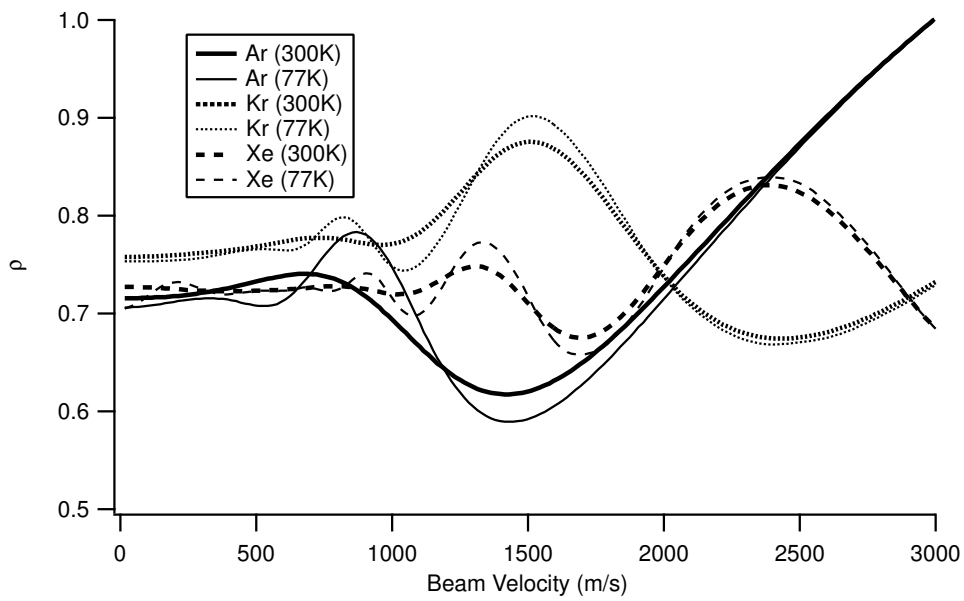


Figure 4-23: Theoretically predicted  $\rho$  versus velocity (based on potential models taken from [22]) for the sodium-argon, sodium-krypton, and sodium-xenon systems. Two traces are shown for each atomic pair, one assuming a room temperature target gas, the other assuming a liquid nitrogen cooled (77K) target gas. Using liquid nitrogen cooling or studying one of the heavier noble gases are two directions under consideration for observing glory oscillations.

# Appendix A

## Diffraction of Sodium Atoms through a Nanofabricated Grating

### A.1 Introduction

The diffraction of sodium atoms through a single nanofabricated grating provides a powerful diagnostic both of our atomic beam as well as the quality and characteristics of the diffraction gratings themselves. In order to extract this information, we have developed a theoretical model for the diffraction pattern which we fit to experimental measurements. This appendix summarizes our current model, which has been improved over the past few years to better account for variations in grating open fraction and for the shape of the diffraction peaks.

### A.2 Physical Model

#### A.2.1 Multiple Slit Diffraction

We begin with the well known expression for the far-field intensity of a normally incident matter-wave (wave-vector  $k \equiv 2\pi/\lambda_{dB}$ ) coherently illuminating  $N$  evenly spaced slits of period  $a$  and width  $b$ :

$$\frac{I(\theta)}{I(0)} = \frac{\sin^2 \beta \sin^2 N\alpha}{\beta^2 \sin^2 \alpha} \quad (\text{A.1})$$

where  $\alpha = \frac{ka}{2} \sin \theta$  and  $\beta = \frac{kb}{2} \sin \theta$ . In our experiment, the period of the slits (1-200 nm) is much smaller than the width of the atomic beam ( $\approx 100 \mu\text{m}$ ), implying that the number of coherently illuminated slits is very large ( $N \approx 1000$ ). In this limit, the second factor in Eqn. A.1 is effectively a delta-function which fires when  $\alpha = n\pi$  or  $\sin \theta_n = n\lambda_{dB}/a$ . Substituting this condition into Eqn. A.1, we obtain the expression:

$$\frac{I_n}{I_0} = \frac{\sin^2(n\pi f)}{(n\pi f)^2}. \quad (\text{A.2})$$

where  $f \equiv \frac{b}{a}$  is the open fraction of the grating. The intensity of the zeroth order,  $I_0$  is proportional to  $f^2$ .

### A.2.2 Variable Open Fraction

A obvious complication we must consider is that the gratings we use are not perfect. In particular, their open fraction may not be uniform over the entire area of the grating illuminated by the atomic beam. To model this variation, we assume a Gaussian distribution of open fractions (mean value  $f_0$ , rms width  $\sigma_f$ ) and average the simple multiple slit pattern (Eqn. A.2) over this distribution to obtain:

$$\frac{I_n}{I_0} = e^{-(n\pi\sigma_f)^2} \frac{\sin^2(n\pi f)}{(n\pi f)^2}. \quad (\text{A.3})$$

This expression indicates that the effect of open fraction variations is to suppress higher-order diffraction peaks.

A grating whose distribution of open fractions is symmetric about some mean value transmits the same total flux of atoms as a grating with a perfectly uniform open fraction. Therefore, it is necessary to account for the matter-wave amplitude “missing” from the higher diffracted orders. Grisenti et. al. [48] have shown that this missing amplitude appears as a broad incoherent peak which can be modeled as a

Gaussian. The intensity  $I_{inc}$  and width  $\sigma_{inc}$  of this incoherent peak can be calculated, but for simplicity we have chosen simply to leave them as free parameters in our fitting routine.

### A.2.3 Velocity Distribution and Collimation

For  $N \rightarrow \infty$  and a monochromatic matter-wave, we expect the diffracted peaks to be infinitely narrow. In practice, the ensemble of atoms in our beam is not monochromatic (typical rms velocity width  $\sigma_v/v_0 = 5\%$ ) nor is the beam a pure longitudinal plane wave (typical undiffracted beam width at the detector is  $30 - 60 \mu\text{m}$ ). We incorporate these effects into our model by assuming a spread in diffraction angle:

$$\sigma_{\theta_n} = \sqrt{\sigma_0^2 + \sigma_n^2} \quad (\text{A.4})$$

where  $\sigma_0$  is the angular width of the undiffracted beam and  $\sigma_n$  represents the additional angular broadening of the  $n$ th diffracted order due to our finite velocity distribution. We model the angular shape of each diffraction peak  $S_n(\theta)$  using this angular spread:

$$S_n(\theta) = \frac{1}{\sqrt{2\pi\sigma_{\theta_n}^2}} e^{-\frac{(\theta - \theta_n(v_0))^2}{2\sigma_{\theta_n}^2}}. \quad (\text{A.5})$$

The parameter  $\sigma_n$  is given by:

$$\sigma_n^2 = \int dv f(v) [\theta_n(v) - \theta_n(v_0)]^2, \quad (\text{A.6})$$

where  $\theta_n(v)$  is the  $n$ th order diffraction angle for a plane wave of velocity  $v$ . Assuming a gaussian velocity distribution of atoms in our beam (mean  $v_0$ , rms width  $\sigma_v$ ) we find:

$$\sigma_n^2 = \frac{L^2}{\sqrt{2\pi\sigma_v^2}} \int dv e^{-\frac{(v-v_0)^2}{2\sigma_v^2}} \left( \sin^{-1}(\theta_n(v_0) \frac{v_0}{v}) - \sin^{-1}(\theta_n(v_0)) \right)^2. \quad (\text{A.7})$$

where  $\theta_n(v_0) = \frac{n\lambda_{db}^0}{a}$ , and  $\lambda_{db}^0 \equiv \frac{h}{mv_0}$  is the mean deBroglie wavelength. Because  $\lambda_{db}^0 \ll a$ , it is valid to use the small angle approximation in integrating Eqn. A.7, with the result:

$$\sigma_n^2 = \theta_n^2(v_0) \left[ \left( \frac{\sigma_v}{v_0} \right)^2 + 9 \left( \frac{\sigma_v}{v_0} \right)^4 + O \left( \frac{\sigma_v}{v_0} \right)^6 \right]. \quad (\text{A.8})$$

#### A.2.4 Detection Geometry

Before we can combine the two previous sections into a single formula for the atomic diffraction pattern, we must consider the effect of our detector geometry on the measurement. The first observation is that atomic flux is measured as a function of transverse position,  $x = L \sin^{-1} \theta$ , where  $L$  is the longitudinal distance from grating to detector. Because  $\theta \ll 1$ , we can substitute  $\theta \approx x/L$  in Eqns. A.8 and A.5:

$$\begin{aligned} S_n(x) &= \frac{1}{\sqrt{2\pi\sigma_{x_n}^2}} e^{-\frac{(x-x_n)^2}{2\sigma_{x_n}^2}} \\ \sigma_{x_n} &= L\sqrt{\sigma_0^2 + \sigma_n^2}. \end{aligned} \quad (\text{A.9})$$

where  $x_n = L\theta_n(v_0)$  is the mean position of the  $n$ th order diffracted peak.

Finally, our detector is not infinitely narrow, it has a half width  $w$  of roughly 25  $\mu\text{m}$ . A measurement of atomic flux taken with the detector centered at some position  $x$  is actually an average over a portion of the diffraction pattern. To account for this, we average our shape function  $S_n(x)$  over the detector width:

$$\begin{aligned} S'_n(x) &= \frac{1}{\sqrt{2\pi\sigma_{x_n}^2}} \int_{x-w}^{x+w} dx' e^{-\frac{(x'-x_n)^2}{2\sigma_{x_n}^2}} \\ &= \frac{1}{2} \left[ \text{Erf} \left( \frac{w + (x - x_n)}{\sqrt{2}\sigma_{x_n}} \right) + \text{Erf} \left( \frac{w - (x - x_n)}{\sqrt{2}\sigma_{x_n}} \right) \right]. \end{aligned} \quad (\text{A.10})$$

### A.2.5 Molecules

For typical source conditions, our “atomic” beam is actual comprised of 10%-30% sodium molecules. Because our gratings are not species selective, the measured diffraction pattern is a sum of contributions from atoms and molecules. The molecules have nominally the same velocity distribution as the atoms, and (being twice as massive) have half the atom’s deBroglie wavelength. All of the analysis presented above is the same for atoms and molecules, so the molecules can be included in our model simply by introducing the molecule fraction,  $m_f$  as an additional parameter.

### A.2.6 Background

A final contribution to our model of the measured diffraction pattern is a constant,  $b$ , representing the background counting rate of our detector (i.e. the counting rate when the atom beam is blocked). The background arises from the ionization of background gas particles on our hot-wire.

## A.3 Synthesis

Bringing together the analysis above, we have a single expression for the expected diffraction pattern (atomic intensity versus position):

$$I(x) = b + \frac{I_{inc}}{\sqrt{2\pi\sigma_{inc}^2}} e^{-\left(\frac{x}{\sigma_{inc}}\right)^2} + (1 - m_f) \left[ \sum_n I_n S'_n(x) \right]_{Na} + m_f \left[ \sum_n I_n S'_n(x) \right]_{Na_2} \quad (\text{A.11})$$

This expression is routinely used to fit measured diffraction patterns and extract parameters of the atom/molecule beam ( $v_0$ ,  $\sigma_v$ ,  $m_f$ ) and diffraction gratings ( $f$ ,  $\sigma_f$ ).

## A.4 Effect of Atom-Wall Interactions

We note that the potentially important van der Waals and Casimir interactions between the atoms/molecules in the beam and the grating walls have not been included in this analysis. Grisenti et. al. [47] have studied the effects of van der Waals attraction between atoms and grating bars on matter-wave diffraction patterns. They find that the primary effect of such interactions is to reduce the effective open fraction of the grating.

The derivation in Ref. [47] is based on an atom-wall potential of the form  $V(x, z) = \frac{C_3}{r_\perp^3}$ . Using the eikonal approximation to calculate the phase shift as a function of transverse position, they arrived at a complex valued amplitude-transmission function which they Fourier transform to obtain the far field intensity distribution:

$$\frac{I_n}{I_0} = \frac{e^{-(2\pi\frac{\sigma}{d})^2}}{\left(\frac{\pi n|s|}{d}\right)^2} \left[ \sin^2\left(\frac{\pi n s_r}{d}\right) + \sinh^2\left(\frac{\pi n s_i}{d}\right) \right], \quad (\text{A.12})$$

where  $s = s_r + i s_i$  is a complex slit width related to  $C_3$ .

By measuring experimentally the change in apparent open fraction as a function of atom beam velocity, the authors were able to see evidence of the van der Waals interaction in matter-wave diffraction through 100 nm gratings (fabricated by the same group at MIT from whom we obtain our own 100 nm gratings).

## Appendix B

**Paper: From Single to  
Multiple-Photon Decoherence in  
an Atom Interferometer**

# PHYSICAL REVIEW LETTERS

VOLUME 86

12 MARCH 2001

NUMBER 11

## From Single- to Multiple-Photon Decoherence in an Atom Interferometer

David A. Kokorowski, Alexander D. Cronin, Tony D. Roberts, and David E. Pritchard

*Massachusetts Institute of Technology, Cambridge, Massachusetts 02139*

(Received 23 August 2000)

We measure the decoherence of a spatially separated atomic superposition due to spontaneous photon scattering. We observe a qualitative change in decoherence versus separation as the number of scattered photons increases, and verify quantitatively the decoherence rate constant in the many-photon limit. Our results illustrate an evolution of decoherence consistent with general models developed for a broad class of decoherence phenomena.

DOI: 10.1103/PhysRevLett.86.2191

PACS numbers: 03.65.Ud, 03.75.Dg, 42.50.Ar

Decoherence is the result of entanglement between a quantum system and an unobserved environment, and manifests as the reduction of coherent superpositions into incoherent mixtures. This reduction occurs more quickly as the number of particles comprising a quantum system increases, establishing decoherence as a fundamental limit to large-scale quantum computation [1] and communication [2]. Progress in these fields therefore relies upon understanding and correcting for decoherence effects. On a macroscopic scale, decoherence is unavoidable and explains the emergence of classical behavior in a world governed by quantum mechanical laws.

Theoretical treatments of decoherence provide a description for the evolution of a system's density matrix under the influence of a specific environment. For spatial decoherence, various environments including a thermal bath of harmonic oscillators [3], a scalar field [4], and an isotropic distribution of scatterers [5,6] have been studied. In the high-temperature or many scatterer limit, these models all yield a diffusionlike master equation for the system's spatial density matrix,  $\rho(x, x')$ :

$$\frac{d\rho}{dt} = -\frac{i}{\hbar}[H, \rho] - D^2|x - x'|^2\rho, \quad (1)$$

where  $H$  is the Hamiltonian for the isolated system and  $D$ , the diffusion constant, depends on the details of the system-environment coupling. Assuming negligible internal dynamics, this equation predicts an exponential reduction in coherence with time and with separation squared [7]:

$$\rho(x, x', t) = e^{-D^2|x-x'|^2 t} \rho(x, x', 0). \quad (2)$$

Similar decoherence behavior arises and has been studied in the context of an atom interacting with a high- $Q$  cavity [8] and trapped ions interacting with a fluctuating electric field [9].

To investigate the distinct case of decoherence due to scattering processes, we have studied the loss of spatial coherence of atoms within an atom interferometer due to spontaneous scattering of photons. In the many-photon limit, this represents a simple case of the general models above; we observe coherence loss consistent with Eq. (2) and are able to derive the decay constant from first principles. The few-photon limit is of a qualitatively different character, and we have followed the smooth transition between these two regimes.

The atom interferometer [10] is realized by passing a collimated, supersonic beam of Na atoms (velocity  $\approx 3000$  m/s using a He carrier gas) through three diffraction gratings arranged in the Mach-Zehnder geometry (Fig. 1). Prior to the first grating, the atoms are collimated and optically pumped into the  $^3S_{1/2}|F=2, m_f=+2\rangle$  ground state. Two paths through the interferometer, separated by up to  $20 \mu\text{m}$ , overlap at the position of the third grating, forming a spatial interference pattern. This pattern is masked by the third grating and the total transmitted flux is detected using a  $50 \mu\text{m}$  hot wire. The interference pattern is measured as an oscillating atomic flux versus grating position. Because the contrast of the interference pattern is

0031-9007/01/86(11)/2191(5)\$15.00

© 2001 The American Physical Society

2191

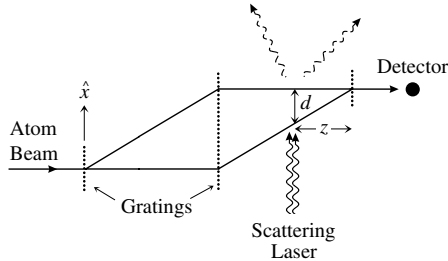


FIG. 1. A schematic of our apparatus: A Mach-Zehnder interferometer composed of three, evenly spaced, transmission gratings. Within the interferometer, sodium atoms continuously absorb and spontaneously emit photons from a variable intensity laser beam. Decoherence due to spontaneous emission results in reduced contrast interference fringes.

proportional to the coherence between the two paths, reduction in contrast is direct evidence of coherence loss.

The effective decohering environment consists of photons from a laser beam directed along the  $\hat{x}$  axis which intersects both interfering paths. The circularly polarized laser light is tuned to the  ${}^3S_{1/2}[2, +2] \rightarrow {}^3P_{3/2}[3, +3]$  transition with wavelength  $\lambda = 2\pi/k_0 = 590$  nm. Because the atoms are dipole forbidden from decaying to any state other than  ${}^3S_{1/2}[2, +2]$ , they can continuously scatter photons without falling out of resonance (the natural linewidth is  $\sim 200$  photon recoils wide).

At the intersection of the atomic beam and scattering laser, each atom's transverse wave function is peaked at two positions which we label  $x$  and  $x + d$ . If a photon, initially in momentum state  $|k_0\rangle$ , scatters from this atom, the two become entangled:

$$|\psi\rangle_i = (|x\rangle + |x + d\rangle) \otimes |k_0\rangle \xrightarrow{\text{scat.}} |x\rangle \otimes |\phi_x\rangle + |x + d\rangle \otimes e^{ik_0d} |\phi_{x+d}\rangle, \quad (3)$$

where  $|\phi_x\rangle$  is the wave function of a photon spontaneously emitted from position  $x$  and the factor  $e^{ik_0d}$  accounts for the difference in spatial phase of the initial photon at the two positions. Generalizing the entangled wave function in Eq. (3) to a density matrix and tracing over a basis of scattered photon states, the net effect of scattering on the atom's spatial density matrix is

$$\rho(x, x + d) \xrightarrow{\text{scat.}} \rho(x, x + d)\beta(d), \quad (4)$$

where  $\beta(d)$  is known as the decoherence function and has the properties  $|\beta(d)| \leq 1$  and  $\beta(0) = 1$ . The decoherence function thus defined is equal to the inner product of the two final photon states, which are identical apart from an overall translation:

$$\begin{aligned} \beta(d) &= e^{ik_0d} \langle \phi_x | \phi_{x+d} \rangle = e^{ik_0d} \langle \phi_x | e^{-ik_x d} | \phi_x \rangle \\ &= \int d\Delta k P(\Delta k) e^{-i\Delta k d}, \end{aligned} \quad (5)$$

where the operator  $\hat{k}_x$  is the generator of photon translations along the  $\hat{x}$  axis. The resulting decoherence function is the Fourier transform of a probability distribution  $P(\Delta k)$ , with  $\Delta k = k_x - k_0$  being the change in momentum of the photon along the  $\hat{x}$  axis.

Previous experiments [11,12] have measured the decoherence function for an atom which spontaneously scatters a single photon. The theoretical prediction which these experiments confirm is displayed as the solid line in Fig. 2. Beneath an overall decay in coherence with distance, periodic coherence revivals are observed. This shape follows directly from the Fourier transform of the dipole radiation pattern for spontaneous emission. It has also been explained in terms of the ability of a single photon to provide which-path information [12]: the contrast drops to zero when the path separation is approximately equal to the resolving power of an ideal Heisenberg microscope  $d \approx \lambda/2$ , with revivals resulting from path ambiguity due to diffraction structure in the image.

If several photons are scattered, and if successive scattering events are independent, the total decoherence function includes one factor of  $\beta$  for each scattered photon:

$$\beta_{\text{total}}(d) = \sum_{n=0}^{\infty} P(n)\beta^n(d). \quad (6)$$

In our experiment, the total number of photons scattered by an individual atom is intrinsically uncertain, but is described by the distribution  $P(n)$  which can be measured or calculated. The sum in Eq. (6) is a trace over this additional degree of freedom of the environment.

Figure 2 shows measurements of the decoherence function for laser intensities corresponding to an average number of scattered photons,  $\bar{n}$ , ranging from  $\sim 1$  to  $\sim 8$ . At each intensity, a reference contrast and phase was measured, with the scattering laser positioned such that the interfering paths were completely overlapped ( $d = 0$ ). We then adjusted the longitudinal position of the scattering

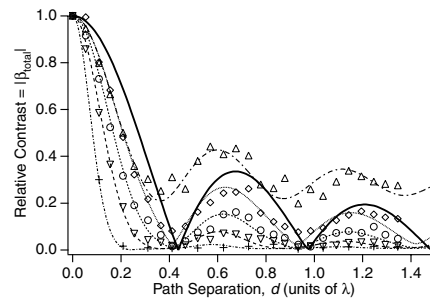


FIG. 2. The total decoherence function,  $|\beta_{\text{total}}|$ , measured as the normalized contrast after spontaneous photon scattering. The solid line is the single-photon decoherence function. Also displayed are the best fits from which we determine  $\bar{n} = 0.9$  ( $\Delta$ ), 1.4 ( $\diamond$ ), 1.8 ( $\circ$ ), 2.6 ( $\nabla$ ), and 8.2 ( $+$ ).

laser,  $z$ , to select specific path separations in the range  $0 < d < 1.4\lambda$  at which to measure the decoherence function (see Fig. 1). For each path separation, the ratio of the measured atom interference contrast to the reference contrast yields the magnitude of the decoherence function,  $|\beta_{\text{total}}(d)|$ . The difference between the measured atom interference phase and the reference phase yields the phase of the decoherence function.

We fit the data using Eq. (6) and taking  $P(n) \approx \exp[-\frac{1}{2}(n - \bar{n})^2/\sigma_n^2]$ . This form was chosen as a good approximation to Monte Carlo wave function calculations of  $P(n)$  for our laser parameters. From the best fit curves displayed in Fig. 2, values were extracted for  $\bar{n}$  and  $\sigma_n$  which were consistent with, and more accurate than, independent measurements of  $P(n)$  based on the deflection and broadening of the atomic beam with the scattering laser blocked versus unblocked.

In the regime  $d \gg \lambda$ , a single scattered photon suffices to completely destroy the coherence between paths. Thus, the nonzero asymptotic value (for  $\bar{n} = 0.9$  in Fig. 2) of the decoherence function at large path separation is equal to the fraction of atoms which scatter zero photons (i.e., decoherence is proportional to the atom-photon scattering cross section). This phenomenon is a simple example of saturation of decoherence [6,13]: the loss of coherence becomes independent of path separation at a characteristic length scale of the environment. A recent experiment by Cheng and Raymer [14], involving loss of optical coherence due to a disordered collection of polystyrene microspheres, has features similar to our own: contrast loss was observed to saturate when the path separation reached roughly the diameter of the microspheres, and the asymptotic contrast was proportional to the microsphere-light scattering cross section.

As the average number of scattered photons increases, the overall amount of decoherence increases, and the contrast revivals disappear. This behavior can be formalized as the Fourier transform of the total momentum distribution of all scattered photons:

$$\beta^n(d) = \int d\Delta K P(\Delta K) e^{i\Delta K d}, \quad (7)$$

where  $\Delta K = \sum_{i=1}^n \Delta k_i$ . As  $n \rightarrow \infty$ , the central limit theorem predicts that  $P(\Delta K)$  will tend towards a Gaussian with mean  $n k_0$  and variance  $n \sigma_k^2$  (where  $\sigma_k = \frac{2}{3} k_0$  is the rms transverse momentum of an emitted photon). In the case of spontaneous emission,  $P(\Delta K)$  is approximately Gaussian for  $n > 3$  and the decoherence function reduces to

$$\begin{aligned} \beta^n(d) &= \int d\Delta K [e^{-(1/2)(\Delta K - n k_0)^2 / n \sigma_k^2}] e^{i\Delta K d} \\ &= e^{-(1/2)n \sigma_k^2 d^2} e^{-i n k_0 d}. \end{aligned} \quad (8)$$

Inserting this expression into Eq. (6) and taking  $d/\lambda \ll 1$ , we find

$$\lim_{\bar{n} \rightarrow \infty} \beta_{\text{total}}(d) = e^{-(1/2)\kappa^2 d^2} e^{-i \bar{n} k_0 d}, \quad (9)$$

where

$$\kappa^2 = \bar{n} \sigma_k^2 + \sigma_n^2 k_0^2 \quad (10)$$

is the variance of the total momentum transferred to the atom from the scattered photons. The first term in Eq. (10) comes from the trace over modes available to the spontaneously emitted photon, while the second is related to the uncertainty in number of absorbed photons combined with the fixed phase  $k_0 d$  imparted by each.

If  $\sigma_n = \sqrt{\bar{n}}$  (i.e., Poissonian statistics), Eq. (9) predicts an exponential decay in contrast with number of scattered photons ( $\kappa^2 \propto \bar{n}$ ). If in addition the scattering rate,  $\Gamma$ , is constant, then  $\bar{n} = \Gamma t$  and the decoherence has exactly the exponential form derived from a master equation like Eq. (1).

We have measured this exponential reduction of spatial coherence by varying the average number of scattered photons, leaving the path separation fixed (Fig. 3). Theory curves (solid lines) are based on Eq. (9) with  $\sigma_n$  determined from the broadening of the atomic beam due to the momentum of the scattered photons. The product of the two remaining free parameters,  $\bar{n} d$ , was obtained from the measured phase of the decoherence function.

The data follow a nearly exponential decay with  $\bar{n}$ . The upward trend at large  $\bar{n}$  is a result of the finite size of our hot-wire detector: the trace over final photon states [Eq. (8)] must be restricted to those states which allow the atom to reach the detector. As a result  $\kappa$  in Eq. (9) is replaced with  $\kappa'$  where  $1/\kappa'^2 = 1/\kappa^2 + 1/\kappa_d^2$  and  $\kappa_d = 3.3(1)k_0$  is our detector's effective momentum acceptance.

In the previous single-photon experiment of Chapman *et al.* [12] lost coherence was similarly "recovered" by

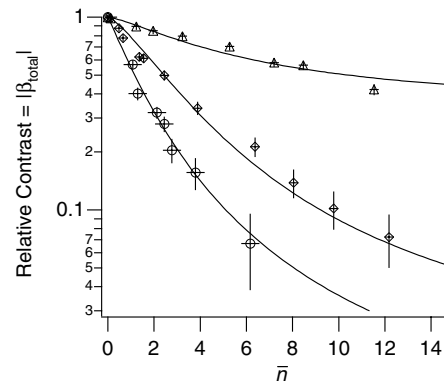


FIG. 3. Loss of interfering contrast as a function of mean number of photons spontaneously scattered by atoms within the interferometer. Each curve represents a different path separation:  $d/\lambda = 0.06$  ( $\Delta$ ),  $0.13$  ( $\diamond$ ), and  $0.16$  ( $\circ$ ).

positioning a hot-wire detector to count only atoms which had scattered photons into a small range of momentum states. This scheme required [15] that the atomic beam width,  $\sigma_x$ , be greater than the path separation,  $d$ , so that the two interfering paths partially overlapped at the point of scattering, and a scattered photon could not have provided complete which-path information, even if  $d \gg \lambda$ . The condition  $\sigma_x < d$  need not be satisfied to demonstrate the features of decoherence in the current experiment, however. Even when it is in principle possible to recover some coherence by measuring the environment, if no such attempt is made then the predicted loss of contrast is independent of  $\sigma_x$ .

In the many-photon limit, the decoherence function we have derived agrees with the solution to the master equation presented in the introduction. Comparing Eqs. (2) and (9), taking into account the time varying intensity profile,  $I(t)$ , of the scattering light as experienced by atoms in the beam, we identify  $\kappa^2 = D^2\tau$  where  $\tau$  is the amount of time needed to scatter  $\bar{n}$  photons [ $\bar{n} = \int_0^\tau I(t) dt$ ]. Because the atom-photon scattering interaction is well defined, and our decohering environment well controlled, we can accurately calculate the constant  $\kappa$  (equivalently  $D$ ) for any laser parameters.

Displayed in Fig. 4 are data which demonstrate Gaussian reduction in contrast as a function of path separation for two different laser intensities. As before, we independently determined  $\bar{n}$  and  $\sigma_n$  for each intensity, and from these values along with  $\kappa_d$  we calculate  $\kappa' = 2.5(1)k_0$  for the higher laser intensity and  $\kappa' = 1.8(1)k_0$  for the lower. Fitting the contrast data to Eq. (9) yields  $\kappa' = 2.39(5)k_0$  and  $\kappa' = 1.71(5)k_0$ , within error of the calculated values.

Our system exhibits what have been referred to as the "naive" [13] generalizations of decoherence phenomenon: exponential loss of contrast with path separation squared

and with number of scattered particles. The similarity of Eq. (1) to a diffusion equation [16] invites identification of this type of decoherence with phase diffusion or a random phase walk. To make the identification explicit, we use the identity  $|\phi_{x+d}\rangle = e^{-ik_x d}|\phi_x\rangle$  to rewrite Eq. (3) as

$$\begin{aligned} |\psi\rangle_i &\xrightarrow{\text{scat.}} |x\rangle \otimes |\phi_x\rangle + |x+d\rangle \otimes e^{ik_0 d} e^{-ik_x d} |\phi_x\rangle \\ &= \int d\vec{k} (|x\rangle + e^{-i(k_x - k_0)d} |x+d\rangle) \otimes |\vec{k}\rangle \langle \vec{k} | \phi_x \rangle. \end{aligned} \quad (11)$$

In this expression for the entangled atom-photon wave function, a photon state  $|\vec{k}\rangle$  corresponds to an atomic superposition state with the phase between the two components shifted by an amount  $\Delta\phi = (k_x - k_0)d$ . Correlating interference data with measurements of each scattered photon momentum [effectively a randomly sampled element of the distribution  $P(k)$ ] would allow complete recovery of lost contrast. In the absence of such postprocessing, however, the phase of each atom's interference fringes will vary randomly, and their sum, the measured interference pattern, will have reduced contrast. The phase diffusion and (previously discussed) which-path pictures are equally valid when the experimenter does not measure the scattered photons [17].

In conclusion, we have studied the decoherence of a spatial superposition due to photon scattering. Our data confirm theoretical predictions, and in the many-photon limit exhibit features of decoherence which are quite general. We have observed the exponential coherence loss with time and path separation squared characteristic of this general behavior, and we have for the first time predicted and experimentally verified the decoherence rate constant  $\kappa$ . The particular model we have explored is not only the most relevant for macroscopic systems but also applies generally to situations in which decoherence arises slowly through a series of independent, mildly decohering interactions, a situation of interest for decoherence avoidance or correction protocols.

This work was supported by Army Research Office Contracts No. DAAG55-98-1-0429 and No. DAA55-97-1-0236, Office of Naval Research Contract No. N00014-96-1-0432, and National Science Foundation Grant No. PHY-9877041.

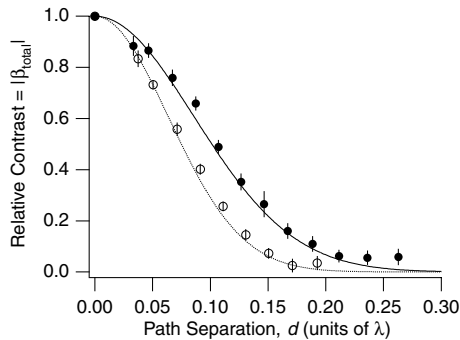


FIG. 4. Loss of contrast in the many-photon regime. Overlaid are theory curves generated from Eq. (9) using parameters (●)  $\bar{n} = 4.8(2)$ ,  $\sigma_n = 1.8(1)$  and (○)  $\bar{n} = 8.1(3)$ ,  $\sigma_n = 3.5(1)$  determined from independent beam deflection measurements.

- [1] W.G. Unruh, Phys. Rev. A **51**, 992 (1995).
- [2] H.-J. Briegel *et al.*, in *The Physics of Quantum Information*, edited by D. Bouwmeester, A. Ekert, and A. Zeilinger (Springer-Verlag, Berlin, 2000), pp. 281–293.
- [3] A.O. Caldeira and A.J. Leggett, Physica (Amsterdam) **121A**, 587 (1983).
- [4] W.G. Unruh and W.H. Zurek, Phys. Rev. D **40**, 1071 (1989).
- [5] E. Joos and H.D. Zeh, Z. Phys. B **59**, 223 (1985).

- 
- [6] M.R. Gallis and G.N. Fleming, *Phys. Rev. A* **42**, 38 (1990).
- [7] For one of the earliest derivations of a solution of this form, see D.F. Walls and G.J. Milburn, *Phys. Rev. A* **31**, 2403 (1985).
- [8] M. Brune *et al.*, *Phys. Rev. Lett.* **77**, 4887 (1996).
- [9] C.J. Myatt *et al.*, *Nature (London)* **403**, 269 (2000).
- [10] J. Schmiedmayer *et al.*, in *Atom Interferometry, Advances in Atomic, Molecular and Optical Physics*, edited by P. Berman (Academic Press, San Diego, 1997), pp. 2–83.
- [11] T. Pfau *et al.*, *Phys. Rev. Lett.* **73**, 1223 (1994).
- [12] M.S. Chapman *et al.*, *Phys. Rev. Lett.* **75**, 3783 (1995).
- [13] J.R. Anglin, J.P. Paz, and W.H. Zurek, *Phys. Rev. A* **55**, 4041 (1997).
- [14] C.C. Cheng and M.G. Raymer, *Phys. Rev. Lett.* **82**, 4807 (1999).
- [15] H.M. Wiseman *et al.*, *Phys. Rev. A* **56**, 55 (1997).
- [16] W.H. Zurek, *Phys. Today* **44**, No. 10, 36 (1991).
- [17] A. Stern, Y. Aharonov, and Y. Imry, *Phys. Rev. A* **41**, 3436 (1990).

# Appendix C

## Paper: Longitudinal Quantum Beam Tomography

David A. Kokorowski and David E. Pritchard

*Massachusetts Institute of Technology,  
Cambridge, Massachusetts 02139*

### Abstract

We propose an experiment to determine the density operator for the longitudinal quantum state of an atomic beam. The method is based on tomographic reconstruction of the Wigner function via a set of measured probability distributions for the phase-space rotated position operator. The time evolution of the Wigner function in free space effectively performs the required phase-space rotation. We propose a state-selective, time-dependent technique for measuring longitudinal probability distributions.

### C.1 INTRODUCTION

Atom interferometric experiments and other atomic beam applications which are sensitive to the quantum mechanical nature of an atom's center of mass motion, have focused attention on the question: "What is the quantum state of particles in an atomic beam?" The most statistically complete representation of such an ensemble

of quantum systems is the density operator, which contains all discernible information about the quantum state. Below we present a method for determining the density operator representing the longitudinal center of mass motion of an atomic beam. The technique may be useful in studying not only the characteristics of atomic beam sources, but also the effects of various manipulations which may create and/or alter the nature of longitudinal coherences in the beam.

Although the physical realization of an atomic beam apparatus imposes certain restrictions on the appropriate density operator[36], only an experiment which measures this operator directly is capable of fully characterizing the beam's quantum state. By 1969, several schemes of limited applicability[63, 41, 117, 78] had been proposed to perform such a measurement. Practical tomographic techniques which attempt to reconstruct the density operator by way of the Wigner distribution[122] have since garnered interest for use in optical[109], electron[116], and atomic[64, 93, 95, 57, 97, 123, 69] systems. Although several of these schemes [64, 93, 57, 69] can be used to determine the density operator for the transverse motion of atoms in an atomic beam, none have yet been developed for the study of a beam's longitudinal state.

To highlight the differences between the longitudinal and transverse cases, we briefly review the formalism underlying quantum state tomography. The general goal is to determine the Wigner function,  $W(x, p)$ , from which the density operator,  $\hat{\rho}$ , follows according to the relationship:

$$\langle p|\hat{\rho}|p'\rangle = \int_{-\infty}^{\infty} dx W\left(x, \frac{p+p'}{2}\right) e^{ix(p-p')/\hbar}. \quad (\text{C.1})$$

The Wigner function shares many features of the classical density of particles in phase space,  $f(x, p)$ . However, quantum mechanical interference effects can result in regions where the Wigner function becomes negative, precluding its characterization as a true probability distribution[97]. Nevertheless, the analogy between  $W(x, p)$  and  $f(x, p)$  can often provide an intuitive understanding of potential experiments.

The standard outline for tomographic reconstruction of  $W(x, p)$ [122, 109] involves

measuring probability distributions for the so-called ‘quadrature’ operators  $\hat{x}_\phi$  and  $\hat{p}_\phi$ :

$$\begin{aligned}\hat{x}_\phi &= \hat{x} \cos \phi + s_p^x \hat{p} \sin \phi \\ \hat{p}_\phi &= -\frac{\hat{x}}{s_p^x} \sin \phi + \hat{p} \cos \phi,\end{aligned}\tag{C.2}$$

where  $s_p^x$  is some conveniently chosen scaling factor. Given a quantum system characterized by  $W(x, p)$ , the probability that a measurement of the operator  $\hat{x}_\phi$  will yield the eigenvalue  $x_\phi$  is:

$$P_\phi(x_\phi) = \int dp_\phi W(x_\phi \cos \phi - s_p^x p_\phi \sin \phi, x_\phi \sin \phi + s_p^x p_\phi \cos \phi).\tag{C.3}$$

If the  $P_\phi(x_\phi)$  are known for all  $\phi$  in any interval  $[\phi_0, \phi_0 + \pi]$ , the Wigner function can be calculated [122] using the inversion formula:

$$W(x, p) = \frac{1}{4\pi^2} \int_{-\infty}^{\infty} dx_\phi \int_{-\infty}^{\infty} d\eta \int_0^\pi d\phi P_\phi(x_\phi) |\eta| e^{i\eta(x_\phi - (x \cos \phi + s_p^x p \sin \phi))},\tag{C.4}$$

and the fact that  $\hat{x}_\phi = -\hat{x}_{\phi-\pi}$ .

Current tomographic techniques, rather than measuring the  $\hat{x}_\phi$  operators directly, are based on measurements of a system whose Wigner function has been rotated about the origin of phase space. The position distribution for a Wigner function rotated by angle  $\phi$  is equivalent to the distribution  $P_\phi(x_\phi)$  for the original (non-rotated) Wigner function.

In the case of longitudinal tomography, both the measurement of position distributions and the rotation of the Wigner function present unique challenges. It is usually important to know the time at which a measurement is performed, which in the transverse case is simply defined according to the classical relationship  $t = z/v$ , where  $z$  is the longitudinal coordinate and  $v$  is the particle velocity. Thus, time-independent

measurements of the transverse quantum state of an atomic beam can be made by scanning a detector across the beam at a particular longitudinal position. In the longitudinal case, a static position distribution only occurs when no correlations exist between different longitudinal momenta. In more interesting cases where longitudinal momentum correlations do exist, (i.e. as a result of amplitude modulation[90]), they can only be observed using time dependent detection techniques[13, 44].

In close analogy to early tomographic experiments for optical systems, several promising tomographic schemes for atoms accomplish rotation of the Wigner function using atom optical lenses[64, 57]. In the longitudinal regime, such lenses are often not practical due to the large kinetic energies involved (although longitudinal lenses might be suitable for very slow beams or for atoms dropped from a magnetic trap.) Instead, we can exploit the highly dispersive nature of the vacuum for matter waves, a property which does not exist in optical systems. Matter waves with longer deBroglie wavelength (smaller momentum) will unavoidably propagate more slowly than those with shorter wavelength—effectively performing a rotation of the Wigner function about the origin of phase space [57]. As explicitly demonstrated in at least one experiment [69], this vacuum dispersion is sufficient to perform the measurements necessary for tomographic reconstruction of the Wigner function.

### C.1.1 Longitudinal Tomography

Our proposed experimental set-up (see Fig. C-1) begins with a standard beam source which emits identical particles of mass  $m$ , with appropriately chosen ground and excited internal states. We identify the quantum mechanical ensemble to be studied as those particles prepared in the ground state; the remaining particles are either deflected out of the beam or otherwise rendered invisible to the rest of the experiment (i.e. by placing them in an third ‘unobserved’ state.) Located at an adjustable position  $x = x_e$  in the apparatus is an electromagnetic excitation region which resonantly couples the ground and excited states. For simplicity, we assume that any particle exposed to the radiation in the region is completely excited, that is, the region is effectively a “ $\pi$ -pulse”. Downstream, a state-selective detector counts the number of

particles that have made a transition into the excited state due to the  $\pi$ -pulse.

Consider a quantum state prepared as described above which, at time  $t = 0$ , is described by the Wigner function  $W(x, p; t = 0)$ . The probability that a  $\pi$ -pulse at time  $t_e$  and position  $x = x_e$  causes a transition into the excited state (and subsequent count at the detector) is given by:

$$P_d(x_e, t_e) = \int dp W(x_e, p; t_e) \quad (\text{C.5})$$

A sequence of such measurements at time  $t_e = 0$  yields the  $\phi = 0$  distribution,  $P_{\phi=0}(x)$ .

To measure the distributions  $P_\phi(x_\phi)$  for arbitrary  $\phi$ , we allow the time evolution of matter waves in vacuum to perform a rotation of the Wigner function [57, 69, 72]. The dynamics of the Wigner function in free space are exactly the same as for the classical density function,  $W(x, p; t) = W(x - pt/m, p; 0)$ , leading to a ‘‘shearing’’ of the Wigner function which may be decomposed into a pure rotation and a rescaling of the position axis. At times  $t_e \neq 0$ , we have the following relationship between the detection probability and the desired quadrature operator distributions:

$$P_d(x_e, t_e) dx_e = P_\phi(x_\phi) dx_\phi, \quad (\text{C.6})$$

where

$$x_\phi = x_e \cos \phi, \quad \tan \phi = \frac{t_e}{s_p^x m}. \quad (\text{C.7})$$

Measurements of the longitudinal position distribution as a function of time can therefore be used to recover the quadrature operator distributions  $P_\phi$ .

The important roles of state-selection and time-dependent detection in this proposal deserve emphasis. The first state-selective step identifies the subset of particles in the beam which constitute our ensemble by (actively or passively) placing them in the only state ‘visible’ to the excitation region. State-selective detection allows us to count only those particles within the excitation region (i.e. located at a particular

$x_e$ ) in a given measurement. The use of time dependent experimental elements is demanded by the requirement that  $\phi$ , and therefore  $t_e$ , be unambiguously specified. Time dependence may be introduced either by operating the excitation region in short pulses at definite  $t_e$ , or by using an excited state whose lifetime is much shorter than the desired time resolution. In the latter case, detection consists of observing spontaneously emitted radiation, and  $t_e$  is simply the time of detection.

### C.1.2 ‘Initial’ Time

In the experiment outlined above, multiple time-dependent measurements are combined to obtain a single reconstructed Wigner function. We assume that the ensemble of particles emitted by the source is described, at some arbitrary initial time, by the Wigner function  $W(x, p; 0)$ . The time at which a measurement is performed,  $t_e$ —which in turn determines the rotation angle via Eq. C.7—is only defined relative to this initial time. We must therefore have a means of identifying the ‘initial time’ reference for subsequent measurements.

The realization of this time reference will vary depending on the system under investigation. The simplest case is for a pulsed particle source where  $t = 0$  is naturally defined as the time at which each pulse of atoms is released. For example, were the technique applied to study the quantum state of trapped atoms,  $t = 0$  would be the time at which the trapping potential was turned off.

The situation is slightly different for the case of a continuous source, such as an atomic beam. While no observable momentum correlations exist in an ideal continuous source, various beam manipulations are known to create correlated momentum states which will exhibit time dependent beats as they propagate[90]. In this case, we expect that  $W(x, p; 0)$  can be defined in terms of this manipulation (i.e. the beginning of a cycle of sinusoidal amplitude modulation.) Alternatively, we may wish to study ‘inherent’ coherences resulting, for example, from self-modulation of the beam source itself. This modulation could then be used to time subsequent measurements, provided its phase were monitored experimentally (i.e. by measuring the power spectrum of the detected signal.)

### C.1.3 Experimental Parameters

Longitudinal tomography is a potentially useful tool for studying a wide variety of atomic beam manipulations. For any given experiment, however, both the resolution of the  $P_\phi$  measurements and the range of accessible  $\phi$  values will impact the tomographic reconstruction of  $W(x, p)$ [57], and must therefore be well understood.

To investigate these limitations, we now outline a possible experiment to study the Wigner function of an amplitude modulated atomic beam. We take the initial quantum state of the beam to be an incoherent superposition of plane waves, and assume that all atoms have been prepared in the ground state,  $|g\rangle$ . Amplitude modulation might consist of a pulse of resonant radiation applied at time  $t = 0$  and position  $x = 0$ , which excites atoms into the state  $|g'\rangle$ . A simple detection scheme might take the form of a second resonance region tuned to the transition between states  $|g'\rangle$  and  $|e\rangle$ . This second region would produce short  $\pi$ -pulses at definite position  $x_e$  and time  $t_e$  and the excited state atoms would subsequently be counted in a state selecting detector.

The initial modulation pulse of such a scheme causes each incoming plane wave to acquire sidebands at frequencies determined by the fourier transform of the pulse envelope [90]. The result is a wavepacket (in the  $|g'\rangle$  state) of spatial extent  $\sigma_x \approx v_o \Delta t$  where  $v_o$  is the average beam velocity and  $\Delta t$  is the duration of the pulse. To good approximation, the velocity spread of the wavepacket,  $\sigma_v$ , will be identical to that of the original, unmodulated beam. The goal of our experiment would be to reconstruct the Wigner function representing an ensemble of these wavepackets, each identically prepared. We define the Wigner function scaling constant,  $s_p^x \equiv \frac{\sigma_x}{m\sigma_v}$ , to guarantee that  $\hat{x}$  and  $\hat{p}$  terms contribute commensurately to the expectation value of  $\hat{x}_\phi$ .

Our primary experimental concern is the range of accessible rotation angles, which in turn depends on the minimum and maximum times at which measurements are possible (Eq. C.7). We take the range of possible measurement times to be  $l_{min}/v_o < t_e \leq l_{max}/v_o$ , where  $l_{min}$  and  $l_{max}$  are the extreme longitudinal positions of the  $\pi$ -pulse excitation coil. The resulting restrictions on  $\phi$  follow from Eq. C.7:

$$0 < \tan^{-1} \left( \frac{l_{min} \sigma_v}{\sigma_x v_o} \right) \leq \phi \leq \tan^{-1} \left( \frac{l_{max} \sigma_v}{\sigma_x v_o} \right) < \frac{\pi}{2}, \quad (\text{C.8})$$

The actual range of accessible angles will be somewhat smaller than implied by Eq. C.8 due to the spreading of the wavepacket as it propagates (see Fig. C-2). However, if  $l_{max} \gg \frac{\sigma_v}{v_o} \sigma_x$ , we can approach rotation angles of  $\phi = \frac{\pi}{2}$ . (Note that in cases where the momentum distribution of the beam is available, this yields an additional measurement at exactly  $\phi = \frac{\pi}{2}$ .)

The extension from the range  $[0, \frac{\pi}{2}]$  to  $[-\frac{\pi}{2}, \frac{\pi}{2}]$ , yielding the full range of  $\pi$  radians needed to reconstruct  $W(x, p)$ , requires using reasonable assumptions regarding symmetry properties of the Wigner function[69]. In particular, for most atomic beam experiments the longitudinal velocity distribution is nearly symmetric about the mean velocity  $v_o$ . In the limit that our beam manipulations are velocity independent, the resulting wavepacket and its Wigner function will possess this symmetry as well. If we invoke the invariance of the Wigner function under Galilean transformations[97] and refer our measurements to a (primed) frame moving at velocity  $v_o$  with respect to the laboratory, then reflection symmetry about the zero velocity axis implies  $P'_\phi(x'_\phi) = P_{\pi-\phi}(x_\phi)$ , and we have potential access to the full range of rotation angles  $[-\frac{\pi}{2}, \frac{\pi}{2}]$ .

A second experimental consideration is the  $\phi$  resolution of our measurements, given explicitly by:

$$d\phi = \cos^2 \phi \frac{\sigma_v}{\sigma_x} dt_e. \quad (\text{C.9})$$

Thus, for a given detector response time  $dt_e$ , the resolution improves with increasing rotation angle. The worst resolution, at  $\phi \approx 0$ , will therefore constrain the number of independent rotation angles at which measurements may be made.

We now present a simple feasibility analysis, ignoring such concerns as signal-to-noise rates in the detector, efficiency of the excitation regions, counting rates, and total integration time which must be determined in terms of the techniques used in a particular experiment. We consider a typical supersonic atomic beam apparatus,

with mean beam velocity,  $v_o = 1000\text{m/s}$ , and velocity width  $\sigma_v = 50\text{m/s}$ . Assuming a stationary detector and a reasonable response time of  $dt_e \approx 100\text{ns}$ , yields a spatial resolution,  $dx \equiv v_o dt_e \approx 100\mu\text{m}$ . In order that features of the Wigner function be well resolved,  $\sigma_x$  should be at least an order of magnitude larger than  $dx$ . Given these parameters, the range of accessible rotation angles is shown in Figure C-2 as a function of the relevant distances. We observe that for reasonable dimensions  $l_{max} = 1\text{m}$ ,  $l_{min} = 0.5\text{cm}$ , and  $\sigma_x = 0.4\text{cm}$ , nearly 90% of the range  $[-\frac{\pi}{2}, \frac{\pi}{2}]$  is experimentally accessible. For  $\sigma_x \leq dx$  and beam parameters given above, Eq. C.9 yields a minimum resolution of  $d\phi \leq 0.05\text{rad}$ . This implies the possibility of  $P_\phi(x_\phi)$  measurements at on the order of 100 different rotation angles.

Because the estimated minimum resolution element,  $dx \approx 100\mu\text{m}$ , is much larger than the spread in deBroglie wavelengths of particles in the beam ( $\Delta\lambda_{dB} \equiv \frac{h}{m\sigma_v} \approx 3$  Angstrom), we do not expect to be able to resolve ‘non-classical’ features of the Wigner function—regions where  $W(x, p) < 0$ . Using velocity selection to reduce  $\sigma_v$ , coupled with a laser based detection scheme (with  $dx \approx 1\mu\text{m}$ ), might conceivably render such features visible. The given resolution is nevertheless more than sufficient for studying momentum correlations which result in spatial features of order several centimeters—as would result from amplitude modulation in the 50-100kHz range.

Thanks to Al-Amin Dhirani for several helpful conversations, and to Richard Rubenstein and Edward Smith for their comments and insights. This work was supported by Army Research Office contracts DAAH04-94-G-0170 and DAAH04-95-1-0533, Office of Naval Research contracts N00014-89-J-1207 and N000014-96-1-0432, Joint Services Electronics Program contract DAAH04-95-1-0038, and National Science Foundation contract PHY-9514795.

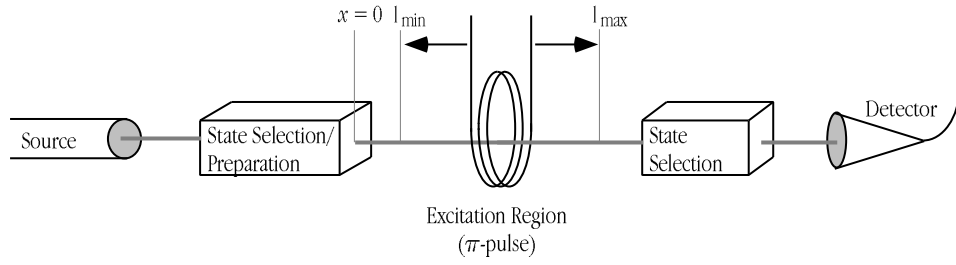


Figure C-1: Proposed setup for longitudinal quantum beam tomography. The atomic beam source emits particles which are selected according to their internal state. Those particles in the chosen “ground” state pass into the  $\pi$ -pulse region, where there is a certain probability of transition into the excited state. Those that have been excited are counted in the state selective detector.

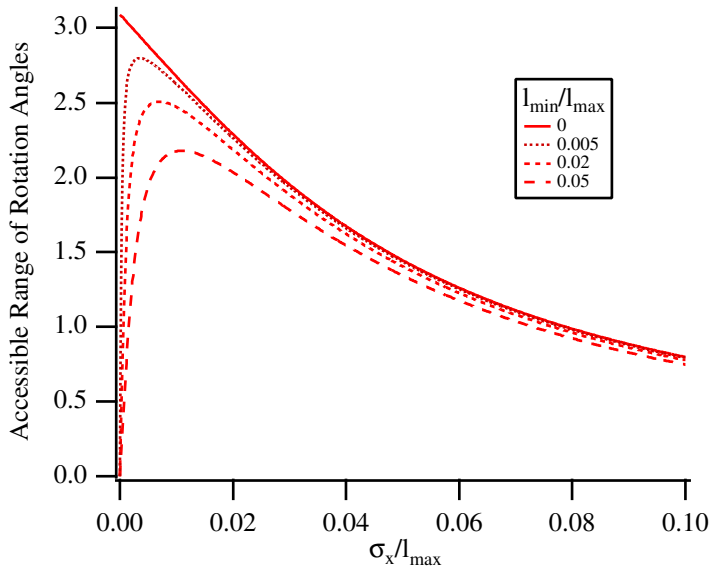


Figure C-2: Range of experimentally accessible rotation angles as a function of the dimensionless ratio  $\sigma_x/l_{max}$ . Several curves are shown for different values of  $l_{min}$ , the shortest possible distance between the detector and the preparation region. A factor of two enhancement has been included from the symmetry of  $W(x, p)$  about the mean beam velocity.

# Bibliography

- [1] Articles describing interferometric studies of vortices in BECs are forthcoming from the Ketterle group at the Massachusetts Institute of Technology and the Dalibard group at the Ecole Normale Supérieure.
- [2] This is the implication of spontaneous collapse models, for example [111], which postulate dynamics outside of standard quantum theory to establish quantum-classical correspondence.
- [3] Perhaps the most dramatic demonstration is that of coherent spatial superpositions of BEC's [6, 53, 67].
- [4] For one of the earliest derivations of a solution of this form, see D.F. Walls and G.J. Milburn. *Phys. Rev. A*, 79:2403, 1985.
- [5] H. Ammann, R. Gray, N. Christensen, and I. Shvachuck. Experimental observation of dynamical localization and decoherence in the atomic delta-kicked rotor. *J. Phys. B-At. Mol. Opt. Phys.*, 31(10):2449–2455, 1998.
- [6] M.R. Andrews, C.G. Townsend, H.J. Miesner, D.S. Durfee, D.M. Kurn, and W. Ketterle. Observation of interference between two Bose condensates. *Science*, 275:637–41, 1997.
- [7] J.R. Anglin, J.P. Paz, and W.H. Zurek. Deconstructing decoherence. *Phys. Rev. A*, 55(6):4041–4053, 1997.
- [8] E. Audouard, P. Duplax, and J. Vigue. Glory and resonance effects in the index of refraction for atomic waves. *Europhys. Lett.*, 32(5):397, 1995.

- [9] D. Bacon, D.A. Lidar, and K.B. Whaley. Robustness of decoherence-free subspaces for quantum computation. *Phys. Rev. A*, 60:1944–1955, 1999.
- [10] G. Badurek, H. Rauch, and A. Zeilinger. Matter wave interferometry. *Physica B*, 151:R9–R10, 1988.
- [11] W.E. Baylis. Semiempirical, pseudopotential calculation of alkali-noble-gas interatomic potentials. *J. Chem. Phys.*, 51:2665–79, 1969.
- [12] P.R. Berman, editor. *Atom Interferometry*. Advances in Atomic, Molecular, and Optical Physics. Academic Press, San Diego, 1997.
- [13] H.J. Bernstein and F.E. Low. Measurement of longitudinal coherence lengths in particle beams. *Phys. Rev. Lett.*, 59(9):951–3, 1987.
- [14] M.V. Berry. Quantal phase factors accompanying adiabatic changes. *Proc. Roy. Soc. Lon. A*, 392:45–57, 1984.
- [15] I. Bloch, T.W. Hansch, and T. Esslinger. Measurement of the spatial coherence of a trapped Bose gas at the phase transition. *Nature*, 403(6766):166–170, 2000.
- [16] U. Bonse and H. Rauch. *Neutron Interferometry*. Oxford University Press, Oxford, 1979.
- [17] H.-J. Briegel, W. Dr, S.J. van Enk, J.I. Cirac, and P. Zoller. Quantum networks II: Communication over noisy channels. In D. Bouwmeester, A. Ekert, and A. Zeilinger, editors, *The Physics of Quantum Information*, pages 281–293. Springer-Verlag, Berlin, 2000.
- [18] M. Brune, E. Hagley, J. Dreyer, X. Maitre, A. Maali, C. Wunderlich, J.M. Raimond, and S. Haroche. Observing the progressive decoherence of the “meter” in a quantum measurement. *Phys. Rev. Lett.*, 77(24):4887–4890, 1996.
- [19] U. Buck and H. Pauly. Interferences in atomic collision processes and their interpretation using a modified Lennard-Jones potential. *Z. Phys.*, 208:390–417, 1968.

- [20] A.O. Caldeira and A.J. Leggett. Path integral approach to quantum brownian-motion. *Physica A*, 121(3):587–616, 1983.
- [21] O. Carnal and J. Mlynek. Youngs double slit experiment with atoms: A simple atom interferometer. *Phys. Rev. Lett.*, 66:2689, 1991.
- [22] C. Champenois, E. Audouard, P. Duplaa, and J. Vigue. Refractive index for atomic waves: Theory and detailed calculations. *J. de Phys. II*, 7(4):523–41, 1997.
- [23] C. Champenois, M. Büchner, and J. Vigué. Fringe contrast in three grating Mach-Zehnder atomic interferometers. *Eur. Phys. J. D*, 5:363–374, 1999.
- [24] M.S. Chapman. *Photon Induced Coherence Loss in Atom Interferometry*. PhD dissertation, Massachusetts Institute of Technology, Department of Physics, 1995.
- [25] M.S. Chapman, T.D. Hammond, A. Lenef, J. Schmiedmayer, R.A. Rubenstein, E. Smith, and D.E. Pritchard. Photon scattering from atoms in an atom interferometer — coherence lost and regained. *Phys. Rev. Lett.*, 75(21):3783–3787, 1995.
- [26] C.C. Cheng and M.G. Raymer. Long-range saturation of spatial decoherence in wave-field transport in random multiple-scattering media. *Phys. Rev. Lett.*, 82(24):4807–4810, 1999.
- [27] J.F. Clauser and S. Li. “Heisenberg microscope” decoherence atom interferometry. *Phys. Rev. A*, 50:2430–3, 1994.
- [28] J. Denschlag, J.E. Simsarian, D.L. Feder, C.W. Clark, L.A. Collins, J. Cubizolles, L. Deng, E.W. Hagley, K. Helmerson, W.P. Reinhardt, S.L. Rolston, B.I. Schneider, and W.D. Phillips. Generating solitons by phase engineering of a Bose-Einstein condensate. *Science*, 287:97–101, 2000.

- [29] A.A. Dhirani, D.A. Kokorowski, R.A. Rubenstein, T.D. Hammond, B. Rohweder, E.T. Smith, A.D. Roberts, and D.E. Pritchard. Determining the density matrix of a molecular beam using a longitudinal matter wave interferometer. *J. Mod. Opt.*, 44(11-12):2583–2589, 1997.
- [30] L.-M. Duan and G.-C. Guo. Preserving coherence in quantum computation by pairing quantum bits. *Phys. Rev. Lett.*, 79:1953–6, 1997.
- [31] R. Duren and W. Groger. A determination of the Na-Ar ground state potential from differential cross section measurements. *Chem. Phys. Lett.*, 56:67–70, 1978.
- [32] R. Duren and Ch. Schlier. Accurate fitting of realistic interatomic potential. *J. Chem. Phys.*, 46:4535–36, 1967.
- [33] S. Durr, T. Nonn, and G. Rempe. Fringe visibility and which-way information in an atom interferometer. *Phys. Rev. Lett.*, 81:5705–9, 1998.
- [34] C.R. Ekstrom. *Experiments with a Separated Beam Atom Interferometer*. PhD dissertation, Massachusetts Institute of Technology, Department of Physics, 1993.
- [35] C.R. Ekstrom, J. Schmiedmayer, M.S. Chapman, T.D. Hammond, and D.E. Pritchard. Measurement of the electric polarizability of sodium with an atom interferometer. *Phys. Rev. A*, 51:3883–8, 1995.
- [36] B.-G. Englert, C. Miniatura, and J. Baudon. Least-bias description of atomic beams. *J. de Physique II*, 4(11):2043–59, 1994.
- [37] B.G. Englert. Fringe visibility and which-way information: An inequality. *Phys. Rev. Lett.*, 77:2154–7, 1996.
- [38] R.C. Forrey, L. You, V. Kharchenko, and A. Dalgarno. The index of refraction of noble gases for sodium matter waves. *Phys. Rev. A*, 54(3):2180–4, 1996.
- [39] R.C. Forrey, L. You, V. Kharchenko, and A. Dalgarno. Refining molecular potentials using atom interferometry. *Phys. Rev. A*, 55(5):R3311–4, 1997.

- [40] M. Freyberger, S.H. Kienle, and V.P. Yakovlev. Interferometric measurement of an atomic wave function. *Phys. Rev. A*, 56(1):195–201, 1997.
- [41] W. Gale, E. Guth, and G.T. Trammel. Determination of the quantum state by measurements. *Phys. Rev.*, 165:1434, 1968.
- [42] M.R. Gallis and G.N. Fleming. Environmental and spontaneous localization. *Phys. Rev. A*, 42(1):38–48, 1990.
- [43] P. Geotsch and R. Graham. Decoherence by spontaneous emission in atomic-momentum transfer experiments. *Phys. Rev. A*, 54:5345–8, 1996.
- [44] R. Golub and S.K. Lamoreaux. Elucidation of the neutron coherence length and a matter-wave sideband interferometer. *Phys. Lett. A*, 162(2):122–8, 1992.
- [45] P.L. Gould. *Momentum Transfer to Atoms by Absorption and Emission of Radiation*. PhD dissertation, Massachusetts Institute of Technology, Department of Physics, 1985.
- [46] P.L. Gould, P.J. Martin, G.A. Ruff, R.E. Stoner, J.L. Picque, and D.E. Pritchard. Momentum-transfer to atoms by a standing light-wave - transition from diffraction to diffusion. *Phys. Rev. A*, 43(1):585–588, 1991.
- [47] R.E. Grisenti, W. Schöllkopf, J.P. Toennies, C.C. Hegerfeldt, and T. Kohler. Determination of atom-surface van der Waals potentials from transmission-grating diffraction intensities. *Phys. Rev. Lett.*, 83:1755–1758, 1999.
- [48] R.E. Grisenti, W. Schöllkopf, J.P. Toennies, J.R. Manson, T.A. Savas, and H.I. Smith. He-atom diffraction from nanostructure transmission gratings: The role of imperfections. *Phys. Rev. A*, 61:33608, 2000.
- [49] T.L. Gustavson. *Precision Rotation Sensing using Atom Interferometry*. PhD dissertation, Stanford University, 2000.

- [50] T.L. Gustavson, P. Bouyer, and M.A. Kasevich. Precision rotation measurements with an atom interferometer gyroscope. *Phys. Rev. Lett.*, 78(11):2046–2049, 1997.
- [51] A.H.M. Habets. *Supersonic Expansion of Argon into Vacuum*. PhD dissertation, Eindhoven University of Technology, 1997.
- [52] E.W. Hagley, L. Deng, M. Kozuma, M. Trippenbach, Y.B. Band, M. Edwards, M. Doery, P.S. Julienne, K. Helmerson, S.L. Rolston, and W.D. Phillips. Measurement of the coherence of a Bose-Einstein condensate. *Phys. Rev. Lett.*, 82:3112–5, 1999.
- [53] D.S. Hall, M.R. Matthews, C.E. Wieman, and E.A. Cornell. Measurements of relative phase in two-component Bose-Einstein condensates. *Phys. Rev. Lett.*, 81:1543–6, 1998.
- [54] T.D. Hammond. *Atom Interferometry: Dispersive Index of Refraction and Rotation Induced Phase Shifts for Matter-Waves*. PhD dissertation, Massachusetts Institute of Technology, Department of Physics, 1997.
- [55] T.D. Hammond, M.S. Chapman, A. Lenef, J. Schmiedmayer, E.T. Smith, R.A. Rubenstein, D.A. Kokorowski, and D.E. Pritchard. Matter-wave index of refraction, inertial sensing, and quantum decoherence in an atom interferometer. *Revista Brasileira de Fisica*, 27:192–213, 1997.
- [56] S. Inouye, T. Pfau, S. Gupta, A.P. Chikkatur, A. Gorlitz, D.E. Pritchard, and W. Ketterle. Phase-coherent amplification of atomic matter waves. *Nature*, 402:641–644, 1999.
- [57] U. Janicke and M. Wilkens. Tomography of atom beams. *J. Mod. Opt.*, 42(11):2183–99, 1995.
- [58] E. Joos and H.D. Zeh. The emergence of classical properties through interaction with the environment. *Z. Phys. B-Condens. Mat.*, 59(2):223–243, 1985.

- [59] M. Kasevich and S. Chu. Atomic interferometry using stimulated Raman transitions. *Phys. Rev. Lett.*, 67:181, 1991.
- [60] David W. Keith, Christopher R. Ekstrom, Quentin A. Turchette, and David E. Pritchard. An interferometer for atoms. *Phys. Rev. Lett.*, 66:2693, 1991.
- [61] D.W. Keith. *An Interferometer for Atoms*. PhD dissertation, Massachusetts Institute of Technology, Department of Physics, 1991.
- [62] D.W. Keith, R.J Soave, and M.J. Rooks. Free standing gratings and lenses for atom optics. *J. Vac. Sci. Technol. B*, 9:2846, 1991.
- [63] E.C. Kemble. *The fundamental principles of quantum mechanics*. Dover, New York, 1937.
- [64] S.H. Kienle, M. Freyberger, W.P. Schleich, and M.G. Raymer. *Experimental Metaphysics: Quantum Mechanical Studies for Abner Shimony*, chapter Quantum beam tomography. Kluwer Academic Publisher, Dordrecht, 1997.
- [65] D.A. Kokorowski, A.D. Cronin, T.D. Roberts, and D.E. Pritchard. From single to multiple-photon decoherence in an atom interferometer. *Phys. Rev. Lett.*, 86:2191–5, 2001.
- [66] D.A. Kokorowski and D.E. Pritchard. Longitudinal quantum beam tomography. *J. Mod. Opt.*, 44:2575–81, 1997.
- [67] M. Kozuma, L. Deng, E.W. Hagley, J. Wen, R. Lutwak, K. Helmerson, S.L. Rolston, and W.D. Phillips. Coherent splitting of Bose-Einstein condensed atoms with optically induced Bragg diffraction. *Phys. Rev. Lett.*, 82(5):871–875, 1999.
- [68] M. Kozuma, Y. Suzuki, Y. Torii, T. Sugiura, T. Kuga, E.W. Hagley, and L. Deng. Phase-coherent amplification of matter waves. *Science*, 286(5448):2309–2312, 1999.

- [69] Ch. Kurtsiefer, T. Pfau, and J. Mlynek. Measurement of the Wigner function of an ensemble of helium atoms. *Nature*, 386(13):150–153, 1997.
- [70] P.G. Kwiat, A.J. Berglund, J.B. Altepeter, and A.G. White. Experimental verification of decoherence-free subspaces. *Science*, 290:498–501, 2000.
- [71] A. Lenef, T.D. Hammond, E.T. Smith, M.S. Chapman, R.A. Rubenstein, and D.E. Pritchard. Rotation sensing with an atom interferometer. *Phys. Rev. Lett.*, 78:760–763, 1997.
- [72] U. Leonhardt. Quantum-state tomography and discrete Wigner function. *Phys. Rev. Lett.*, 74(21):4101–5, 1995.
- [73] U. Leonhardt and M.G. Raymer. Observation of moving wave packets reveals their quantum state. *Phys. Rev. Lett.*, 76(12):1985–1989, 1996.
- [74] D.A. Lidar, I.L. Chuang, and K.B. Whaley. Decoherence-free subspaces for quantum computation. *Phys. Rev. Lett.*, 81:2594–7, 1998.
- [75] H. Maier-Leibnitz and T. Springer. Ein interferometer für langsame neutronen. *Z.Phys.*, 167:368, 1962.
- [76] L. Marton. Electron interferometer. *Phys. Rev.*, 85:1057, 1952.
- [77] L. Marton, J.A. Simpson, and H.A. Suddeth. An electron interferometer. *Rev. Sci. Instrum.*, 25:1099, 1954.
- [78] W.E. Lamb, Jr.. An operational interpretation of nonrelativistic quantum mechanics. *Phys. Tod.*, 22(9):23, 1969.
- [79] M. Mei and M. Weitz. Controlled decoherence in multiple beam Ramsey interference. *Phys. Rev. Lett.*, 86:559, 2001.
- [80] Ch. Miniatura, J. Robert, O. Gorceix, V. Lorent, S. Le Boiteux, J. Reinhardt, and J. Baudon. Atomic interferences and the topological phase. *Phys. Rev. Lett.*, 69:261–264, 1992.

- [81] G. Mollenstedt and H. Duker. Frensel'scher interferenzversuch mit einem biprisma für elektronenwellen. *Naturwissenschaften*, 42:41, 1955.
- [82] J.H. Müller, D. Bettermann, V. Reiger, K. Sengstock, U. Sterr, and W. Ertmer. Topological phase-shift in a cold-atom interferometer. *Appl. Phys. B*, 60:199–204, 1995.
- [83] C.J. Myatt, B.E. King, Q.A. Turchette, C.A. Sackett, D. Kielpinski, W.M. Itano, C. Monroe, and D.J. Wineland. Decoherence of quantum superpositions through coupling to engineered reservoirs. *Nature*, 403(6767):269–273, 2000.
- [84] S. Nowak, T. Pfau, and J. Mlynek. A matter-wave interferometer based on the dc-stark effect. *Appl. Phys. B*, 69:269–275, 1999.
- [85] C. Orzel, A.K. Tuchman, M.L. Fenselau, M. Yasuda, and M.A. Kasevich. Squeezed states in a Bose-Einstein condensate. *Science*, 291:2386–9, 2001.
- [86] G.M. Palma, K.-A. Suominen, and A.K. Ekert. Quantum computers and dissipation. *Proc. R. Soc. London A*, 452:567–84, 1996.
- [87] J. Pascale and J. Vandeplanque. Excited molecular terms of the alkali-rare gas atom pairs. *J. Chem. Phys.*, 60:2278–2289, 1974.
- [88] A. Peters, K.Y. Chung, and S. Chu. Measurement of gravitational acceleration by dropping atoms. *Nature*, 400(6747):849–852, 1999.
- [89] T. Pfau, S. Spalter, C. Kurtsiefer, C.R. Ekstrom, and J. Mlynek. Loss of spatial coherence by a single spontaneous emission. *Phys. Rev. Lett.*, 73(9):1223–1226, 1994.
- [90] D.E. Pritchard, R.A. Rubenstein, A. Dhirani, D.A. Kokorowski, E.T. Smith, T.D. Hammond, , and B. Rohwedder. Longitudinal atom optics using localized oscillating fields: A fully quantum mechanical treatment. *Phys. Rev. A*, 59:4641–52, 1998.

- [91] H. Rauch, W. Treimer, and U. Bonse. Test of a single crystal neutron interferometer. *Phys. Rev. A*, 47:369, 1974.
- [92] M.G. Raymer. Measuring the quantum mechanical wave function. *Contemp. Phys.*, 38(5):343–355, 1997.
- [93] M.G. Raymer, M. Beck, and D.F. McAlister. Complex wave-field reconstruction using phase-space tomography. *Phys. Rev. Lett.*, 72(8):1137–40, 1994.
- [94] F. Riehle, T. Kisters, A. Witte, J. Helmcke, and C.J. Bordé. Optical Ramsey spectroscopy in a rotating frame: Sagnac effect in a matter-wave interferometer. *Phys. Rev. Lett.*, 67:177, 1991.
- [95] J. Robert, Ch. Miniatura, S.N. Chormaic, J. Lawson-Daku, O. Gorceix, F. Perales, and J. Baudon. Angular correlation measurements in a thermal beam of  $H^*$  (2s) atoms using a stern-gerlach atomic axicon. *J. de Physique II*, 4(11):2061–71, 1994.
- [96] M.J. Rooks, R.C. Tiberio, M.S. Chapman, T.D. Hammond, E.T. Smith, A. Lenef, R.A. Rubenstein, D.E. Pritchard, and S. Adams. Coherence of large gratings and electron-beam fabrication techniques for atom-wave interferometry. *J. Vac. Sci. Technol. B*, 13:2745, 1995.
- [97] A. Royer. Measurement of quantum states and the Wigner function. *Found. Phys.*, 19(1):3–32, 1989.
- [98] R.A. Rubenstein. *Longitudinal Atom Optics: Measuring the Density Matrix of a Matter Wave Beam*. PhD dissertation, Massachusetts Institute of Technology, Department of Physics, 1999.
- [99] R.A. Rubenstein, A. Dhirani, D.A. Kokorowski, T.D. Roberts, E.T. Smith, W.W. Smith, H.J. Bernstein, J. Lehner, S. Gupta, and D.E. Pritchard. Search for off-diagonal density matrix elements for atoms in a supersonic beam. *Phys. Rev. Lett.*, 82:2018–2021, 1999.

- [100] R.A. Rubenstein, D.A. Kokorowski, A. Dhirani, T.D. Roberts, S. Gupta, J. Lehner, W.W. Smith, E.T. Smith, H.J. Bernstein, and D.E. Pritchard. Measurement of the density matrix of a longitudinally modulated atomic beam. *Phys. Rev. Lett.*, 83:2285–8, 1999.
- [101] J.J. Sakurai. *Modern Quantum Mechanics*. Addison-Wesley, Reading, MA, 1994.
- [102] T.A. Savas, S.N. Shah, M.L. Schattenburg, J.M. Carter, and H.I. Smith. Achromatic interferometric lithography for 100-nm period gratings and grids. *J. Vac. Sci. Technol. B*, 13:2732, 1995.
- [103] R. P Saxon, R.E. Olson, and B. Liu. Ab initio calculations for the  $x_\sigma^2$ ,  $a_\pi^2$ , and  $b_\sigma^2$  stats of NaAr: Emission spectra and cross sections for fine structure transitions in Na-Ar collisions. *J. Chem. Phys.*, 67:2692–2702, 1977.
- [104] J. Schmiedmayer, M.S. Chapman, C.R. Ekstrom, T.D. Hammond, D.A. Kokorowski, A. Lenef, R.A. Rubenstein, E.T. Smith, and D.E. Pritchard. Optics and interferometry with atoms and molecules. In P.R. Berman, editor, *Atom Interferometry*, Advances in Atomic, Molecular and Optical Physics, pages 2–83. Academic Press, San Diego, 1997.
- [105] J. Schmiedmayer, M.S. Chapman, C.R. Ekstrom, T.D. Hammond, S. Wehinger, and D.E. Pritchard. Index of refraction of various gases for sodium matter waves. *Phys. Rev. Lett.*, 74(7):1043–1047, 1995.
- [106] J.E. Simsarian, J. Denschlag, M. Edwards, C.W. Clark, L. Deng, E.W. Hagley, K. Helmerson, S.L. Rolston, and W.D. Phillips. Imaging the phase of an evolving Bose-Einstein condensate wave function. *Phys. Rev. Lett.*, 85:2040–3, 2000.
- [107] R.E. Smalley, D.A. Auerbach, P.S.H. Fitch, D.H. Levey, and L. Wharton. Laser spectroscopic measurement of weakly attractive interatomic potentials: the Na-Ar interaction. *J. Chem. Phys.*, 66:3778–85, 1977.

- [108] E.T. Smith. *Velocity Rephased Coherences in a Longitudinal Atom Interferometer*. PhD dissertation, Harvard University, Department of Applied Physics, 1998.
- [109] D.T. Smithey, M. Beck, M.G. Raymer, and A. Faridani. Measurement of the Wigner distribution and the density matrix of a light mode using optical homodyne tomography: Application to squeezed states and the vacuum. *Phys. Rev. Lett.*, 70(9):1244–7, 1993.
- [110] M.J. Snadden, J.M. McGuirk, P. Boyer, K.G. Haritos, and M.A. Kasevich. Measurement of the earth’s gravity gradient with an atom interferometer. *Phys. Rev. Lett.*, 81:971–4, 1998.
- [111] I.-O. Stamatescu. *Decoherence and the Appearance of a Classical World in Quantum Theory*, chapter Stochastic Collapse Models. Springer-Verlag, Berlin, 1996.
- [112] R.F. Streater and A.S. Wightman. *PCT, Spin and Statistics, and all that*. W.A. Benjamin, New York, NY, 1964.
- [113] J. Summhammer, H. Rauch, and D. Tuppinger. Stochastic and deterministic absorption in neutron-interference experiments. *Phys. Rev. A*, 36:4447–55, 1987.
- [114] K.T. Tang and J. P Toennies. A simple theoretical model for the van der Waals potential at intermediate distances I. Spherically symmetric potentials. *J. Chem. Phys.*, 66(4):1496–1506, 1977.
- [115] M. Tegmark. Apparent wave function collapse caused by scattering. *Found. Phys. Lett.*, 6:571–90, 1993.
- [116] M. Tegmark. Measuring quantum states: Eperimental setup for measuring the spatial density matrix. *Phys. Rev. A*, 54(4):2703–6, 1996.
- [117] G.T. Trammel. Momentum after position. *Phys. Tod.*, 22(10):9, 1969.

- [118] W.G. Unruh. Maintaining coherence in quantum computers. *Phys. Rev. A*, 51(2):992–997, 1995.
- [119] W.G. Unruh and W.H. Zurek. Reduction of a wave packet in quantum brownian-motion. *Phys. Rev. D*, 40(4):1071–1094, 1989.
- [120] J.J.H. van den Biesen. Elastic scattering I: Integral cross sections. In G. Scoles, editor, *Atomic and Molecular Beam Methods*. Oxford University Press, New York, NY, 1988.
- [121] J. Vigué. Index of refraction of dilute matter in atomic interferometry. *Phys. Rev. A*, 52(5):3973–5, 1995.
- [122] K. Vogel and H. Risken. Determination of quasiprobability distributions in terms of probability distributions for the rotated quadrature phase. *Phys. Rev. A*, 40(5):2847–9, 1989.
- [123] S. Wallentowitz and W. Vogel. Reconstruction of the quantum mechanical state of a trapped ion. *Phys. Rev. Lett.*, 75(16):2932–5, 1995.
- [124] I.A. Walmsley and N.P. Bigelow. Measuring the quantum state of cold atoms using momentum-shearing interferometry. *Phys. Rev. A*, 57(2):R713–R716, 1998.
- [125] D.S. Weiss, B.C. Young, and S. Chu. Precision measurement of  $\hbar/m_Cs$  based on photon recoil using laser-cooled atoms and atomic interferometry. *Appl. Phys. B*, 59:217–56, 1994.
- [126] G.C. Wick, A.S. Wightman, and E.P. Wigner. The intrinsic parity of elementary particles. *Phys. Rev.*, 88:101–5, 1952.
- [127] G.C. Wick, A.S. Wightman, and E.P. Wigner. Superselection rule for charge. *Phys. Rev. D*, 1:3267–9, 1970.
- [128] M. Wilkens. Quantum phase of a moving dipole. *Phys. Rev. Lett.*, 72:5–8, 1994.
- [129] P. Zanardi. Computation on an error-avoiding quantum code and symmetrization. *Phys. Rev. A*, 60:R729–32, 1999.

- [130] P. Zanardi and M. Rasetti. Noiseless quantum codes. *Phys. Rev. Lett.*, 79:3306–9, 1997.
- [131] H.D. Zeh. *Decoherence and the Appearance of a Classical World in Quantum Theory*, chapter The Program of Decoherence: Ideas and Concepts. Springer, Berlin, 1996.
- [132] K. Zeiske, G. Zinner, F. Riehle, and J. Helmcke. Atom interferometry in a static electric-field—measurement of the Aharonov-Casher phase. *Appl. Phys. B*, 60:205–209, 1995.
- [133] W. Zurek, 2000. private communication.
- [134] W.H. Zurek. Preferred states, predictability, classicality and the environment-induced decoherence. *Prog. Theor. Phys.*, 89:281–312, 1993.